Laminar Separation Bubble Dynamics on a Finite Wing

by

Connor Toppings

A thesis
presented to the University of Waterloo
in fulfillment of the
thesis requirement for the degree of
Master of Applied Science
in
Mechanical Engineering

Waterloo, Ontario, Canada, 2021

Author's Declarations

This thesis consists of material all of which I authored or co-authored: see Statement of Contributions included in the thesis. This is a true copy of the thesis, including any required final revisions, as accepted by my examiners.

I understand that this document may be made electronically available to the public.

Statement of Contributions

Connor Toppings is the sole author of Chapters 1–3 and 6. This thesis contains portions of two co-authored manuscripts written for publication. Exceptions to sole authorship are as follows:

Chapter 4 is adapted from [1]. The experiments presented in Chapter 4 were conducted by Connor Toppings and Dr. John Kurelek. Connor Toppings conducted all data processing and analysis, and wrote the draft manuscript. Dr. John Kurelek and Dr. Serhiy Yarusevych also provided intellectual contributions to the manuscript.

Chapter 5 is adapted from a manuscript written for publication. The experiments presented in Chapter 5 were performed by Connor Toppings, who also conducted all data processing and analysis, and wrote the draft manuscript. Dr. Serhiy Yarusevych also provided intellectual contributions to the manuscript.

Abstract

Laminar separation bubbles substantially influence the performance of finite wings at low chord Reynolds numbers. The objective of this study is to explore the influence of wingtip effects on three-dimensional laminar separation bubble topology and dynamics on a finite wing. An experimental investigation is conducted on a laminar separation bubble forming on the suction surface of a cantilevered rectangular NACA 0018 wing with a semi-aspect ratio of 2.5 at a chord Reynolds number of 1.25×10^5 and an angle of attack of 6°. Surface pressure and particle image velocimetry measurements are employed to investigate the separation bubble flowfield. Using a two-dimensional airfoil of the same profile, the separation bubble on the wing is compared to a nominally two-dimensional separation bubble at similar effective angles of attack. On the portion of the wing where laminar boundary layer separation occurs, the separated shear layer rolls up into spanwise uniform vortices which develop similarly to the vortices observed on the two-dimensional airfoil, despite spanwise changes to the mean separation bubble structure along the wingspan. Whereas a decrease in the angle of attack of the two-dimensional airfoil causes a downstream shift in the locations of separation and reattachment and a reduction in the frequency of shear layer vortex shedding, spanwise variations of these parameters on the wing are much smaller than the variations expected due to the reduction in effective angle of attack near the wingtip. On the inboard portion of the wing, the location and vortex shedding frequency of the separation bubble are analogous to the separation bubble on the two-dimensional airfoil at the effective angle of attack of the wing root. Downwash from the wingtip vortex inhibits boundary layer separation in proximity to the wingtip, suppressing shear layer vortex shedding and causing a delay in transition near the wingtip. Unlike a canonical two-dimensional separation bubble, the separation bubble on the wing becomes an open separation near the wingtip, where the spanwise pressure gradient causes fluid to enter into the separation bubble, producing a substantial spanwise flow within recirculation region. A comparison with the results of previous studies suggests a similar bubble topology across different wing geometries and experimental conditions. The results of this investigation quantify the influence of wingtip effects on a laminar separation bubble, elucidating the three-dimensional changes to the bubble's mean structure and dynamics along the wingspan.

Acknowledgements

I thank God for giving me the opportunity to be a scholar. I also thank my supervisor, Dr. Serhiy Yarusevych, for his support and genuine interest in the work of his students. Thank you John Kurelek for teaching me how to operate the lab equipment and helping me to finish my first PIV campaign the week the pandemic was declared. I would also like to thank the rest of my fellow FMRL students: Kaycee Okoye, Supun Pieris, Kieran Qin, Yash Shah, Nikhilesh Tumuluru-Ramesh, and Caddie Zhang.

I also acknowledge the Canadian taxpayers who funded this work through the Natural Sciences and Engineering Research Council.

Contents

List of Figures

List of Tables

Nomenclature

Abbreviations

2C	Two Component
3C	Three Component
DNS	Direct Numerical Simulation
K-H	Kelvin-Helmholtz
LSB	Laminar Separation Bubble
NACA	National Advisory Committee for Aeronautics
PIV	Particle Image Velocimetry
POD	Proper Orthogonal Decomposition
RMS	Root Mean Square
RMSE	Root Mean Square Error
T-S	Tollmein-Schlichting

Accents and Subscripts

Example	**Description**
$\overline{a}$	time averaged quantity
$< a >$	spatially averaged quantity
$\tilde{a}$	phase averaged quantity
$\mathbf{a}$	vector or tensor quantity
a'	fluctuating component of a
a_e	value of a at edge of boundary layer
a_{RMS}	root mean square of a
a_H	value of a at location of maximum shape factor
a_r	value of a at location of boundary layer reattachment
a_s	value of a at location of boundary layer separation

a_t	value of a at location of boundary layer transition
a_x, a_y, a_z	streamwise, wall-normal, and spanwise components of $\mathbf{a}$

Dimensionless Quantities

Symbol	Description	Definition
AR	aspect ratio	b^2/A_w
sAR	semi-aspect ratio	b_s^2/A_s
C	contraction coefficient	$\Delta p/q_\infty$
C_L	lift coefficient	$L/(q_\infty A_w)$
C_l	sectional lift coefficient	$l/(q_\infty c)$
C_p	pressure coefficient	$(p-p_\infty)/q_\infty$
H_x	boundary layer shape factor	δ_x^*/θ_x
N_{eff}	effective number of independent samples	$T/(2T_{int})$
R_{aa}	autocorrelation coefficient of a	$\int_{-\infty}^{\infty} \frac{(a(t)-\overline{a})(a(t-\Delta t)-\overline{a})}{s_a^2} dt$
R_{ab}	cross-correlation coefficient of a and b	$\int_{-\infty}^{\infty} \frac{(a(t)-\overline{a})\left(b(t-\Delta t)-\overline{b}\right)}{s_a s_b} dt$
Re_a	Reynolds number; length scale a	$u_\infty a/\nu$
r	wind tunnel contraction ratio	A_1/A_2
St	Strouhal number	fc/u_∞
St_0	Strouhal number of central instability frequency	$f_0 u_\infty/c$
Tu	turbulence intensity	u'_{RMS}/u_∞

Roman Symbols

Symbol	Description	Units
A	planar control volume area	m^2
A_w	wing area	m^2
A_s	semi-wing area	m^2
A_1, A_2	wind tunnel contraction entrance and exit area	m^2
a	POD temporal coefficient	-
b	wing span	m

b_s	wing semispan	m
c	chord length	m
D_i	induced drag	N
E	POD modal energy	J
$\mathcal{F}_{aa}$	power spectral density of a	units of a^2 times s
$\widehat{\mathcal{F}_{aa}}$	power spectral density of a normalised by variance of a	s
f	frequency	Hz
f_0	central instability frequency	Hz
L	lift force	N
l	sectional lift force	$\mathrm{N\,m^{-1}}$
p	pressure	Pa
p_∞	free-stream pressure	Pa
q_∞	dynamic pressure, $\frac{1}{2}\rho u_\infty^2$	Pa
$\mathbf{S}$	velocity fluctuation snapshot matrix	$\mathrm{m\,s^{-1}}$
$\mathcal{S}$	symmetric part of the velocity gradient tensor	$\mathrm{s^{-1}}$
s_a	standard deviation of a	units of a
T	sampling time	s
T_{int}	integral time scale, $\int_0^\infty R_{aa}(t)dt$	s
$U(a)$	uncertainty of a (95% confidence level)	units of a
u_∞	free-stream velocity	$\mathrm{m\,s^{-1}}$
u, v, w	streamwise, wall-normal, and spanwise velocity components	$\mathrm{m\,s^{-1}}$
v_d	downwash velocity	$\mathrm{m\,s^{-1}}$
X, Z	chordwise and spanwise coordinates in chord-based coordinate system	m
x, y, z	streamwise, wall-normal, and spanwise coordinates in surface-attached coordinate system	m

Y	vertical coordinate	m

Greek Symbols

Symbol	Description	Units
α	angle of attack	$^\circ$
α_{eff}	effective angle of attack	$^\circ$
β	angular spanwise coordinate	rad
Γ	circulation	$\mathrm{m^2\,s^{-1}}$
γ	angle between camera optical axes	$^\circ$
Δ	change in quantity	-
δ_x^*	streamwise boundary layer displacement thickness, $\int_0^{y_e}(1-u/u_e)dy$	m
θ_x	streamwise boundary layer momentum thickness, $\int_0^{y_e}(1-u/u_e)u/u_e dy$	m
ζ	wind tunnel wall interference parameter	-
Θ	phase angle	rad
λ	wavelength	m
λ_2	second eigenvalue of $\mathcal{S}^2+\mathbf{\Omega}^2$	$\mathrm{s^{-2}}$
μ_i	lifting line parameter, $c\frac{\partial C_l}{\partial\alpha}/4b$	$\mathrm{m^{-1}}$
ν	kinematic viscosity	$\mathrm{m\,s^{-2}}$
σ_a	exponential growth rate of a	-
τ	skin friction	Pa
$\mathbf{\Phi}$	POD eigenfunction	-
Ω	skew-symmetric part of the velocity gradient tensor	$\mathrm{s^{-1}}$
ω	vorticity	$\mathrm{s^{-1}}$

Chapter 1

Introduction

Wings are used by both man and nature to generate lift across a wide range of flow conditions [2]. A wing is an object of finite span able to produce and transmit a lifting force when moving through a fluid [3]. The two-dimensional cross-section of a wing, usually a teardrop-like shape, is called an airfoil [4]. Despite the common purpose of generating lift, substantial differences exist between the flows of fluid over wings of different sizes and at different speeds. The chord Reynolds number ($Re_c = u_\infty c/\nu$), is the nondimensional parameter that relates the wing or airfoil chord length (c) to the freestream velocity (u_∞) and kinematic viscosity (ν) of the fluid [4]. The transition process from laminar to turbulent flow, which significantly influences the lift and drag produced by a wing or airfoil section, is greatly affected by the Reynolds number [2]. Thus, different wing designs are required to achieve optimal wing performance at different Reynolds numbers [2].

At chord Reynolds numbers less than 5×10^5, the boundary layer on an airfoil may remain laminar into the region of adverse pressure gradient, e.g., [2, 4]. When subject to an adverse pressure gradient, laminar boundary layers are more susceptible to separation than turbulent boundary layers, because turbulent boundary layers exchange momentum with the outer flow through advection, which increases their capacity to overcome adverse pressure gradients [5]. The occurrence of boundary layer separation typically leads to a decrease in lift and an increase in drag, e.g., [4, 6], both of which are major challenges for the design of efficient airfoils and wings that operate at low Reynolds numbers. Downstream of laminar boundary layer separation, the highly unstable separated laminar shear layer may undergo transition to turbulence through the convective amplification of disturbances, e.g., [7–9]. If the Reynolds number is sufficiently large and the angle of attack is sufficiently small, the separated turbulent flow can reattach to the airfoil surface, enclosing in a time mean sense a region of recirculating flow called a laminar separation bubble (LSB) [10]. Due to the change in airfoil pressure distribution that the LSB causes, the lift to drag ratios attainable

at low Reynolds numbers are much lower than those attainable at higher Reynolds numbers where the boundary layer transitions to turbulence before the adverse pressure gradient and remains attached [4]. At very low Reynolds numbers ($Re_c \lesssim 5 \times 10^4$) or high angles of attack, transition in the separated laminar shear layer may be delayed to the extent that reattachment does not occur, stalling the airfoil and producing a more substantial reduction in performance, e.g., [2, 11]. Since the transition process in the separated shear layer is very sensitive to the angle of attack, Reynolds number, and disturbance environment, small changes in any of these conditions can cause dramatic changes in lift and drag, especially if these changes cause the separated shear layer to fail to reattach, e.g., [12–14]. Such behaviour is undesirable in the design of aircraft operating at low chord Reynolds numbers, since controlled flight must be maintained during manoeuvring and varying environmental conditions [15].

LSBs are not confined simply to the domain of aircraft wings, but are prevalent in a diverse array of technological applications. These include the blades of small wind turbines, e.g., [16], low pressure turbine stages in gas turbine engines, e.g., [17], and circular cylinders in crossflow, e.g., [18]. In most situations where LSBs form, three-dimensional flow is present at wing or turbine blade tips and roots. Notably, the flow development around wingtips involves the formation of wingtip vortices, which cause a reduction in lift and an increase in drag through their influence on the flow along the entire wingspan [19, 20]. The relative importance of wingtip vortices on overall wing performance is related to the wing aspect ratio (AR), defined as the wingspan squared divided by wing area (b^2/A_w). For cantilevered wings, the semi-aspect ratio (sAR) is defined using the wing semispan and semi-wing area (b_s^2/A_s). Generally, wings with smaller aspect ratios experience more severe lift reduction from wingtip vortices than wings with larger aspect ratios at the same angle of attack. The adverse effects of both LSBs and wingtip vortices can compound for small unmanned aircraft, which operate at low chord Reynolds numbers and are equipped with low aspect ratio wings to minimise overall aircraft size [21]. Wingtip vortices have been observed to interact with LSB development on wings, suppressing laminar separation near the wing tips [22], and causing changes in LSB location [23].

Despite the large number of studies that have focused on the structure and dynamics of LSBs on nominally two-dimensional geometries such as airfoils and flat plates, e.g., [7–11, 14, 24–27], relatively little attention has been given to the influence of tip effects on LSB formation, even though tip effects are present in most practical applications where LSBs occur. The influence of tip effects becomes especially important at low aspect ratios, where three-dimensional flow may extend over a large portion of a wing surface [28]. Because three-dimensional tip effects can change the stalling characteristics of and maximum lift produced by a wing when compared to a two-dimensional airfoil [29], it is important to understand the characteristics of LSBs in three-dimensional flow conditions near wingtips. While previous studies have investigated the surface topologies of three-dimensional LSBs, e.g., [28, 30], the three-dimensional flowfields of LSBs on finite wings remain largely unexplored. Adequate knowledge of the three-dimensional topology and dynamics of LSBs on finite wings is essential to understanding the mechanisms by which wing performance is affected in real-world flows subject to three-dimensional wingtip effects.

1.1 Study Objectives and Outline

The overall goal of this study is to quantitatively assess how an LSB on a finite wing is influenced by the three-dimensional wingtip effects. To this end, the laminar separation bubble forming on a semispan wing is investigated experimentally using surface pressure measurements and particle image velocimetry (PIV). The LSB forming on the wing is compared to an LSB forming on a reference two-dimensional airfoil geometry to elucidate the similarities and differences between LSBs that form under the influence of wingtip effects and those that form on nominally two-dimensional geometries. Thus, the extent to which the characteristics of LSBs explored in previous studies are representative of three-dimensional LSBs similar to those that exist in practical applications can be assessed. The specific research objectives of this study are as follows:

- Quantify the extent to which the presence of a wingtip causes LSB properties on a finite wing to differ from LSB properties on a two-dimensional airfoil.
- Determine the three-dimensional topological structure of an LSB forming on a finite wing.
- Characterise the spanwise evolution of the LSB on a finite wing and the influence of the wingtip on the laminar-to-turbulent transition process.

The remaining chapters of this thesis are organised as follows. Chapter 2 provides background information about LSBs and a survey of previous studies relevant to LSB formation on finite wings. Chapter 3 details the methodology used in this experimental investigation, while Chapters 4 and 5 present the results and discussion of the experiments. Conclusions and recommendations are presented in Chapter 6.

Chapter 2

Background

Laminar separation bubbles have been the subject of numerous experimental and numerical investigations, of which the majority relate to two-dimensional flow geometries. The most pertinent findings from the literature on two-dimensional airfoils at low Reynolds number as they relate to LSB flow development are reviewed in Section 2.1. Specific attention is given to the transition from laminar to turbulent flow, which dominates the dynamics of LSBs, in Section 2.2. Section 2.3 discusses some of the fundamental differences between two-dimensional and three-dimensional boundary layer separation. Section 2.4 provides a background on the effects of finite wingspan on the flow development over lifting surfaces. Finally, Section 2.5 reviews previous investigations of three-dimensional LSBs on finite wings.

2.1 Airfoils at Low Reynolds Numbers

The performance of airfoils in the low chord Reynolds number regime $Re_c < 5 \times 10^5$ is substantially influenced by laminar boundary layer separation [2], which commonly reduces lift, increases drag, and can cause abrupt stall [4]. Jones [31] was the first to attribute the phenomenon of leading edge stall to the presence of a local region of separated laminar flow near the leading edge of an airfoil. Leading edge stall occurs when the boundary layer on the suction surface of an airfoil suddenly fails to remain attached downstream of the leading edge. The relationship between boundary layer characteristics and airfoil performance was further investigated by McCullough & Gault [32] in their study on airfoil stall using detailed boundary layer velocity measurements. They concluded that the abrupt loss of lift and increase in drag associated with leading edge stall occurred when the separated laminar shear layer near the leading edge suddenly failed to reattach to the suction surface as the

angle of attack was increased. This sudden expansion of the region of separated flow is called bubble bursting [12]. McCullough & Gault [32] also discovered that before bursting, the mean locations of separation and reattachment move upstream with increasing angle of attack, while the overall length and height of the LSB decreases.

Prediction of the bursting phenomenon was the focus of the investigation of Gaster [12], who demonstrated that bursting could occur due to either an increase in angle of attack or a decrease in Reynolds number. Bubble bursting is responsible for the substantial reduction in maximum lift to drag ratios attainable at Reynolds numbers less than 1×10^5 [6]. To predict bubble bursting, Gaster [12] suggested a two-parameter criterion based on the momentum thickness Reynolds number at separation (Re_{θ_s}) and a pressure gradient parameter ($P = \theta_s^2/\nu(\Delta u_e/\Delta x)$) defined using the mean edge velocity gradient ($\Delta u_e/\Delta x$) across the LSB.

Mueller [33] observed that bubble bursting causes hysteresis in airfoil lift, such that post-stall reattachment of the separated shear layer and the associated recovery of lift requires a decrease in angle of attack below the initial bursting angle. Lift hysteresis presents major challenges to the control and stability of flying vehicles at low Reynolds numbers [34].

In his investigation into the growth and bursting of LSBs, Horton [7] proposed the overall mean LSB structure shown in Fig. 2.1. Between the locations of mean separation and mean reattachment is a region of recirculating flow. The mean dividing streamline, defined as the locus of points under which there is zero net streamwise mass flux, delineates the extent of the recirculation region [7]. Although the transition from laminar to fully turbulent flow in the separated shear layer occurs over a finite streamwise length, e.g., [9, 26, 35], a transition point is usually defined in the region where the mean dividing streamline begins to curve back towards the airfoil surface [36]. The upstream portion of the bubble is called the dead-air region, where the velocity of the recirculating flow is small and relatively steady, [7, 12, 37]. In the downstream portion of the bubble, the mean reverse flow velocity is stronger, forming a reverse flow vortex.

Figure 2.2 shows the typical influence of a suction surface LSB on the mean surface pressure coefficient ($C_{\overline{p}}$) as a function of chordwise distance (X) on an airfoil at low chord Reynolds number and moderate pre-stall angle of attack. Laminar boundary layer separation causes a plateau of relatively constant pressure to form in the region of adverse pressure gradient downstream of the suction peak [7]. The beginning of the pressure plateau occurs at the separation location, while the end of the plateau occurs at the mean transition point [7, 10]. Following transition, a rapid pressure recovery occurs up to the mean reattachment point [7].

The disturbance environment has a substantial influence on LSB formation and airfoil performance at low Reynolds numbers. Millikan & Klein [38] identified differences between measured maximum lift coefficients of airfoils in different wind tunnels and attributed these differences to differing levels of free-stream turbulence, which affected the location at which transition occurred. Higher maximum lift coefficients were observed when the boundary layer became turbulent upstream of the strong adverse pressure gradient on the suction surface, precluding the formation of an LSB. O'Meara & Mueller [13] determined that when

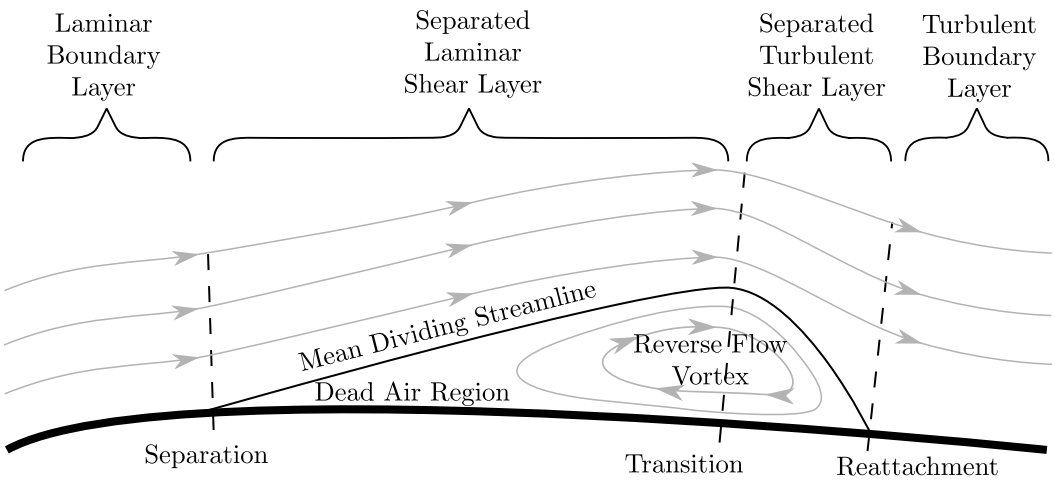

Figure 2.1: Schematic of mean laminar separation bubble structure adapted from Horton [7].

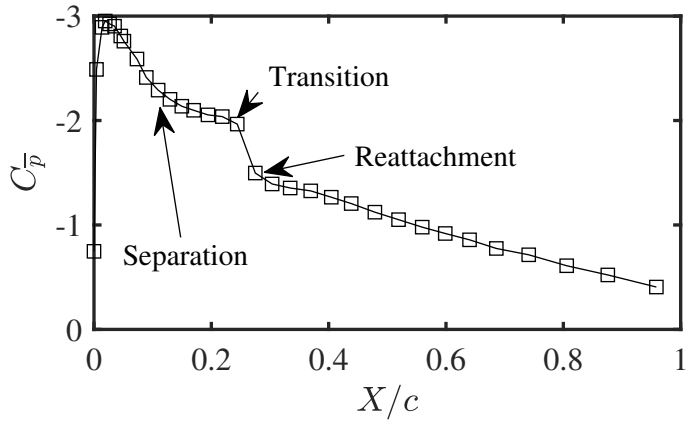

Figure 2.2: Representative suction surface pressure distribution on an airfoil with an LSB, from Boutilier & Yarusevych [14], on a NACA 0018 airfoil at $\alpha = 8°$ and $Re_c = 1.5 \times 10^5$.

an LSB does form on an airfoil, increased levels of turbulence intensity cause a reduction in LSB size. Furthermore, Istvan & Yarusevych [27] and Hosseinverdi & Fasel [39] have shown that increased levels of free-stream turbulence reduce the coherence of vortical structures formed during transition from laminar to turbulent flow in the aft portion of an LSB. Therefore, the sensitive nature of the transition process requires the use of experimental facilities with sufficiently low levels of ambient disturbances for the accurate prediction of free-flight airfoil performance [2].

2.2 Transition in Laminar Separation Bubbles

Transition from laminar to turbulent flow in the separated shear layer is responsible for boundary layer reattachment in LSBs [13]. Therefore, the dynamics of the transition process

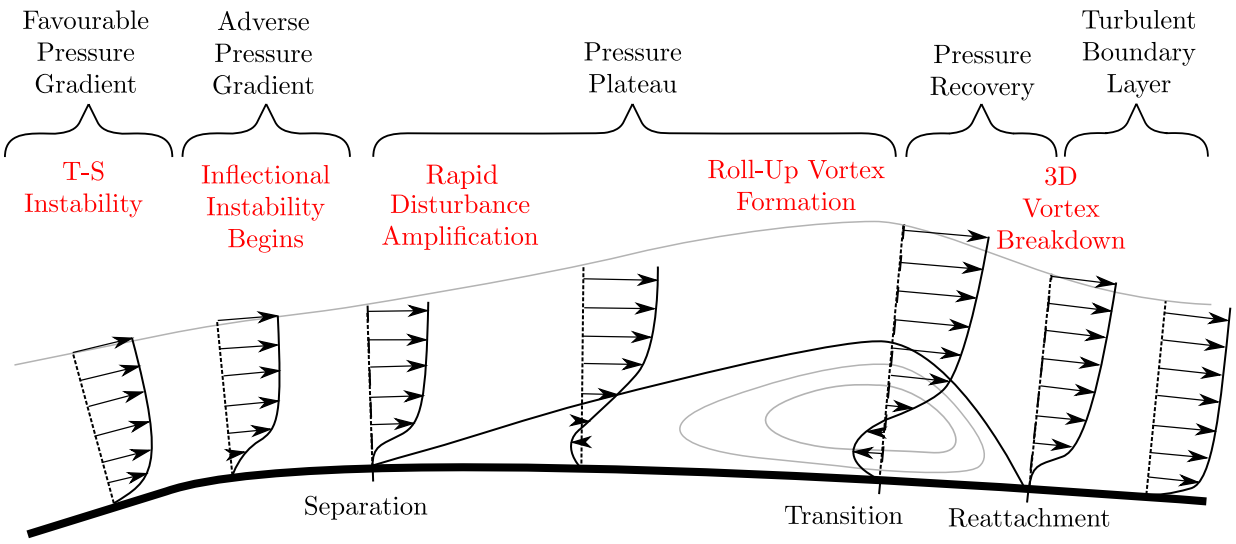

Figure 2.3: Streamwise velocity profiles typical of an LSB

plays a crucial role in determining overall LSB characteristics. A general overview of the transition process is shown in Fig. 2.3. The transition process in an LSB begins upstream of separation, [35, 37, 40], similar to the initial stages of the transition process in an attached boundary layer.

Boundary layer transition begins with the receptivity process, which involves the perturbation of the boundary layer by free-stream disturbances such as sound or turbulence [41]. If the boundary layer is unstable, the disturbances are amplified and transition to fully turbulent flow may result. The amplification or damping of disturbances of infinitesimal amplitude is described by linear stability theory [42]. The foundation of classical linear stability theory is the Orr-Sommerfeld equation, versions of which were independently formulated by Orr [43] and Sommerfeld [44]. Tollmien [45] was the first to solve the Orr-Sommerfeld equation to determine the curve of neutral stability as a function of disturbance wavenumber and displacement thickness Reynolds number for a zero-pressure-gradient flat plate boundary layer. His results showed that, below a critical Reynolds number, all disturbances are damped, whereas above the critical Reynolds number, specific wavenumbers are unstable. Later, Schlichting [46] determined the growth rates of the unstable disturbances. These wave-like unstable disturbances, which amplify in the boundary layer, are called Tollmien-Schlichting (T-S) waves [5]. The small amplitude of T-S waves in a transitioning boundary layer makes their observation difficult, and the linear stability theory deveoped by Tollmien [45] and Schlichting [46] was viewed with scepticism [42] until the first experimental confirmation of T-S waves in a transitioning boundary layer by Schubauer & Skramstad [47]. At low free-stream turbulence levels, the amplification of T-S waves is responsible for the initial growth of disturbances in the boundary layer [41]. At higher levels of free-stream disturbances, bypass transition may occur if the formation of turbulent spots in the laminar boundary layer occurs faster than the amplification of T-S waves [41].

If the developing boundary layer remains laminar into a region of adverse pressure

gradient, as is the case when an LSB forms, a change in the primary instability mechanism takes place. The amplification of T-S waves, which occurs due to the destabilising effect of viscosity in the boundary layer, is gradually superseded by the inviscid Kelvin-Helmholtz (K-H) instability mechanism as the primary disturbance amplification mechanism [8]. The K-H instability occurs when an inflection point exists in the velocity profile of a shearing flow. When a boundary layer encounters an adverse pressure gradient, such an inflection point occurs (Fig. 2.3) [5]. Lord Rayleigh [48] mathematically proved that an inflection point is a necessary condition for instability in inviscid flows. Furthermore, Fjørtoft [49] demonstrated that the sufficient condition for inviscid instability is the occurrence of a local maximum in vorticity at the inflection point. This inflectional instability mechanism, which is active in both viscous and inviscid flows, is also the primary instability mechanism in free shear layers [50].

At the start of the region of adverse pressure gradient on an airfoil, the inflection point in the streamwise velocity profile of the laminar boundary layer is located close to the airfoil surface [51]. Michalke [52] used linear stability theory to demonstrate that, for an inflectionally unstable shear layer, disturbance growth rates are reduced when the inflection point in the streamwise velocity profile is close to a wall. Downstream of separation, the inflection point in the streamwise velocity profile of an LSB moves away from the airfoil surface as the region of reverse flow develops. The stability analysis of Michalke [52] showed that disturbance growth rates increase significantly when the inflection point is farther from a wall or when reverse flow is present. The decreasing stability of the separated shear layer with increasing wall-normal distance was also confirmed experimentally by Brendel & Mueller [36], who measured a decrease in the distance between separation and transition under conditions where the separated shear layer was farther from the airfoil surface, implying a more rapid growth of disturbances, in agreement with Michalke [52]. Furthermore, the hot-wire anemometry measurements of Brendel & Mueller [36] indicated that amplified disturbances in the separated shear layer belong to a well-defined band of unstable frequencies, centred around a fundamental instability frequency.

In LSBs, the T-S mechanism governs the initial amplitudes of disturbances that are convected into the separated laminar shear layer for further amplification by the K-H instability mechanism [8, 40]. Using hotwire anemometry in an LSB on a flat plate, Diwan & Ramesh [8] observed that the location of maximum production of disturbance energy gradually moves away from the wall and begins to coincide with the inflection point in the streamwise velocity profile near the separation point, which indicates that the K-H instability mechanism progressively becomes the dominant instability mechanism near separation. Diwan & Ramesh [8] concluded that the amplification of disturbances in the separated laminar shear layer by the inviscid K-H mechanism is similar to a free shear layer near the location of maximum LSB height, where the inflection point is farthest from the surface. The velocity measurements and linear stability analysis of Boutilier & Yarusevych [51] also demonstrated that disturbance development in an LSB is well modelled by inviscid linear stability theory, with viscosity causing only a mild reduction to disturbance growth rates in the separated laminar shear layer.

As the amplitudes of disturbances in the separated laminar shear layer grow, nonlinear

effects cause the shear layer to roll up into vortices. This was observed by Watmuff [37], who conducted phase-averaged hot-wire velocity measurements of an LSB forming on a flat plate and characterised the evolution of an impulsive disturbance introduced into the boundary layer upstream of separation. As the disturbance amplified downstream, it caused the separated shear layer to roll up into vortices typical of those associated with the K-H instability. Roll-up vortex formation in the aft portion of LSBs has also been observed in numerous other numerical, e.g., [24, 26, 53–55], and experimental studies, e.g., [11, 36, 56, 57].

The roll-up vortices in LSBs on airfoils at low free-stream turbulence intensities are initially two-dimensional with a high degree of spanwise coherence, as detailed in the smoke-wire visualisations and spanwise correlation coefficient estimates of Kirk & Yarusevych [57] at a turbulence intensity (Tu) of less than 0.2%. Using hot-wire anemometry and smoke-wire visualisation, Yarusevych *et al.* [11] determined that roll-up vortices form at the frequency of the most amplified disturbances in the separated laminar shear layer, and that the frequency of the most amplified disturbances (fundamental frequency) increases with an increase in angle of attack or Reynolds number. At higher levels of free-stream disturbances, roll-up of the shear layer occurs with greatly reduced spanwise coherence, e.g., [27, 39, 58]. At a turbulence intensity of $Tu = 1.5\%$, Burgmann *et al.* [25] observed the formation of C-shaped vortices instead of the largely two-dimensional shear layer vortices seen at lower turbulence intensities. The formation of shear layer vortices is responsible for the highly unsteady mean recirculating flow in the aft portion of an LSB [57]. These vortices are responsible for bringing higher momentum fluid closer to the surface, which energises the boundary layer, enabling reattachment.

Similar to the transition process in free shear layers, vortex merging can occur between shear layer roll-up vortices in LSBs, e.g., [50, 59, 60]. Since merging involves the formation of one vortex from two original vortices, vortex merging is associated with the amplification of disturbances at half of the fundamental frequency [60]. Although vortex merging dominates the later stages of shear layer spreading in free shear layers [50], vortex merging in LSBs occurs irregularly and is suppressed by the proximity of the wall [11, 59].

The later stages of transition in an LSB involve three-dimensional deformation of the shear layer vortices and subsequent breakdown to turbulence [56]. Several instability mechanisms have been proposed to explain the three-dimensional breakdown of initially two-dimensional shear layer vorticies. Using direct numerical simulations (DNS), Marxen *et al.* [61] identified the presence of a Görtler instability in the upstream portion of a laminar separation bubble [61]. Görtler instability results in the formation of streamwise vorticity due to the centrifugal forces caused by boundary layer separation [61, 62]. Marxen *et al.* [26] also suggested that the presence of an elliptic instability of the shear layer vortex cores and a hyperbolic instability in the region between the vortices could be responsible for spanwise vortex deformations that lead to fully turbulent flow. Deformation of the shear layer vortices produces components of streamwise and surface-normal vorticity that lead to three-dimensional turbulence in the reattaching shear layer [56]. Furthermore, Rodríguez & Theofilis [63] showed that a stationary global instability can cause spanwise waviness in the locations of mean separation, mean reattachment, and the location of the mean

recirculation vortex core, producing corresponding spanwise deformations of the shear layer vortices. Regions of absolute inviscid instability [64], and the superposition of oblique and normal disturbance waves [40] have also been identified as possible causes for the onset of three-dimensional turbulence.

2.3 Three-Dimensional Boundary Layer Separation

The classical description of boundary layer separation in two-dimensional flows was introduced by Prandtl [65]. In two-dimensional flows, locations of boundary layer separation and reattachment are identified as points where the skin friction is zero. However, in three-dimensional flows, the skin friction may be non-zero at locations of separation and reattachment [66, 67]. The description of three-dimensional flows requires a generalisation of the concepts of separation points, attachment points, and dividing streamlines that are used to describe two-dimensional flows. In three dimensional flows, the analogous concepts are separation lines, attachment lines, and dividing surfaces, respectively. On a no slip boundary in a three-dimensional flow, one can define skin-friction lines, which are integral curves that are everywhere parallel to the local skin friction vector ($\boldsymbol{\tau}$) [66]. Under the hypothesis that the skin friction field is a continuous vector field, Legendre [68] introduced critical point theory to interpret the pattern of limiting streamlines (equivalent to skin friction lines) on the boundary. Critical points are singular points in a vector field where the magnitude of the vector field is zero [67]. The types of critical points and the integral curves connecting them define the topology of the vector field [66].

The critical points of a two-dimensional continuous vector field, such as the skin friction field on the surface of a three-dimensional body immersed in a fluid, can be divided into two categories: nodes and saddle points [66]. A node is a point that is common to an infinite number of integral curves (Fig. 2.4a) [66]. Nodes can further be sub-classified into nodal points and foci [66]. At a nodal point, all but one of the integral curves passing through the nodal point share a common tangent, while at a focus, there is no common tangent [66]. If the integral curves converge on a node such as depicted in Fig. 2.4a, the node is a node of separation. Alternatively, if the integral curves diverge from a node, the node is a node of attachment. Saddle points are critical points common to only two integral curves called separators, one approaching and one leaving the saddle point (Fig. 2.4b) [66, 67].

The topological theory of three-dimensional flow separation requires that separation lines are separators that begin at saddle points or limit cycles [69]. A limit cycle is a separation line that forms a closed curve on the boundary, having neither a start or end point. However, Wang [70] asserted that three-dimensional separation lines can occur that do not originate at a saddle point or limit cycle of the skin friction field. Instead, Wang [70] proposed that separation can also occur when limiting streamlines converge on an ordinary limiting streamline. This type of three-dimensional separation is called open separation or crossflow separation [69], because the separation surface from this type of separation appears as a half-saddle in a crossflow plane. However, a consensus has not been reached in the literature as to the definition of crossflow separation lines [69, 71]. One may attempt to

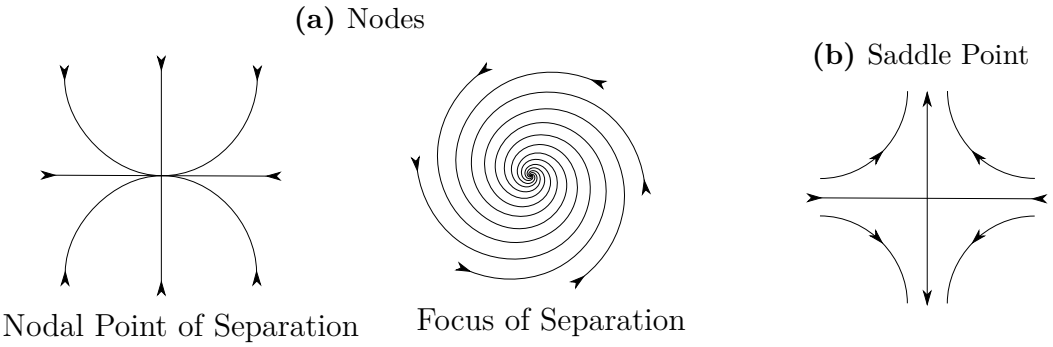

Figure 2.4: Types of critical points.

define a crossflow separation line as an ordinary skin friction line onto which other skin friction lines converge, but in a region of converging skin friction lines, all skin friction lines are converging on each other and a unique crossflow separation line cannot be defined [72]. Another difficulty in formulating a generally valid definition of crossflow separation lines is determining where a crossflow separation begins [73, 74]. In a numerical simulation of a tangent ogive cylinder at an angle of attack, Yates & Chapman [72] observed that crossflow separation began gradually, and did not correspond to a rapid change or extrema of the pressure or skin friction fields. The difficulty in establishing the onset of crossflow separation may contribute to the discrepancies in the locations of separation and reattachment reported in different studies of LSBs on finite wings. Wu *et al.* [71] proposed a general theory of flow separation based on boundary vorticity curvature that can be applied to both crossflow separations and separations originating at critical points, but their theory only produces separation lines that are tangent to the limiting streamlines when the skin friction field is linear [69]. Although a precise and universally applicable mathematical definition of crossflow separation has yet to be formulated, crossflow separation lines can often be heuristically identified in flow visualisations where there is strong convergence of nearby skin friction lines [75]. Due to the complex three-dimensional character of many real-world flows, the study of three-dimensional separation remains an area of active research, e.g., [30, 76–79].

2.4 Finite Aspect Ratio Wings

Many applications of low Reynolds number lifting surfaces, such as micro aerial vehicle wings [80], and small wind turbine blades [81], involve three-dimensional end effects at the wing or blade tip. At nominally pre-stall angles of attack, end effects usually reduce the lift produced by a finite wing [82]. The extent of three-dimensional flow on a lifting surface is related to the aspect ratio [3]. As the aspect ratio of a lifting surface increases, tip effects become less significant on overall performance [3].

The generation of lift by a lifting surface requires the establishment of regions of high and low pressure on opposite sides of the lifting surface. The presence of a wingtip creates a spanwise pressure gradient that reduces the difference in pressure between the suction and

(a) Spanwise flow on a finite wing.

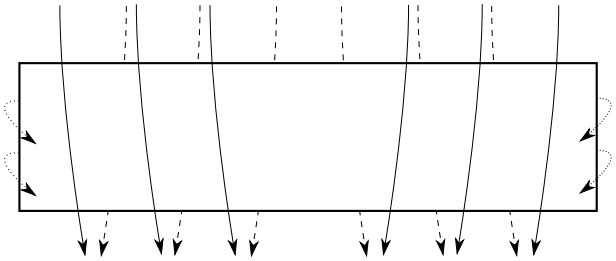

(b) Roll-up of trailing vortex sheet into wingtip vortices.

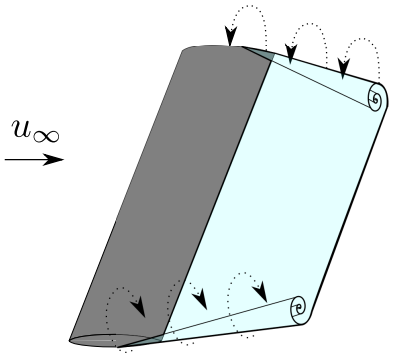

Figure 2.5: Production of trailing vorticity and wingtip vortices in the wake of a finite wing. Solid lines: streamlines over suction surface, dashed lines: flow over pressure surface, dotted lines: flow around wingtips.

pressure surfaces as the wingtip is approached. This spanwise pressure gradient results in spanwise flow [83]. On the suction surface, the spanwise flow is directed inboard towards the lower pressure region at the wing root or midspan. On the pressure surface, the spanwise flow is directed outboard, away from the highest pressure region near the wing root or midspan. Figure 2.5a shows the streamline curvature that results from spanwise flow on a finite aspect ratio wing. The spanwise flow leads to the generation of a trailing vortex sheet [83], which rolls up in the wake of the wing, forming wingtip vortices (Fig. 2.5b). The wing tip vortices induce a component of velocity perpendicular to the free-stream flow termed downwash [3, 83], which in general varies along the span of a wing and reduces the angle between the oncoming flow and the wing chord. Since the lift force is defined as the force that acts perpendicular to the oncoming velocity, the downwash creates a component of lift that is parallel to the free-stream. This is illustrated in Fig. 2.6, where the lift force (L') has a component (D_i) that is parallel to the free-stream because of the inclination of the local velocity vector due to the downwash (v_d). This component of the lift force that acts parallel to the free-stream creates a type of drag called induced drag, which is proportional to the square of the lift coefficient [3]. The local effective angle of attack (α_{eff}) is used to describe the local angle between the wing chord and the resultant oncoming flow at a given spanwise location, and is typically less than the geometric angle of attack (α). Figure 2.6 illustrates how the geometric and local effective angles of attack are defined relative to the direction of freestream velocity and local resultant velocity, respectively.

The spanwise distributions of lift and local effective angle of attack can be predicted using the lifting line theory developed by Lanchester [84] and Prandtl [20], which models a finite aspect ratio wing as a line of varying vortex strength called the bound vortex (Fig. 2.7). Because Helmholtz' vortex theorems require that the strength of a vortex filament be constant along its length [85], any change in the strength of the bound vortex must be accompanied by a trailing vortex filament of equivalent strength. Assuming that at every spanwise location the flow is locally two-dimensional, the sectional lift coefficient

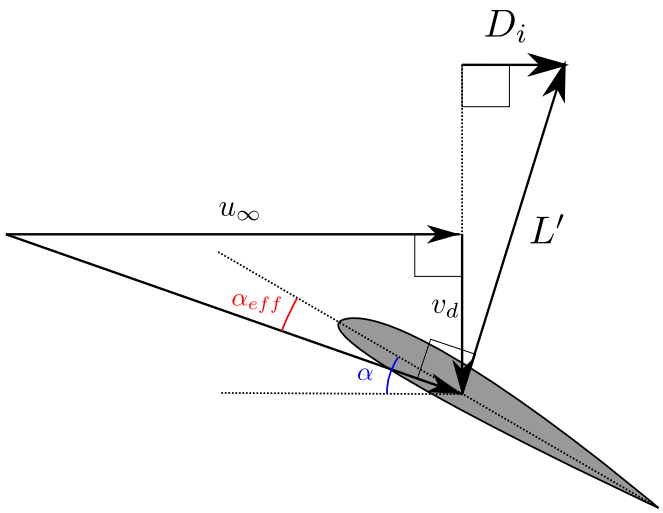

Figure 2.6: The geometric angle of attack (α) is the angle between the airfoil chord and the freestream velocity (u_∞). The local effective angle of attack (α_{eff}) is the angle between the chord and the resultant of the free-stream (u_∞) and downwash (v_d) velocities. Induced drag (D_i) is the component of the lift force (L') acting in the direction of the freestream velocity (u_∞).

(C_l) at any spanwise location on the wing can be calculated from the strength of the bound vortex at that location (Γ) and the freestream velocity, using the Kutta-Joukowski theorem [86]:

$$C_l = \frac{-2\Gamma}{u_\infty c} \tag{2.1}$$

The lift coefficient, and therefore the circulation, are proportional to the local effective angle of attack. For thin airfoils in inviscid flow, the relationship between angle of attack and lift coefficient is linear, and can be expressed as $C_l = (\partial C_l/\partial\alpha)\alpha$ [86]. When modelling a continuous distribution of lift along the span of a wing, the individual trailing vortex fillaments become a continuous trailing vortex sheet of varying strength. The downwash produced by the trailing vortex sheet at a given spanwise location (Z_0) on the Z axis of the wing (Fig. 2.7), can be found by integrating the downwash produced by the entire vortex sheet according to the Biot-Savart law [3]:

$$v_d(Z_0) = \frac{-1}{4\pi}\int_{-b/2}^{b/2} \frac{\frac{\partial\Gamma}{\partial Z}}{Z - Z_0} dZ \tag{2.2}$$

However, because the circulation is a function of the local effective angle of attack, an additional relationship between the downwash velocity and circulation is required to solve for the circulation distribution. Noting that $v_d \approx u_\infty(\alpha - \alpha_{eff})$ (Fig. 2.6) and $\alpha_{eff} = C_l/(\partial C_l/\partial\alpha)$, and using Eq. 2.1, Eq. 2.2 can be manipulated into the following

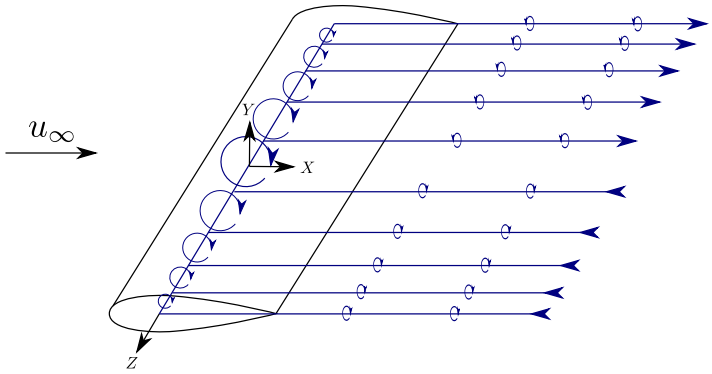

Figure 2.7: Lifting line model of a finite wing.

integral equation in terms of the bound vortex strength distribution along the span (Γ):

$$u_\infty \alpha = \frac{-1}{4\pi} \int_{-b/2}^{b/2} \frac{\frac{\partial \Gamma}{\partial Z}}{Z - Z_0} dz - \frac{2\Gamma}{\frac{\partial C_l}{\partial \alpha} c} \tag{2.3}$$

This equation can be converted to a system of linear equations in terms of the coordinate $\beta = \cos^{-1}(2Z/b)$ by expressing Γ as a Fourier sine series with coefficients A_n [3]:

$$\Gamma(Z) = 2u_\infty b \sum_{n=1}^{N} A_n \sin(n\phi) \tag{2.4}$$

By substituting Eq. 2.4 into Eq. 2.3, the following system of equations is obtained [3]:

$$\sum_{n=1}^{N} A_n \sin(n\beta_i)(\mu_i n + \sin(\beta_i)) = \alpha \mu_i \sin(\beta_i), \quad i = 1, 2, ..., N \tag{2.5}$$

where β_i denotes each of the N control points on the wing where Eq. 2.3 is satisfied, and $\mu_i = c_i(\partial C_l/\partial \alpha)/4b$ is a parameter that relates to the local geometric properties of the wing. By solving Eq. 2.5 for the coefficients A_n, the circulation, sectional lift, and effective angle of attack distributions can be determined for a straight wing.

Figure 2.8 shows the sectional lift distribution for a finite rectangular wing calculated using lifting line theory, normalised by the maximum lift coefficient. For a wing of finite span, the circulation, sectional lift, and effective angle of attack reduce to zero at the wingtips. This also means that the adverse pressure gradient on the suction surface (Fig. 2.2) is reduced near the wingtips. This is of great relevance to LSBs on finite wings, since the strength of the adverse pressure gradient is related to bubble bursting [12], and stability characteristics of the attached boundary layer and separated shear layer [8]. Also shown in Fig. 2.7 is the lift distribution calculated from surface pressure measurements on a rectangular Wortmann FX 63-137 semispan wing with a semi-aspect ratio $sAR = 2$ at a chord Reynolds number of $Re_c = 2 \times 10^5$ [87], which also displays a decrease in sectional lift coefficient near the wingtip. Because the lifting line theory models a wing as a single line, and does not account for the three-dimensional shape of real wings, the experimental

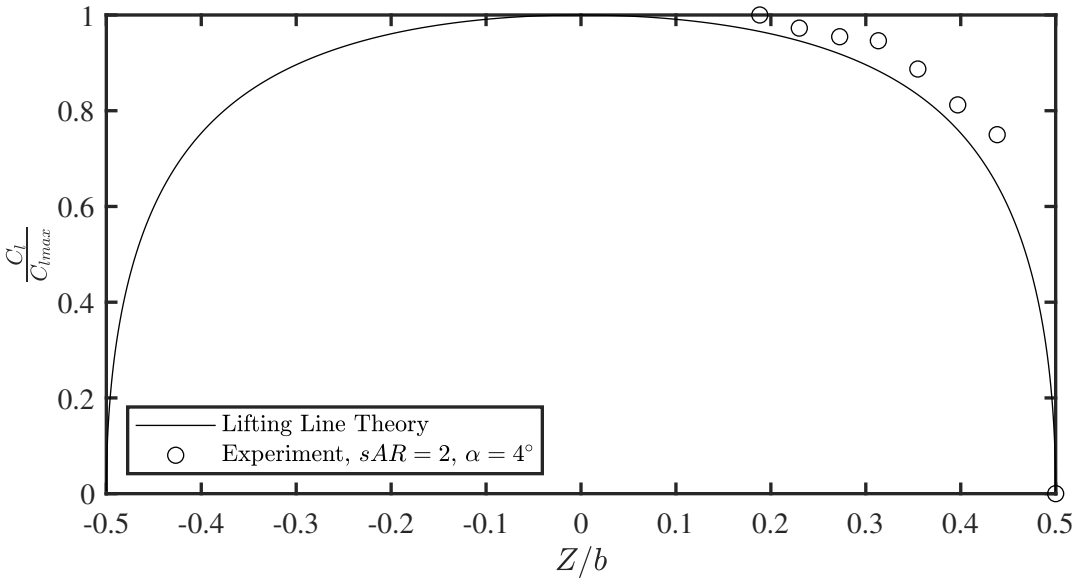

Figure 2.8: Sectional lift distribution on a rectangular wing. Experimental data from Bastedo & Mueller [87].

results deviate from the theory, especially near the wingtip. Lifting line theory is most accurate for wings with large aspect ratios, where three-dimensional effects are diminished [86].

2.5 Finite Aspect Ratio Wings at Low Reynolds Numbers

At low Reynolds numbers, finite wing performance is influenced by both wingtip vortices and laminar boundary layer separation [88]. Both of these phenomena contribute to non-linearities in the relationship between the wing lift coefficient (C_L) and angle of attack [29], which present a challenge for the control of small aircraft operating under variable environmental conditions [21]. On low aspect ratio wings, the reduction in lift and increase in drag caused by laminar boundary layer separation may be delayed to higher angles of attack by the energising effect of the wingtip vortices, which can prevent flow separation near the wingtips [29]. While many studies have investigated the influence of Reynolds number and aspect ratio on the overall lift and drag forces produced by wings experiencing laminar boundary layer separation, e.g., [29, 88–90], knowledge of the physical mechanisms underlying the interactions between three-dimensional wingtip effects and LSBs remains incomplete.

As illustrated in Fig. 2.8, the most significant spanwise variations in lift occur near the wingtips, while relatively small spanwise variations occur closer to the wing root or midspan ($Z/b = 0$). Similarly, the most substantial three-dimensional effects on the boundary layer of a finite wing are limited to the portions of the wing surface near the tips. One of the first

studies on low Reynolds number aerodynamics of finite aspect ratio wings was conducted by Marchman & Abtahi [89], on a full span finite wing with an aspect ratio of $AR = 8$ over a chord Reynolds number range of $7 \times 10^4 \leq Re_c \leq 3 \times 10^5$. Surface oil flow visualisations confirmed the presence of an LSB on the wing which was largely uniform over the majority of the span. Significant three-dimensionality in the flow visualisations was confined to approximately one chord length from the wingtips, reported to be similar to patterns seen at higher Reynolds numbers.

Huang & Lin [91] studied the flow field around a cantilevered NACA 0012 semispan wing with a semi-aspect ratio of $sAR = 5$ in the chord Reynolds number range $3.2 \times 10^3 < Re_c < 1.2 \times 10^5$. Using surface oil flow visualisation at $Re_c = 8 \times 10^4$, they classified the suction surface flow field into five different regimes based on angle of attack. In the first regime, for $\alpha \lesssim 0.1°$, laminar separation without reattachment was observed. Three-dimensional tip effects caused laminar separation to advance farther upstream near the wingtip, while the location of separation was largely uniform along the rest of the span. The upstream advance of laminar separation at the wingtip was also observed in the other four flow regimes, and was attributed to the adverse pressure gradient caused by flow passing over the sharp corner of the wingtip. In the second regime, for $0.1° \lesssim \alpha \lesssim 6.5°$, the separated laminar shear layer reattached to form an LSB. Near the wingtip, turbulent reattachment was delayed. The third regime, for $6.5° \lesssim \alpha \lesssim 7.5°$, was similar to the second regime, but the LSB moved farther upstream and the separation line became wavy. In the fourth regime, for $7.5° \lesssim \alpha \lesssim 11.5°$, both the laminar separation and turbulent reattachment lines advanced upstream near the wingtip, and turbulent separation began to occur near the trailing edge. In the fifth regime, for $\alpha \gtrsim 11.5°$, the separation line of the reattached turbulent boundary layer advanced farther upstream causing massive separation near the leading edge. In all five flow regimes, three-dimensional effects were most prominent near the wingtip and root, while the flow over the midspan of the wing remained essentially two-dimensional and followed the trends expected for two-dimensional LSBs. Huang & Lin [91] also conducted hot-wire measurements of the vortex shedding frequency in the wake of the wing at multiple locations along the span for Reynolds numbers between $1.5 \times 10^4 < Re_c < 3.7 \times 10^4$ and angles of attack of $\alpha = 0°$ and $\alpha = 3°$. They observed that a small reduction in wake vortex shedding frequency occurred near the wing root and wingtip, while the maximum wake vortex shedding frequency occurred near the midspan. At post-stall angles of attack, no significant spanwise variation in wake vortex shedding frequency was observed.

The spanwise variation of an LSB on a finite wing was investigated by Bastedo & Mueller [23], who studied a semispan Wortmann FX 63-137 wing with a semi-aspect ratio of $sAR = 2$ at $Re_c = 8 \times 10^4$ and 2.0×10^5 and quantified the reduction in effective angle of attack on the wing using surface pressure measurements on the wing and on the corresponding two-dimensional airfoil section. Comparing the chordwise pressure distributions from multiple spanwise locations on the wing with pressure distributions from the two-dimensional airfoil section, Bastedo & Mueller [23] concluded that, at spanwise locations away from the wingtips, the flow was only weakly three-dimensional, and the LSB on the wing was analagous to the LSB on the airfoil at the local effective angle of attack, thus confirming the two-dimensionality of the flow over the wing in the region away

from the wingtip. Bastedo & Mueller [23] reported that the decrease in effective angle of attack towards the wing tip produced a downstream shift in the locations of separation and reattachment of the LSB.

Chen *et al.* [92] conducted a numerical study on a semispan cambered thin plate wing with a semi-aspect ratio of $sAR = 6$ at a Reynolds number of $Re_c = 6 \times 10^4$ using the $k - \omega$ SST turbulence model and $\gamma - Re_\theta$ transition model. At an angle of attack of $\alpha = 5°$, an LSB formed on the suction surface. The LSB, which initially formed at the wing root, expanded along the span of the wing until $\alpha = 8°$, at which point it spanned the majority of the wing. The separation and reattachment locations of the LSB were relatively uniform along the inner portion of the span, while a spanwise flow of progressively increasing magnitude occurred within the dead air region of the LSB closer to the wingtip.

Horton [7] experimentally studied the influence of spanwise flow on a laminar separation bubble forming on a nominally infinite swept wing. The mean recirculation region of the LSB on the infinite swept wing contained substantial spanwise flow, forming a helical vortex. Horton [7] found that bubble bursting on the infinite swept wing could be predicted by applying the bursting criteria for two-dimensional LSBs to the component of velocity perpendicular to the leading edge, confirming independence between the chordwise and spanwise flow for the range of Reynolds numbers and sweep angles considered. Although no substantial changes to LSB behaviour on infinite swept wings were observed by Horton [7], the flowfield over finite wings is non-uniform in the spanwise direction, notably near the wingtip. This creates a dependence between the chordwise and spanwise momentum equations, which may cause LSB behaviour near a wingtip to deviate from the trends seen on nominally two-dimensional geometries.

Flow visualisations and quantitative measurements have shown that LSB formation on the inboard portion of finite wings is essentially two-dimensional. However, spanwise changes in LSB behaviour begin to occur near the wingtip which do not occur in two-dimensional flow geometries. Using surface oil flow visualisations, Bastedo & Mueller [23] reported a downstream shift in LSB separation and reattachment locations near the wingtip. This shift was attributed to the reduction in effective angle of attack near the wingtip. Genç *et al.* [93] also reported a similar downstream curvature of the LSB separation and reattachment locations near the wingtips of full span wings with aspect ratios of $AR = 1$ and 3.

However, the downstream shift in LSB location near the wingtip reported by Bastedo & Mueller [23] and Genç *et al.* [93] stands in contrast with the results of Huang & Lin [91], Chen *et al.* [92], and Awasthi *et al.* [22] who reported different three-dimensional flow patterns near the tips of finite wings at low Reynolds numbers. Considering that the identification of three-dimensional separation and reattachment lines remains an inexact pursuit, it is possible that these discrepancies are the result of incorrect or differing interpretations of similar surface oil flow patterns. Also, the apparent separatrices in surface oil flow patterns of LSBs can change depending on the duration of time over which the surface oil flow visualisation is performed [94]. As such, a generally valid topological description of the region of three-dimensional flow near the tip of a finite wing at low Reynolds number remains to be found.

Awasthi *et al.* [22] investigated the three-dimensional interaction between the wingtip

and LSB forming on a cantilevered NACA 0012 semispan wing with a semi-aspect ratio of $sAR = 0.5$ at a Reynolds number of $Re_c = 2.7 \times 10^5$. In contrast with Huang & Lin [91], Awasthi *et al.* [22] concluded from their surface oil flow visualisation that the wingtip vortex caused turbulent reattachment of the separated laminar shear layer to occur farther upstream at moderate angles of attack. Although the reported LSB reattachment line curved upstream towards the wingtip, the separation line remained parallel with the leading edge of the wing. Awasthi *et al.* [22] also conducted boundary layer and wake mean velocity measurements using a Pitot-static tube. Between the outboard end of the LSB on the suction surface and the region dominated by the wing-tip vortex, they observed a region with substantially reduced boundary layer thickness and reduced wake velocity deficit, suggesting an absence of laminar separation and a reduction of the streamwise adverse pressure gradient in this region. However, it is unclear from single point velocity measurements how these changes influence LSB transition dynamics near the wingtip. Three-dimensional end effects have been shown to influence attached boundary layer transition on low aspect ratio wings in the direct numerical simulation of Smith & Ventikos [95]. In their simulation, the wingtip vortex caused a reduction in the growth rate of Tollmein-Schlichting waves near the wingtip on the suction surface. Since the initial perturbations that convect into the separated shear layer of an LSB are amplified by the Tollmein-Schlichting mechanism [8], it is likely that spanwise variations in the amplitudes of disturbances also occur in LSBs on finite wings.

Using a multi-hole Pitot probe, Awasthi *et al.* [22] performed measurements of the direction of the local velocity vector to determine the variation in local effective angle of attack along the span of the $sAR = 0.5$ wing. They found that, in general, lifting line theory provided a reliable estimate of the local effective angle of attack on the outboard portion of the wing. However, near the wing root, where wall boundary layer effects became substantial, the measured local effective angles of attack were higher than those predicted by lifting line theory. Nonetheless, the observed general agreement of lifting line theory with the experimental data of Awasthi *et al.* [22] is remarkable considering the very low aspect ratio.

The topology of three-dimensional separation bubbles was studied by Kremheller & Fasel [30] using a three-dimensional displacement body to impose a streamwise and spanwise pressure gradient on a flat plate, producing a three-dimensional LSB similar to the LSBs found on low aspect ratio wings. Unlike the mean LSB topology in Fig. 2.1, this type of three-dimensional LSB was an open separation that exchanged fluid with the surrounding flow. According to the classification of surface flow topologies of Perry *et al.* [96], the topological structure of the three-dimensional LSB on the flat plate was an owl face of the first kind, illustrated in Fig. 2.9. An owl face of the first kind consists of two counter-rotating foci of separation at opposite ends of the separator emanating from a saddle point in the symmetry plane. This separation pattern was also observed in the oil flow visualisations of Liu & Hsiao [97], PIV measurements of Gresham *et al.* [98], and numerical simulations of Chen *et al.* [28] on thin low aspect ratio wings. These studies have revealed mean surface topologies for LSBs on low aspect ratio wings at low Reynolds numbers, but the relationship between three-dimensional LSB structure and dynamics remains to be explored.

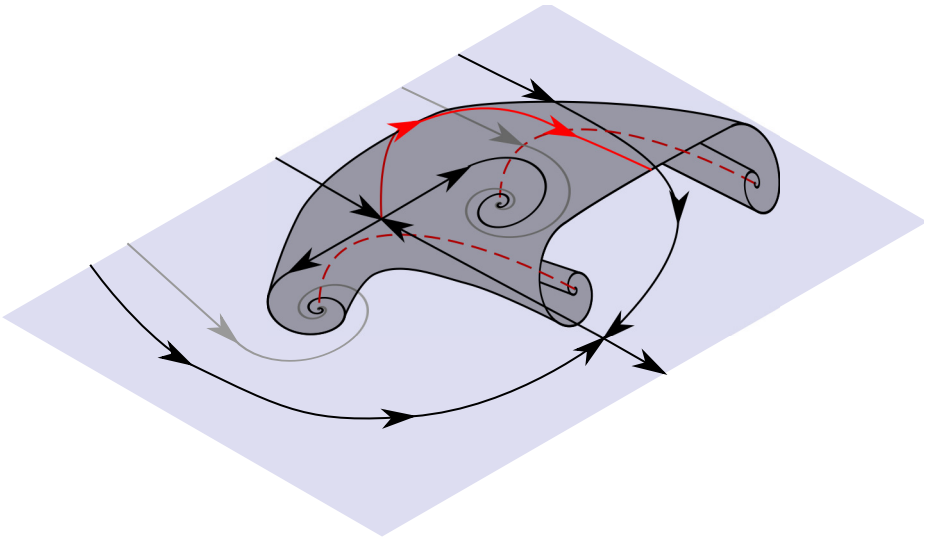

Figure 2.9: Owl face of the first kind. Black streamlines are separatrices on the boundary. Grey streamlines are ordinary streamlines on the boundary. Red streamline is on the separation surface. Red dashed lines follow vortex cores. Grey surface is the separation surface.

Chapter 3

Methodology

This investigation is an experimental study of the laminar separation bubble forming on the suction surface of a finite wing. The NACA 0018 airfoil model used in this investigation had previously been designed for the investigation of LSBs forming on two-dimensional airfoils [57, 99–104]. By cantilevering the model from one of the side walls of the test section of the University of Waterloo recirculating wing tunnel, finite wings of varying aspect ratio could be studied. After analysing the pressure distributions on wings with semi-aspect ratios between $sAR = 2.0$ and 2.75, a semi-aspect ratio of $sAR = 2.5$ was selected as the focus of this investigation, since this aspect ratio was the minimum needed to create a region of nominally two-dimensional flow away from the wingtip and wing root. Appendix D provides details on the pressure distributions of all wings tested. Particle image velocimetry (PIV) was the primary measurement technique used in this investigation, because it enables non-invasive measurement of the velocity field across a region of space. To produce an LSB on the suction surface of the wing with suitable length and height for the spatial resolution of the PIV measurements, a wing angle of attack of $\alpha = 6°$ and a chord Reynolds number of $Re_c = 1.25 \times 10^5$ were chosen as the baseline conditions for this investigation.

The wind tunnel and model set-up are described in Section 3.1, and the employed measurement techniques are detailed in Section 3.2. Section 3.3 outlines data processing methods performed on the data obtained from the experiments. A detailed analysis of the experimental uncertainties can be found in Appendix A, and a characterisation of the recirculating wind tunnel facility is provided in Appendix B.

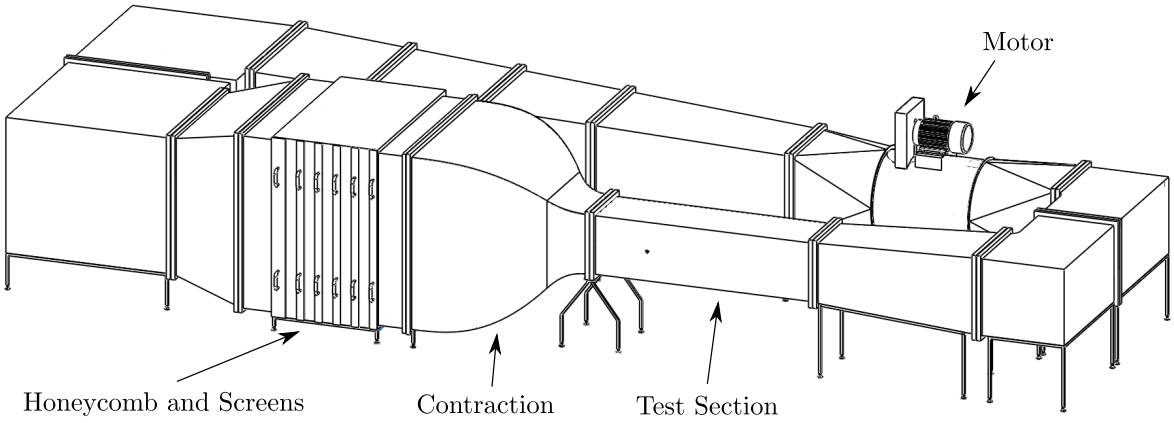

Figure 3.1: University of Waterloo recirculating wind tunnel.

3.1 Experimental Apparatus

All measurements were conducted in the recirculating wind tunnel at the University of Waterloo, shown in Fig. 3.1. The test section has a 0.61 m × 0.61 m square cross section, and is 2.44 m long. The wind tunnel is powered by a variable frequency alternating current electric motor which turns a six-bladed axial fan [102], capable of producing test section velocities up to 33 m s^{-1}. The freestream velocity in the test section was set according to a calibration of the pressure drop across the wind tunnel's 9:1 contraction. Upstream of the contraction, the flow is conditioned through an aluminium honeycomb and five wire-mesh screens [102]. To allow optical access to the test section, the walls of the test section are made of 9.53 mm thick glass. A detailed characterisation of the test section flow conditions is presented in Appendix B, and the main results are summarised here. All measurements were conducted at a chord Reynolds number of $Re_c = 1.25 \times 10^5$, which corresponds to a freestream velocity of approximately 9.5 m s^{-1}. At this velocity, the turbulence intensity in the empty test section measured using a single normal hotwire anemometer with the signal low-passed at 10 kHz was less than 0.08%. Applying Taylor's frozen turbulence hypothesis to the hotwire anemometer data [105], the integral length scale of turbulent fluctuations was estimated to be 40 mm, or 0.26c. The spatial variation of the freestream velocity over the test section cross-section was measured using a traversing Pitot-static probe, and found to be less than ±1.1% of the mean freestream velocity.

The anodised aluminium wing model used in this investigation was manufactured with a NACA 0018 airfoil section and a chord length of $c = 0.2$ m. Full details of the model's construction can be found in [99]. The wing model was cantilevered from one of the side walls of the test section as shown in Fig. 3.2, with a semispan of 0.5 m, resulting in a semi-aspect ratio of $sAR = 2.5$. The gap between the flat tip of the wing model and the opposite wall of the test section was 0.5c. The influence of the test section walls on the flow over the wing is analysed in Appendix C, where the differences between the experimental conditions and free-flight conditions are estimated quantitatively.

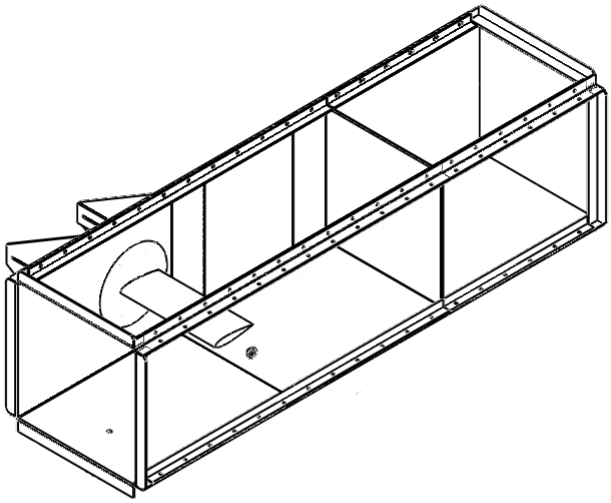

Figure 3.2: Wind tunnel test section with wing.

To enable direct comparison with flow development on a two-dimensional airfoil, a removable wing extension was installed in the gap between the tip of the aluminum wing model and the opposite wall of the test section, producing a nominally two-dimensional airfoil geometry by extending the span of the wing model across the entire width of the test section. The extension was made from a plastic block with a NACA 0018 profile that matched the profile of the aluminum wing model. The location of the wing extension is shown in Fig. 3.3. The model configuration with the extension installed is referred to as the airfoil, while the model configuration without the extension is referred to as the wing.

3.2 Measurement Techniques

3.2.1 Surface Pressure Measurements

Wing and airfoil surface pressure measurements were used to characterize the streamwise and spanwise pressure distributions on the wing, and estimate the effective angle of attack. Surface pressure measurements on the model were performed using 89 static pressure taps (0.4 mm in diameter), whose layout is shown in Fig. 3.3. For chordwise pressure measurements, the 65 staggered pressure taps centred at $Z/c = 0.95$ on both the suction and pressure surfaces were used. The remaining pressure taps are divided among three spanwise rows on the suction surface at $X/c = 0.15$, 0.30, and 0.60, and were used to measure the suction side spanwise pressure distribution. All pressure taps were connected to two Setra Model 239 pressure transducers with input ranges of ± 250 Pa, via two Scanivalve multiplexers. Two static pressure ports in the top and bottom walls of the upstream end of the test section were used as the reference freestream pressure (p_∞). Pressure transducer outputs were measured using a National Instruments USB-6259 data acquisition system. For all pressure measurements, a total of 4000 samples were acquired at each tap location at

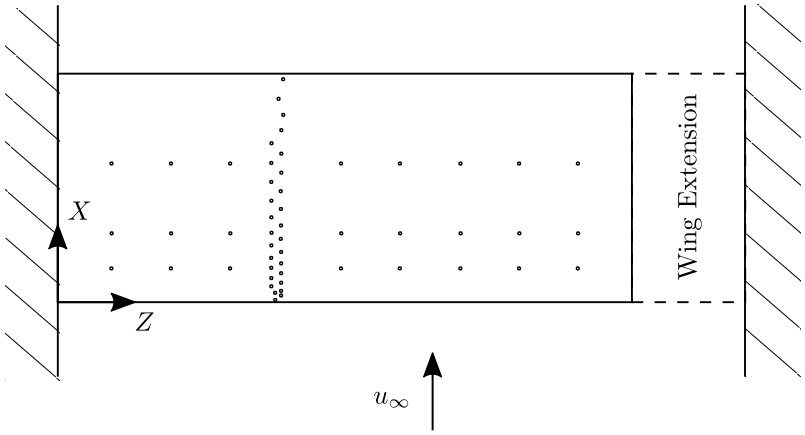

Figure 3.3: Locations of pressure taps on the wing model indicated by dots, viewed from the positive Y direction.

a sampling frequency of 1 kHz. The uncertainty in the obtained surface pressure coefficients was estimated to be less than 1.4% of the freestream dynamic pressure. Surface pressure measurements on the wing were taken with and without the presence of the PIV optics in the test section to verify that the optics had no measurable effect on the flow development over the wing.

3.2.2 Particle Image Velocimetry

Planar particle image velocimetry (PIV) was used to measure the velocity field of the LSB forming on the suction surface of the wing model. Planar PIV provides a minimally intrusive means for measuring the velocity of a fluid flow in a single measurement plane. A detailed overview of the technique can be found in Raffel *et al.* [106]. Essentially, PIV entails the use of a light source to illuminate small particles in a flowing fluid. The particles are imaged using one or more cameras at multiple instants in time, and the displacements of particles between images taken at different times are used to calculate the fluid velocity. In this investigation, illumination was provided by a sheet of laser light, enabling the cameras to image particles in a single plane. The laser light was formed into a sheet approximately 2 mm thick. For all PIV measurements, the flow was seeded with water-glycol based fog, and particle illumination was provided by a Photonics DM20-527 Nd:YLF pulsed laser. Synchronization of the camera shutters and laser trigger was performed using a LaVision programmable timing unit. The DaVis software from LaVision was used for image acquisition, preprocessing, and calculation of velocity fields from the particle images.

Two-Component PIV

Two-component (2C) planar PIV enables the measurement of the two velocity components parallel to the laser sheet, using images from a single viewing direction normal to the laser sheet. Two-component planar PIV measurements were performed in two different

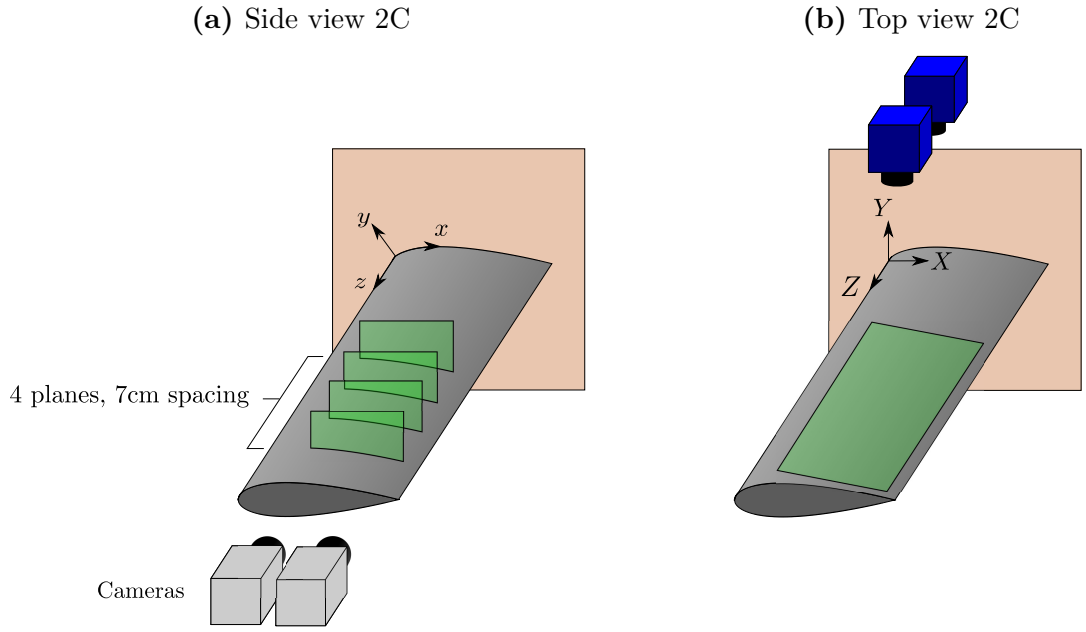

Figure 3.4: Light sheet orientations for 2C PIV and coordinate axes.

configurations referred to as the side view 2C configuration and the top view 2C configuration. Figures 3.4a and 3.4b show the orientation of the light sheet for the side view 2C and top view 2C configurations, respectively. Table 3.1 provides an overview of the PIV parameters of the side view 2C and top view 2C PIV configurations.

For the side view 2C configuration, the light sheet was positioned in $x - y$ planes at $z/c = 0.95$, 1.30, 1.66, and 2.01 (Fig. 3.4a), with the spanwise locations chosen to cover an area of the wing outside of the direct influence of root and tip flows, and to avoid laser light reflections from the pressure taps on the airfoil surface. At $z/c = 0.95$, the light sheet was positioned between the staggered pressure taps. The forming optics for the light sheet were located approximately $8c$ downstream of the model in the test section. Surface pressure measurements confirmed that the presence of the optics in the test section had no measurable influence on the flow over the model. In the side view 2C configuration, measurements were performed at the baseline angle of attack ($\alpha = 6.0°$) at all four spanwise locations for both the wing and airfoil model configurations. Furthermore, additional measurements at $z/c = 0.95$ were performed over a range of angles of attack, $3.8° \leq \alpha \leq 5.0°$, on the two-dimensional airfoil configuration covering the expected effective angle of attack range at the PIV measurement locations on the wing model configuration.

For the side view 2C configuration, two 1.0 Mpx Photron FastCam SA4 high-speed cameras operating in double frame mode were equipped with 200 mm fixed focal length macro lenses. The sensors of both cameras were cropped to 1024 px × 512 px. With an overlap of $0.016c$ (9%), the total field of view spanned $0.23 \leq x/c \leq 0.58$, and from the model surface to $y/c = 0.08$. A total of 5457 image pairs were taken at both 3.88 kHz and 0.3 kHz for spectral analysis and statistics, respectively. The corresponding sampling times were 1.41 s and 18.19 s, respectively. Based on the measured nominal vortex shedding period

within the LSB of 2 µs, over 1000 shedding cycles are captured within the time-resolved PIV measurements, while measurements at the lower sampling rate provide statistically independent samples for better convergence of velocity statistics.

Top view 2C measurements were conducted with the light sheet positioned tangent to but elevated from the suction surface of the wing, as shown in Fig. 3.4b. The light sheet was formed outside of the test section, and the closest distance between the light sheet and the surface of the wing model was $0.007c$. This distance was selected such that the measurement plane passed through the top halves of the shear layer vortices observed in the side view 2C measurements. Top view 2C measurements were conducted on both the finite wing and the two-dimensional airfoil configurations at $\alpha = 6.0°$.

To capture a larger field of view in the top view 2C configuration, two 5.5 Mpx LaVision Imager sCMOS cameras were used in double frame mode, equipped with 50 mm fixed focal length macro lenses. The camera sensors were cropped to 2560 px × 1492 px. With an overlap of approximately $0.059c$ (7%), the total field of view for top view PIV measurements covered the range $0.28 \leq X/c \leq 0.71$ and $0.93 \leq Z/c \leq 2.5$. For both the wing and the airfoil at an angle of attack of $\alpha = 6°$, images were acquired at 36 Hz, for a total of 4488 image pairs, corresponding to a sampling time of 124.67 s for each measurement set.

Calibration of the side view 2C and top view 2C configurations was performed by imaging a gridded calibration target. A least squares fit of a mapping function to the imaged calibration grid was used to map the image coordinates to physical coordinates. The side view configuration used a third order polynomial mapping function, while the top view configuration used a pinhole camera mapping function. These mapping functions were also used to perform perspective correction of the raw particle images before velocity calculations. Particle images were pre-processed using sliding minimum subtraction, with a sliding window width of 7 images. Velocity fields were then calculated from the images using multi-pass cross-correlation with window deformation [107]. The final interrogation window sizes were 16 px × 16 px and 24 px × 24 px for the side view 2C and top view 2C configurations, respectively, with 75% window overlap. The velocity fields were post-processed using iterative outlier detection and removal based on the median filter method [108]. The resulting vector fields were then stitched together using cosine blending in the overlap region. For data analysis and presentation, the side view velocity fields were transformed into the surface attached coordinate system (Fig. 3.4a).

Using the correlation statistics method [109], uncertainties in velocity due to random errors in the PIV measurements were estimated. The maximum RMS uncertainties in the side-view 2C measurements were estimated to be less than 8% and 6% of the freestream velocity for the streamwise (u) and wall-normal (v) velocity components, respectively. The maximum RMS uncertainties occurred near the wing surface upstream and downstream of the LSB, where a large velocity gradient occurs next to the surface. The maximum RMS uncertainties in the top view configuration were estimated to be 31% of the freestream velocity for both the streamwise (u) and spanwise (w) velocity components. The large values of maximum RMS uncertainties are due to localised regions of high noise caused by strong light reflections from the wing surface in the top view configuration. However, over the majority of the field of view, RMS uncertainties in the top view configuration were only

Table 3.1: Two-component PIV measurement parameters.

Parameter	Side View	Top View
Cameras	Photron FastCam SA4	LaVision Imager sCMOS
Sensor Resolution	1024px × 512px	2560px × 1492px
PIV Mode	Double Frame	
Frame Separation	60 µs	45 µs
Sampling Rate	3880 Hz and 300 Hz	36 Hz
Sampling Time	1.41 s and 18.19 s	124.67 s
Lens Focal Length	200 mm	50 mm
Magnification Factor	0.51	0.10
Combined Field of View	$0.35c \times 0.08c$	$1.57c \times 0.43c$
Laser	Photonics DM20-527 Nd:YLF	
Light Sheet Thickness	≈ 2 mm	
Seeding Particles	Water-Glycol Fog	
Final Interrogation Window Size	16 px × 16 px	24 px × 24 px
Window Overlap	75%	75%
Vector Pitch	0.16 mm	0.38 mm

4% for both the u and w velocity components (see Appendix A.3).

Two coordinate systems are used for PIV data presentation. For the side view 2C configuration, a surface attached coordinate system is used (Fig. 3.4a), with the positive x axis tangent to the suction surface in the streamwise direction, the positive y axis normal to the suction surface, and the positive z axis directed towards the wingtip, parallel to the leading edge. For presentation of data from the top view 2C configuration and surface pressure taps, a chord based coordinate system is used (Fig. 3.4b), with the positive X axis parallel to the wing chord, the positive Y axis in the vertical direction, and the Z axis identical to the z axis. Both coordinate systems have their origins at the wing root leading edge.

Three-Component PIV

Three-component (3C) planar PIV uses particle images taken from two different viewing directions to calculate the out-of-plane velocity component in addition to the velocity components in the plane of the light sheet [110]. To enable a three-dimensional reconstruction of the velocity field of the LSB forming on the suction surface of the wing near the wingtip, 3C PIV was conducted on 18 $x-y$ planes as indicated in Fig. 3.5. This configuration is referred to as the side view 3C configuration. Starting from the wingtip, side view 3C measurements were taken in planes with $0.05c$ (1 cm) spacing in the z direction from $z/c = 2.45$ to $z/c = 1.75$. Two additional side view 3C measurement planes were located at $z/c = 1.50$ and 1.25. All of the 15 planes with 1 cm spacing were acquired in a single run using an computer controlled traversing system with a nominal resolution of 0.1 mm

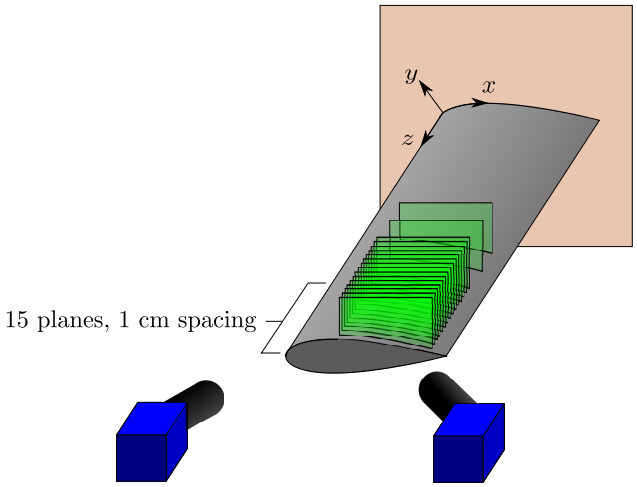

Figure 3.5: Side view 3C PIV measurement planes and coordinate axes.

to synchronously position the cameras and laser sheet. Side view 3C measurements were also conducted on the two-dimensional airfoil configuration using the wing extension at $z/c = 1.25, 1.50, 1.75, 1.90$ and 2.00.

Table 3.2 summarises the parameters of the side view 3C PIV system. Particle images were acquired with two LaVision Imager sCMOS 5 Mpx cameras, equipped with 200 mm fixed focal length Nikon macro lenses and Scheimpflug adapters, operating in double frame mode at 52.35 Hz. At each plane, 1000 image pairs were taken for a total sampling time of 19.10 s at each plane. The cameras were positioned as shown in Fig. 3.5. Due to physical limitations on camera positioning and optical access to the test section, the cameras were positioned with a narrow 35° angle between their optical axes, which increased the uncertainty in the out-of-plane velocity component relative to the in-plane components (Appendix A.3). The forming optics for the light sheet were set up identically as the side view 2C configuration, except that they were mounted on a computer controlled traverse. To mitigate the differences in particle image intensity due to forward and backward light scattering from the fog particles, the apertures of the upstream and downstream cameras were set to $f/5.6$, and $f/4$, respectively. The images from both cameras were cropped to 2560px × 1024 px, yielding a total field of view of approximately $0.3c \times 0.08c$. For each side view 3C measurement plane on the wing and the airfoil at an angle of attack of $\alpha = 6°$, 1000 image pairs were acquired at a frequency of 52.35 Hz, for a total sampling time of 19.10 s at each plane.

A two-level calibration target with grid markers on two $x - y$ planes separated by 1 mm in the z direction was used to calibrate the 3C PIV system. Calibration plate images were taken at the first plane in each traverse of the optical system. For every plane in the traverse, 3C PIV self calibration [111] was performed on the first 100 particle images using the calibration plate images from the first plane as an initial calibration. The final self-calibration interrogation window size was 128 px × 128 px, and the average remaining disparity between cameras was less than 2 px at each plane. At the end of the traverse, a second set of calibration images was taken to verify that the alignment of the cameras

Table 3.2: Three-component PIV measurement parameters.

Parameter	Value	
Sensor Size	2560px × 1024 px	
Field of View	$0.3c \times 0.08c$	
Lens Focal Length	200 mm	
Sampling Frequency	52.35 Hz	
Sampling Time	19.10 s	
Angle Between Optical Axes	35°	
Frame Separation	36 µs	
Freestream Particle Displacement	20 px	
Light Source	Photonics DM20-527 Nd:YLF Pulsed Laser	
Light Sheet Thickness	≈ 2 mm	
Particles	Water-Glycol Fog	
Final Interrogation Window Size	16 px × 16 px	
Window Overlap	75%	
Vector Pitch	0.096 mm	
	Upstream Camera	Downstream Camera
Aperture	$f/5.6$	$f/4$
Magnification Factor	0.246	0.253

was maintained during their translation. Using the width of the correlation peaks in the self-calibration correlation maps, the thickness of the light sheet was estimated to be 2 mm [111].

All 3C PIV particle images were pre-processed using global minimum subtraction and pixel intensity normalisation by the time-average pixel intensity before stereo self-calibration and vector calculation. Vector calculation was performed using an iterative multi-grid cross-correlation scheme with window deformation [107]. A window size of 16 px × 16 px with 75% overlap was used for the final pass, resulting in a vector pitch of 0.1 mm. Vectors were accepted if their stereo reconstruction error was less than 1 px. Velocity vector post-processing was performed using the universal outlier detection method of Westerweel & Scarano [112]. The resulting vector fields were interpolated onto the surface attached coordinate system (Fig. 3.5). The uncertainty in the side view 3C measurements due to random errors was estimated using the correlation statistics method [109]. The maximum RMS uncertainties, which occurred near the wing surface upstream and downstream of the LSB, where a large velocity gradient occurs, were 12%, 6.2%, and 27% of the freestream velocity for the u, v, and w velocity components, respectively. The RMS uncertainties within the LSB were approximately 2%, 2%, and 5% of the freestream velocity for the for the u, v, and w velocity components, respectively (see Appendix A.3).

3.3 Data Processing Techniques

3.3.1 Proper Orthogonal Decomposition

Proper orthogonal decomposition (POD) is a modal analysis technique that can be applied to unsteady fluid flows to extract dominant flow features [113]. POD was used to analyse the development of coherent structures using the method of snapshots introduced by Sirovich [114]. POD was performed on the fluctuating velocity field snapshots ($\mathbf{u}' = \mathbf{u} - \overline{\mathbf{u}}$) obtained by subtracting the mean flow from the instantaneous velocity field snapshots. The method of snapshots arranges the fluctuating velocity measurements taken at N instants in time into a snapshot matrix [115]:

$$\mathbf{S} = \begin{bmatrix} \mathbf{u'}_1(\mathbf{x}_1) & \mathbf{u'}_2(\mathbf{x}_1) & \dots & \mathbf{u'}_N(\mathbf{x}_1) \\ \mathbf{u'}_1(\mathbf{x}_2) & \mathbf{u'}_2(\mathbf{x}_2) & & \\ \vdots & & \ddots & \\ \mathbf{u'}_1(\mathbf{x_M}) & & & \mathbf{u'}_N(\mathbf{x}_M) \end{bmatrix} \tag{3.1}$$

where each of the columns of $\mathbf{S}$ contains the velocity fluctuations measured at M spatial locations at an instant in time. The cross-correlation matrix of $\mathbf{u}'$ is defined as [116]:

$$\mathbf{R}_{u'u'} = \mathbf{S}^T\mathbf{S} \tag{3.2}$$

POD is performed by solving the eigenvalue problem [116]:

$$\mathbf{R}_{u'u'}\mathbf{a}^{(n)} = E^{(n)}\mathbf{a}^{(n)}, n = 1 \dots N \tag{3.3}$$

to find a set of n orthonormal basis vectors ($\mathbf{a}^{(n)}$) for the cross-correlation matrix $\mathbf{R}_{u'u'}$. The eigenvalues ($E^{(n)}$) are the modal energies, and the entries of the orthonormal basis vectors are temporal coefficients ($a_i^{(n)}$) that represent the contribution of mode n to snapshot i of the fluctuating velocity field. The POD modes are conventionally sorted in the order of decreasing energy content ($E^{(n)}$), with the first mode ($n = 1$) corresponding to the highest energy content. The POD spatial modes ($\mathbf{\Phi}^{(n)}$) can then be determined from the linear combination of the temporal coefficients and the velocity snapshots [116]:

$$\mathbf{\Phi}^{(n)} = \frac{1}{\sqrt{E^{(n)}}} \sum_{i=1}^{N} a_i^{(n)} \mathbf{u'}_i \tag{3.4}$$

Finally, the original velocity field can be expressed using the POD modes [116]:

$$\mathbf{u}_i = \overline{\mathbf{u}} + \sum_{n=1}^{N} a_i^{(n)} \sqrt{E^{(n)}} \mathbf{\Phi}^{(n)}, \; i = 1 \dots N \tag{3.5}$$

In flows dominated by the convection of vortices, including LSBs, the dominant flow structures are captured in paired modes, which have similar energy content and their spatial

topology shifted in space by one-quarter of a wavelength [116–118]. Thus, POD is useful for analysing coherent structures.

Additionally, POD can be employed to produce phase-averaged flow reconstructions from non-time-resolved data [116–119]. In a fully deterministic periodic flow characterised solely by the convection of a vortex train with constant convection velocity and wavelength, the paired temporal coefficients $a^{(1)}$ and $a^{(2)}$ take the form [116]:

$$a_i^{(1)} = \sqrt{2/N}\cos(\Theta_i) \tag{3.6}$$

$$a_i^{(2)} = \sqrt{2/N}\sin(\Theta_i) \tag{3.7}$$

where Θ_i is the phase angle of the vortex shedding cycle captured in a given snapshot i. Therefore, the temporal coefficients of the paired modes can be used to sort non-time-resolved data samples according to the phase of the fundamental vortex shedding cycle [116, 117, 119] using the relation:

$$\Theta_i = \tan^{-1}\left(\frac{a_i^{(1)}}{a_i^{(2)}}\right) \tag{3.8}$$

While POD-based phase averaging is often conducted by binning the velocity snapshots falling withing a certain phase angle range [120], the polynomial fitting method of Lengani *et al.* [118] was adopted in the present study. This method involves applying a least squares 5^{th} order polynomial fit to the phase-sorted velocity data at each point in space. The polynomial fit provides a continuous relationship between phase angle and velocity at a given point. A distinct advantage of this method is that it minimizes the adverse effect of phase bin width (phase jitter) on the phase-average fields [118], because the polynomial fits are continuous functions of phase angle.

As discussed by Legrand *et al.* [120], for improved accuracy of phase averaging, the cumulative energy of a modal pair used for phase averaging should exceed 10% of the total energy of velocity fluctuations. Thus, unlike the standard POD performed on the two- or three-component velocity vector measured in a given plane, it is beneficial to do phase reconstruction using POD applied to the most dominant component of velocity fluctuations. In the present study, this was accomplished by using wall-normal fluctuations and streamwise fluctuations for phase averaging of the results obtained in side view 3C (Fig. 3.5) and top view 2C (Fig. 3.4b) configurations, respectively. The resulting cumulative modal energy of the first two modes for the side view 3C measurements was over 48% where distinct shedding was observed for the planes away from the wingtip ($z/c \leq 2.15$), as depicted in Fig. 3.6a, which depicts the relative energy (E_r) of the first twenty modes at $z/c = 1.25$. In the vicinity of the wingtip, the planes were considered for the phase averaging and reconstruction only where the relative cumulative energy of the most energetic pair reached 10%. For the top view 2C measurements, the first two modes captured 12% of the total fluctuating energy content (Fig. 3.6b).

Figure 3.7 depicts cross plots of a_1 and a_2 normalised by $\sqrt{N/2}$. Cycle-to-cycle variations

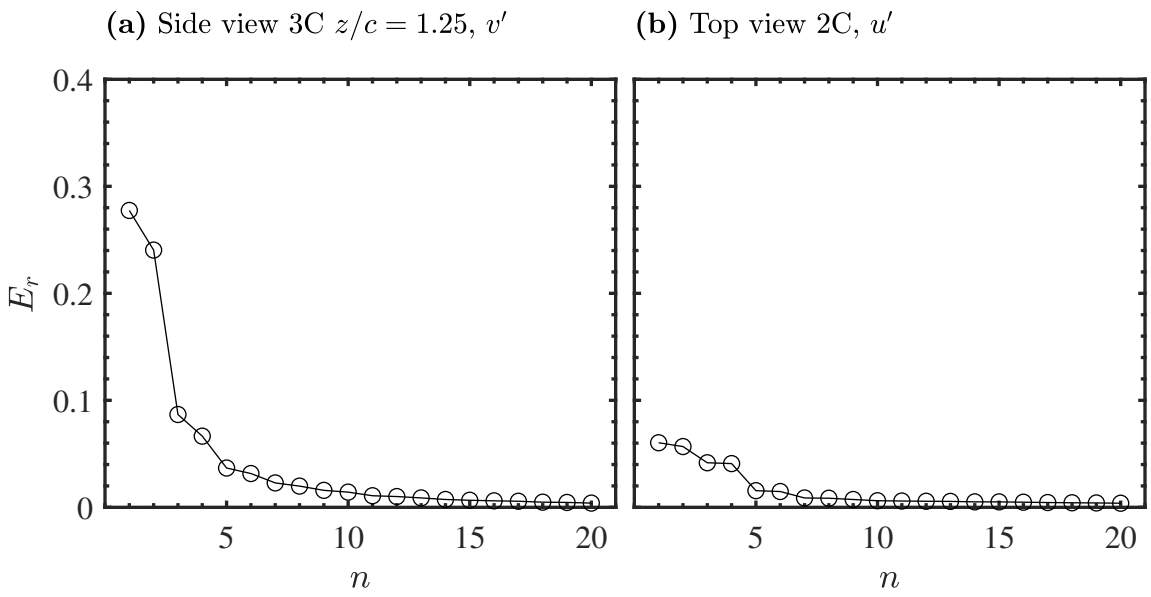

Figure 3.6: Representative relative modal energy distributions of the first twenty modes of the velocity fluctuation components used for phase averaging using polynomial fitting.

in the vortex shedding process produce substantial scatter of the experimental data away from the unit circle that represents the distribution expected for a perfectly periodic vortex train. The data scatter observed is similar to that of an unforced LSB on a two-dimensional airfoil [121]. Note that 1000 snapshots were used for POD in the side-view planes, while 4488 snapshots were employed for the top view, which is reflected in the number of data points in Figs. 3.7a and 3.7b. A convergence study of the POD modal energies was performed, and it was estimated that the relative energy of the most energetic mode pairs was converged to within 1% and 0.1% for the side view 3C and top view 2C configurations, respectively.

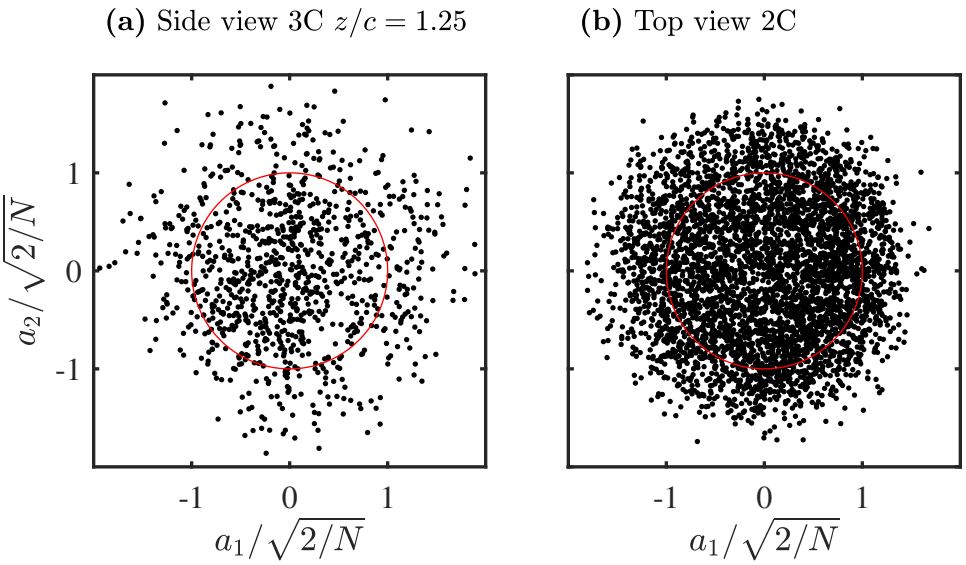

Figure 3.7: Cross plot of temporal coefficients of POD modes used for phase averaging. Unit circle in red.

Chapter 4

Comparison of Laminar Separation Bubbles on Airfoil and Finite Wing

Since the bulk of existing literature on LSB structure and dynamics has focused on two-dimensional LSBs, an investigation was conducted to compare the behaviour of LSBs forming on a two-dimensional airfoil and on a finite wing. The comparison focuses on the region away from the immediate vicinity of the wingtip, in which previous studies have reported that the flow over finite wings is essentially two-dimensional, e.g., [23, 89, 91]. Surface pressure and planar 2C PIV measurements are presented for a semispan NACA 0018 wing of semi-aspect ratio $sAR = 2.5$ at a geometric angle of attack of $\alpha = 6°$ and a chord Reynolds number of $Re_c = 1.25 \times 10^5$. The effect of the wingtip on flow development over the wing is quantified through examination of the resulting changes in effective angle of attack. Measurements performed using the two-dimensional airfoil configuration over a range of angles of attack encompassing the effective angles on the wing allow an examination of how LSB mean topology and dynamics on the wing are affected by the finite aspect ratio of the wing.

4.1 Surface Pressure Distributions

Figure 4.1a contrasts the chordwise surface pressure distributions on the wing and the airfoil at the same geometric angle of attack. For both cases, the pressure distribution on

Parts of this chapter have been adapted with permission from Toppings, C. E., Kurelek, J. W., & Yarusevych, S. April 2021 Laminar Separation Bubble Development on a Finite Wing. *AIAA Journal* (Articles in Advance), 1–13. DOI.

the suction side features a characteristic pressure plateau downstream of the suction peak, indicating the presence of an LSB [7]. Measurements on the pressure surface indicate that there is no LSB present on the pressure side of the airfoil. Figure 4.1a illustrates that the suction peak magnitude is reduced on the finite wing, e.g., [23, 92], and the accompanying changes in the pressure gradient result in the notable downstream shift of the pressure plateau. This indicates a downstream shift of the LSB on the wing, consistent with the expected decrease of the effective angle of attack [23].

Figure 4.1b shows the spanwise pressure distributions on the suction surface from the three spanwise rows of pressure taps. The location of the streamwise pressure taps are indicated by the dashed line in Fig. 4.1b, while pressures common to the measured streamwise and spanwise distributions are marked in Fig. 4.1a. From Fig. 4.1a, the rows at $X/c = 0.15$ and 0.60 are located upstream and downstream of the expected LSB location, respectively, while the middle row ($X/c = 0.3$) is located within the LSB. The airfoil configuration displays spanwise uniform pressure distributions at $X/c = 0.15$ and 0.60; however, an increase in suction on the airfoil within the LSB at $z/c = 2.25$ and $X/c = 0.30$ is observed. This increase is attributed to the high degree of sensitivity of LSBs to test environment perturbations [13], since the surface pressures outside of the LSB remain virtually constant across the span of the airfoil. For the wing configuration, suction side pressure magnitudes are decreased compared to those of the airfoil configuration, while a gradual decrease in suction is observed with increasing z/c (i.e., towards the wingtip), which is consistent with the expected spanwise pressure gradient on finite wings, e.g., [23, 122].

The results in Fig. 4.1a indicate that the sectional lift coefficients of the wing are lower than those of the airfoil, with the difference expected to increase as the wingtip is approached. This decrease in sectional lift is commonly represented as a decrease in the effective angle of attack [20]. Therefore, if an estimate of the spanwise variation in the effective angle of attack is available for the wing, then conditions under which the airfoil and wing models produce similar streamwise pressure distributions can be identified. At these conditions, LSB characteristics can be cross-examined between the airfoil and wing, allowing for the effect of the spanwise pressure gradient to be isolated.

4.2 Estimation of Effective Angle of Attack

The variation in the effective angle of attack along the span of the wing model at a geometric angle of attack of $\alpha = 6°$ is determined using the following procedure. First, a set of baseline pressure distributions is established for the airfoil over a range of geometric angles of attack. Then, for each spanwise location on the wing at which spanwise pressure taps are situated (= 0.25, 0.50, 0.75, etc.), the three data points available in the streamwise direction are compared with the airfoil data to identify the closest match. When the data are matched, the geometric angle of attack of the corresponding airfoil pressure data is taken as the effective angle of attack at the examined z/c location on the wing.

From an initial exploratory survey, the effective angle of attack on the wing in the

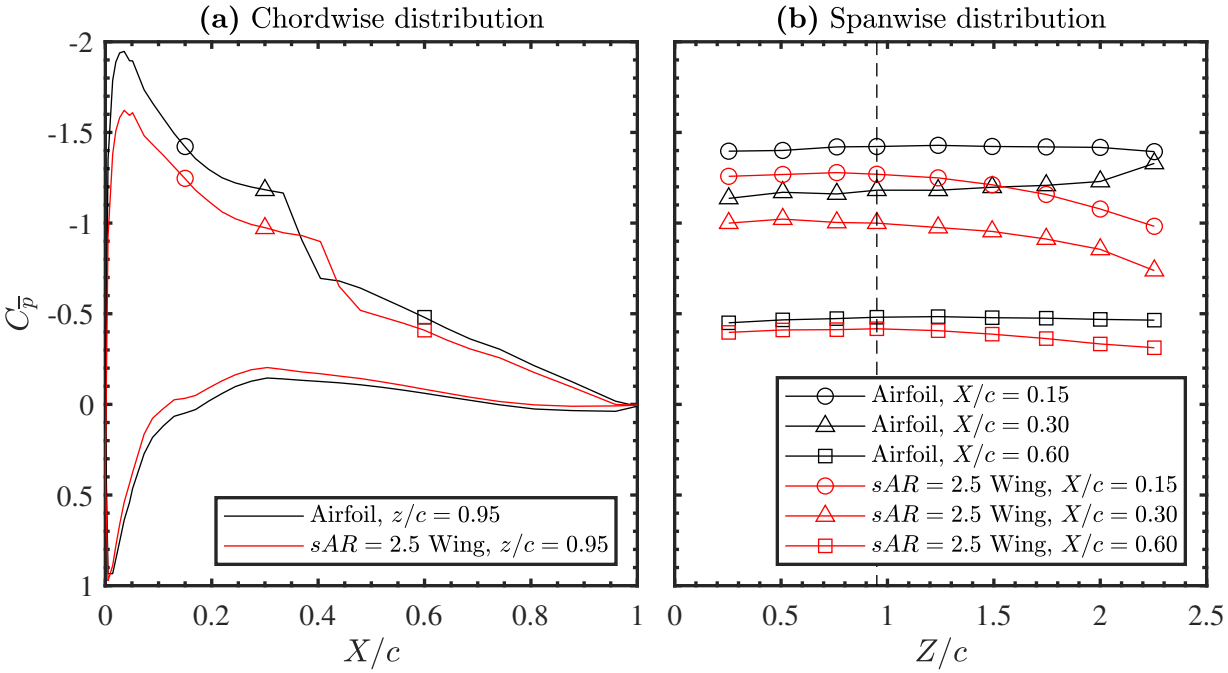

Figure 4.1: Surface pressure distributions at $\alpha = 6°$ on the wing and airfoil. Symbols in **(a)** mark measurements common to the streamwise and spanwise distributions. Dashed line in **(b)** shows the spanwise location of the measurements presented in **(a)**.

region of $0.95 \leq z/c \leq 2.01$ was estimated to fall in the range $4° \leq \alpha_{eff} \leq 5°$. Thus, a refined sweep of pressure measurements on the airfoil was performed around this angle of attack range, and the obtained data were used for a detailed matching procedure. First, the pressure data from the three pressure taps on the airfoil common to the streamwise and spanwise rows are considered, with Fig. 4.2 showing the pressure coefficients from these three locations plotted against α. Also plotted in Fig. 4.2 (inset plots) are streamwise pressure distributions for a select number of angles of attack. Given the nearly linear variation of the pressure coefficients within this range of angles of attack (blue lines in Fig. 4.2), the effective angle of attack on the wing is estimated at all Z/c locations at which pressure data are available by finding the value of α that minimized the sum of squared differences between the linear fits (determined from the airfoil pressure measurements) to the wing pressure measurements at a specific z/c location. This is illustrated in Fig. 4.3a, where the three pressure measurements at a single spanwise location on the wing (red markers) are shifted horizontally such that the sum of squares of Δ_1, Δ_2, and Δ_3 is minimized, thus identifying the effective angle of attack for this spanwise location. Figure 4.3b shows the result for all spanwise pressure tap locations on the wing. It should be noted that the wing pressure coefficients at the same three streamwise locations also exhibit a nearly linear variation with the effective angle of attack, supporting the employed approach.

Figure 4.4 presents the obtained variation of the effective angle of attack along the span of the wing, with the indicated uncertainly limits incorporating estimates of both the measurement and methodological uncertainty. The locations of the PIV measurement

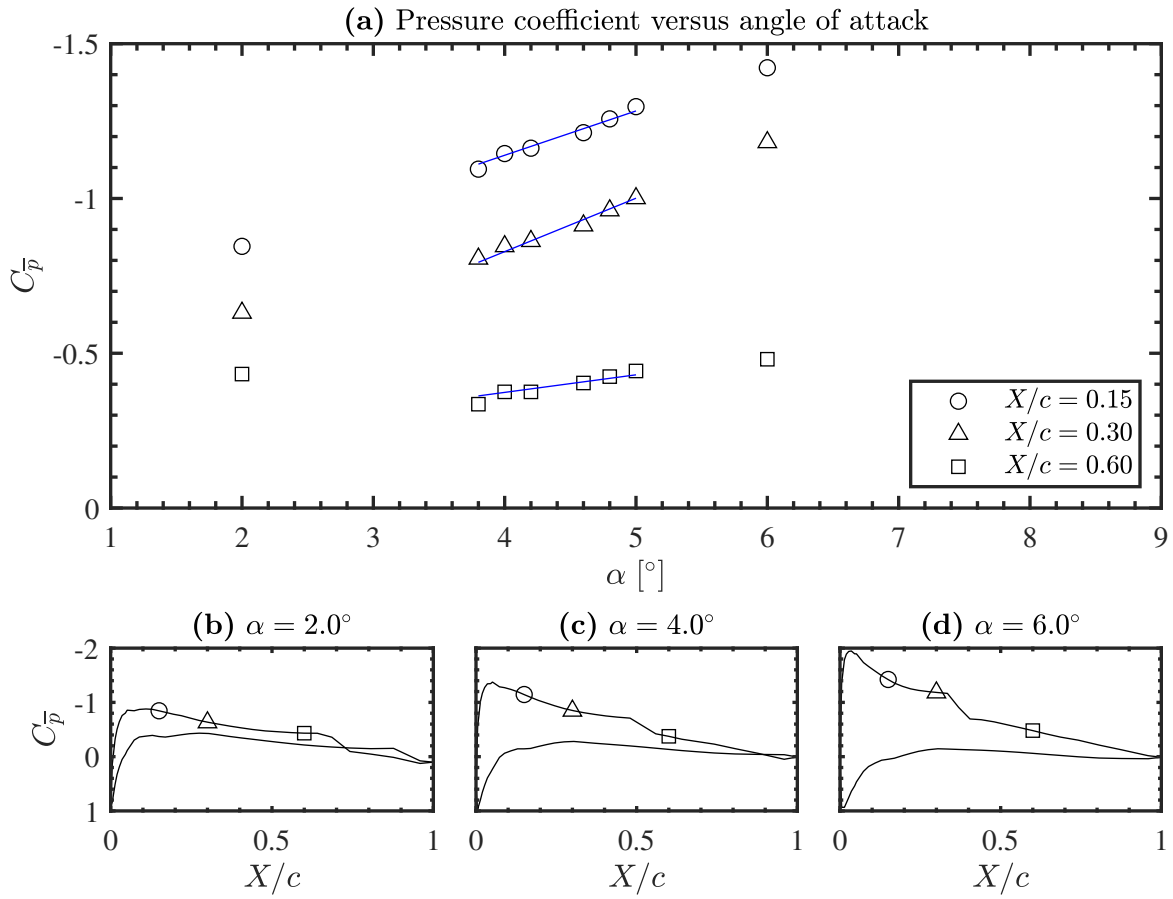

Figure 4.2: **(a)** Surface pressure coefficient versus angle of attack for the airfoil. Linear fits (in blue) are applied to the data in the range $3.8 \leq \alpha \leq 5$. **(b-d)** Representative streamwise pressure distributions.

planes are indicated by the vertical dotted lines. Since the lifting line theory has been shown to produce reasonable estimates of the effective angle of attack on the outboard region of finite wings with LSBs [22], it is employed in the present investigation to support α_{eff} estimates. In applying lifting line theory, the effective angle of attack along the span of an untwisted wing with a symmetric airfoil profile can be predicted by solving Eq. 2.5 for the coefficients A_n, which are related to the effective angle of attack at each spanwise control point i through the following relationship [3]:

$$\alpha_{eff,i} = \alpha - \sum_{n=1}^{N} n A_n \frac{\sin(n\phi_i)}{\sin(\phi_i)} \tag{4.1}$$

In applying lifting line theory, it is important to account for tunnel wall interference effects, which cause an increase in the effective angle of attack [123]. Here, because of the linear relation between α and $\alpha_{eff,i}$ and the consequent similarity of the solution for a given α, an iterative approach was used, where the value of α was iteratively changed in Eqs.

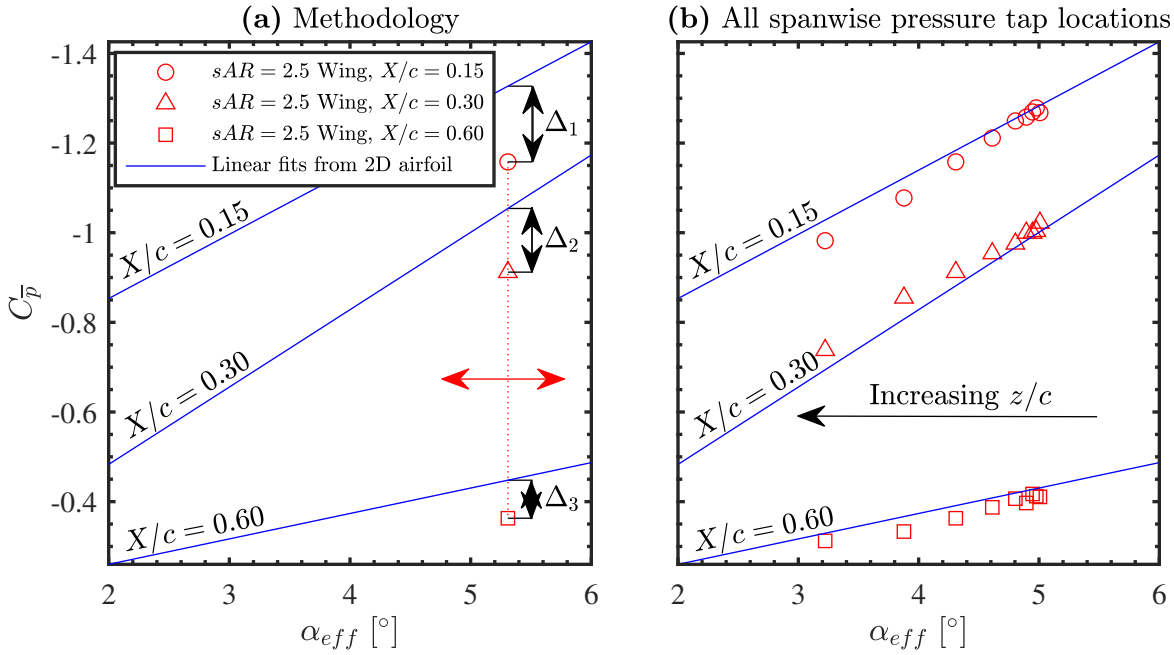

Figure 4.3: Estimation of effective angle of attack on the wing.

2.5 to obtain the best fit between the solution of Eq. 4.1 and estimates of the effective angle in Fig. 4.4. The value of α obtained was 6.6°, with the difference from the true geometric angle of attack ($\alpha = 6.0°$) verified to be in close agreement with the estimated effective angle of attack change due to wall interference [123]. A comparison of the results in Fig. 4.4, shows that the lifting line theory fit conforms well to the pressure based estimates, which lends further support to the applicability of the lifting line theory to wings operating at low Reynolds numbers and provides added confidence in the obtained distribution of the effective angles of attack. The estimates of α_{eff} at the locations of the side view 2C measurements taken from the lifting line theory curve fit in Fig. 4.4 are summarized in Table 4.1, and are used to compare measurements on the airfoil and wing in sections 4.3 and 4.4.

Table 4.1: Estimated α_{eff} at each side view 2C measurement plane.

z/c	α_{eff} [°]
0.95	4.9
1.30	4.7
1.66	4.4
2.01	3.8

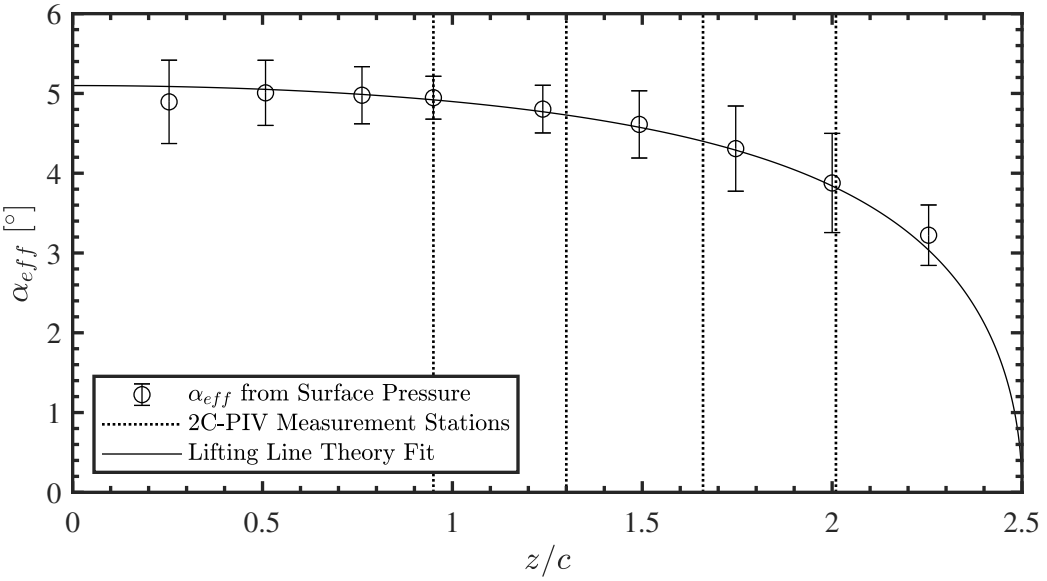

Figure 4.4: Spanwise variation of effective angle of attack on the wing. Dashed lines indicate spanwise locations of side view 2C PIV measurements. Solid line is a least-squares fit from lifting line theory for rectangular wings.

4.3 Mean Velocity Field

Mean streamwise velocity contours in the area of LSB formation are presented for the airfoil and wing in Fig. 4.5a and Fig. 4.5b, respectively, for a comparable range of effective angles of attack. The LSB is identified by the mean dividing streamline (solid black line), defined as the locus of points below which there is zero net mass flow across any wall-normal plane [7]. Separation and reattachment locations were estimated by extrapolating the dividing streamline to the model surface via a smoothing spline fit. The transition location was estimated from the location of maximum displacement thickness, which has been shown to correspond to the location of shear layer roll up and the onset of rapid pressure recovery [9, 36]. As expected from the pressure distributions (Figs. 4.2b–4.2d), as well as trends reported in previous studies on various airfoils [13, 14, 124], the LSB moves downstream and lengthens as the angle of attack is decreased on the airfoil model configuration (Fig. 4.5a). In contrast, at the four surveyed spanwise planes on the wing model (Fig. 4.5b), the LSB remains at approximately the same streamwise location across the span, while an increase in the maximum displacement thickness and wall-normal extent of reverse flow is observed with increasing z/c and decreasing α_{eff}.

For comparison, the mean locations of separation, transition, and reattachment are presented in Fig. 4.6, where they are plotted against angle of attack and effective angle of attack for the airfoil and wing, respectively. The results confirm and quantify the downstream movement of the LSB with decreasing angle of attack on the airfoil. For the wing model, over a change in effective angle of attack of 1.1°, minimal changes in the

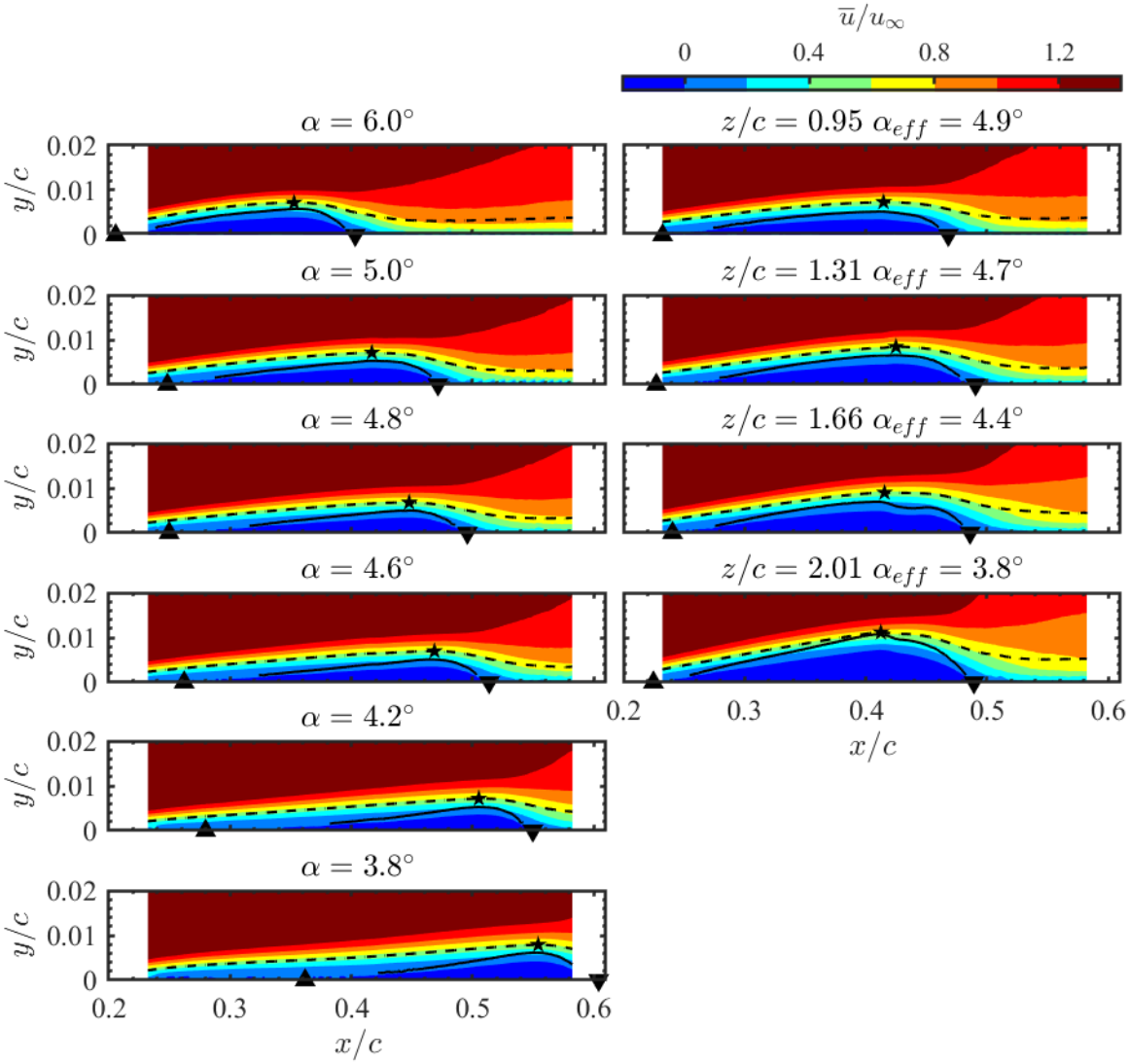

(a) Airfoil **(b)** $sAR = 2.5$ Wing

Figure 4.5: Contours of mean streamwise velocity. Solid lines: mean dividing streamline, dashed lines: displacement thickness. $\overline{x_t}$: ⋆, $\overline{x_s}$: ▲, $\overline{x_r}$: ▼.

LSB characteristics are observed, which is in stark contrast to the trends seen in the LSB characteristics on the 2D model when the angle of attack is changed by a similar amount. In fact, the spanwise variations of the mean separation, transition, and reattachment locations on the wing were verified to be comparable to the spanwise variations on the airfoil at $\alpha = 6.0°$ (see Appendix D). However, the results point to distinct similarities between the LSBs formed at equal values of α and α_{eff} for the airfoil and wing in the region away from the wingtip. In particular, at $\alpha_{eff} = 4.9°$, the measurements performed on the wing at $z/c = 0.95$ yield similar results to those obtained on the airfoil model at $\alpha = 5°$

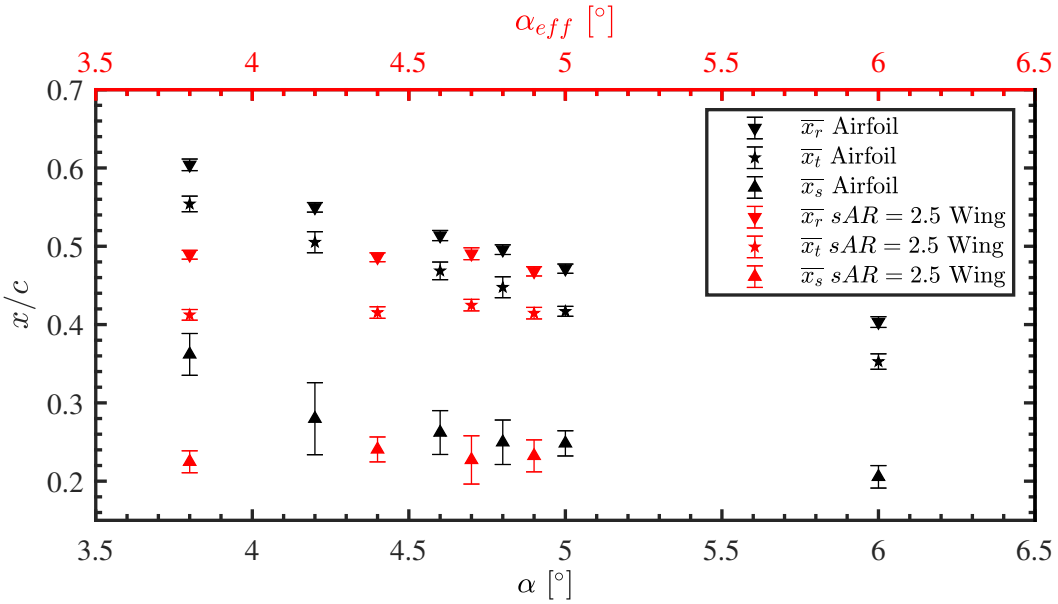

Figure 4.6: Locations of mean separation, transition, and reattachment on the airfoil at $3.8° \leq \alpha \leq 6°$ and wing at $\alpha = 6°$. Markers coloured according to the x-axis on which they are plotted.

(Fig. 4.6), as the mean streamwise velocity contours (Fig. 4.5) are remarkably similar between these cases, leading to closely matching mean LSB characteristics (Fig. 4.6). Thus, the results suggest that a quantitative similarity in mean LSB topology between the airfoil and wing is restricted to the region away from the wingtip where the flow is only weakly three-dimensional. As the spanwise gradient in the effective angle becomes progressively more significant near the wingtip, such a similarity breaks down. This important finding provides quantitative support to the results reported in Refs. [89, 91, 92], and suggests that the analogy between LSBs at the same effective angle of attack suggested by Bastedo & Mueller [23] is not universal. In fact, over the spanwise range considered in this study, the effective angle of attack of the wing root can be used to accurately describe the mean locations of separation, transition, and reattachment up to at least $z/c = 2.01$, despite the substantial reduction in α_{eff}.

In comparison to the airfoil configuration at the same effective angle of attack, the differences in LSB position on the wing are most significant near the tip (low effective angles of attack in Fig. 4.6). Here, three-dimensional effects and the spanwise pressure gradient are most significant on the wing. It should be noted that in the present analysis, the locations of separation and reattachment are based on classical estimations of the locations of zero in-plane wall shear, which can differ in strongly three-dimensional flows [71]. However, subsequent 3C PIV results presented in Chapter 5 show that the assumption of two-dimensional flow for the calculation of separation and reattachment locations does not introduce substantial error along the entire length of the LSB.

The variation in displacement thickness on the airfoil with the angle of attack is presented in Fig. 4.7a. The maximum displacement thickness does not show any significant

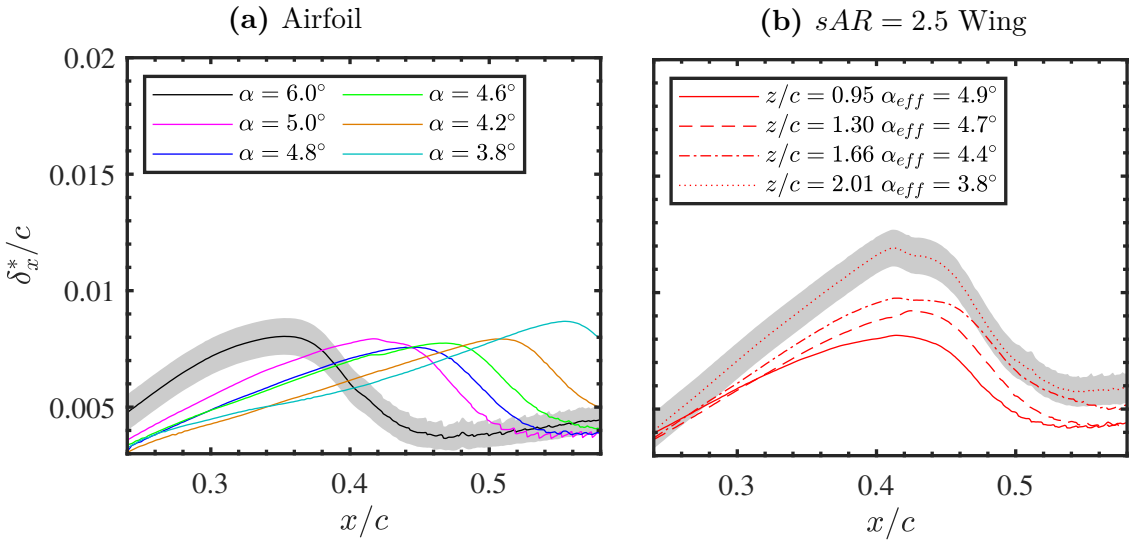

Figure 4.7: Chordwise displacement thickness. Shaded areas show typical uncertainty bounds

changes within the investigated range of airfoil incidences. On the other hand, a clear trend of increasing maximum displacement thickness with increasing z/c is observed between $0.95 \leq z/c \leq 2.01$ on the wing in Fig. 4.7b. The associated displacement of the separated shear layer away from the airfoil surface is also accompanied by an increase in the thickness of the reverse flow region, as seen in Fig. 4.5b, particularly at $z/c = 2.01$. Such changes are known to affect stability characteristics of near-wall shear flows [8, 52, 125] and even the nature of the dominant flow instability mode [54, 63]. At the same time, the characteristic mean locations of the bubble appear to remain invariant within experimental uncertainty, which points to a likely interplay between wingtip effects and changes in stability in this region. The potential implication these changes have on bubble dynamics will be explored in section 4.4.

The observed changes in maximum displacement thickness near the tip of the wing suggest that three-dimensional effects are important to LSB development in the vicinity of the wingtip, where a considerable spanwise pressure gradient is observed (Fig. 4.1b). Using the top view PIV configuration (Fig. 3.4b), measurements of streamwise and spanwise flow were made above a portion of the airfoil and wing surfaces at $\alpha = 6.0°$, with time averaged flow fields presented in Fig. 4.8. This figure shows sectional streamlines superimposed onto contours of mean spanwise flow velocity. The results verify two-dimensional flow for the airfoil, and confirm the presence of a crossflow that progressively increases in magnitude near the wingtip. The isolation of significant spanwise flow to $2.2 \leq z/c$ agrees with the findings of Bastedo & Mueller [23], who observed that the three-dimensional flow region is limited to a distance of less than $0.4c$ from the wingtip at moderate angles of attack. Although the mean spanwise velocity magnitude on the wing remains below 7% of u_∞ (Fig. 4.8b) at the outermost side view 2C measurement plane ($z/c = 2.01$), the top view measurement plane is located at a minimum of $0.007c$ from the wing surface. The

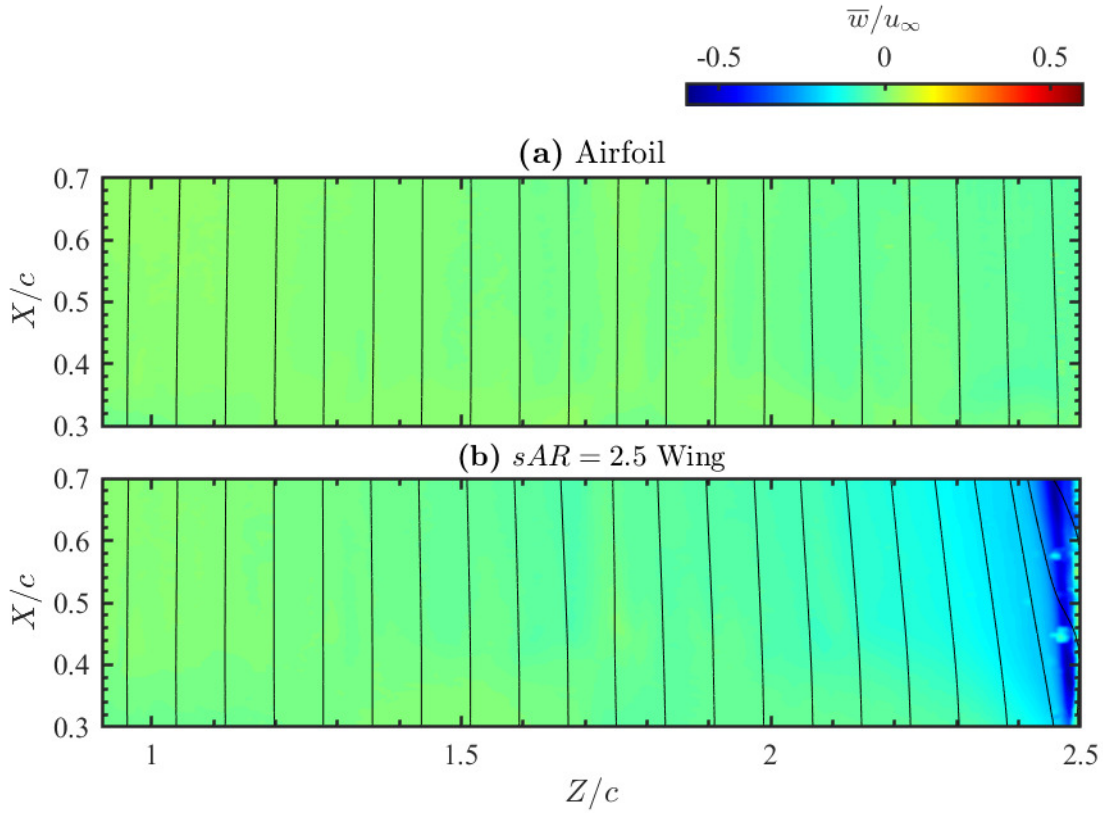

Figure 4.8: Mean spanwise velocity contours and sectional streamlines. $\alpha = 6°$

pronounced changes in mean LSB structure at this location are suspected to be the result of higher spanwise velocities closer to the wing surface. This is because a spanwise pressure gradient causes the lower velocity fluid located nearer to the surface to turn more sharply, since the centrifugal and pressure forces must balance in the cross-stream direction [126]. Therefore, the spanwise velocities seen in Fig. 4.8 are not necessarily representative of the spanwise velocities throughout the entire boundary layer thickness.

4.4 Separation Bubble Dynamics

Vortex shedding in the LSB is examined in Figs. 4.9 and 4.10, where sequences of instantaneous spanwise vorticity are presented for the airfoil and wing configurations, respectively. On the airfoil (Fig. 4.9), the formation and shedding of shear layer vortices can be clearly seen in Fig. 4.9a, corresponding to $\alpha = 5.0°$. The shear layer rolls up at approximately the location of maximum mean bubble height ($x/c = 0.40$) and the shed vortices propagate downstream, marked by dashed lines connecting the same structures in the sequence. A similar dynamics is captured on the wing at a similar effective angle of attack (Fig. 4.10a), with comparable roll-up location and streamwise wavelength of the structures observed for this spanwise location, which is subject to a minimal level spanwise flow (Fig. 4.8). As

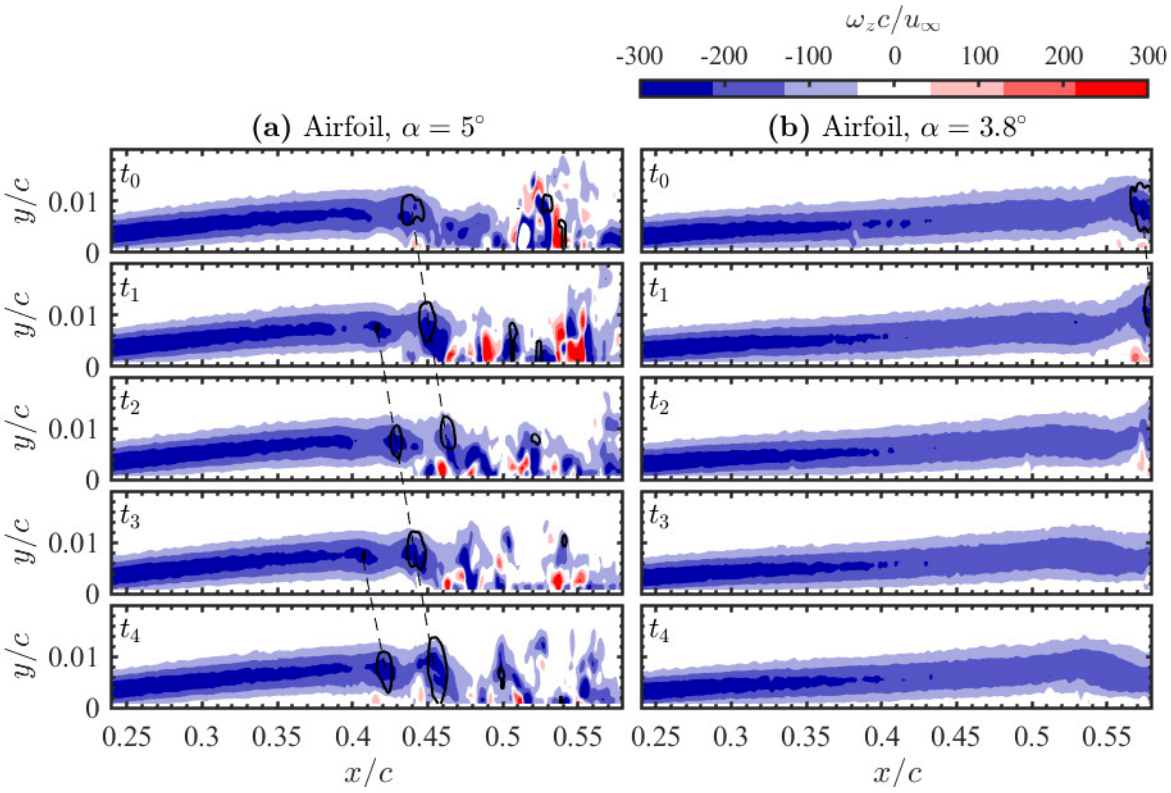

Figure 4.9: Contours of instantaneous spanwise vorticity on the airfoil. Solid lines are contours of λ_2 criterion [127]. Frame separation is 0.13 ms. Dashed lines track individual vortices.

expected from the time-averaged results discussed earlier, decreasing the angle of attack of the airfoil results in the downstream movement of the roll-up location, which can be seed from a comparison of Figs. 4.9a and 4.9b. In contrast, for the wing configuration, the roll-up location remains largely insensitive to the decrease in the effective angle of attack (Fig. 4.10). However, the increase in maximum displacement thickness at $z/c = 2.01$ is associated with the formation of roll-up vortices farther from the wing surface compared to those at $z/c = 0.95$.

The RMS fluctuating velocity fields for the airfoil and wing are shown in Figs. 4.11 and 4.12, respectively. Both cases show a significant increase in the amplitude of the fluctuations in the aft portion of the separation bubble. The rapid growth in the magnitude of u'_{RMS} and v'_{RMS} is most prominent near the location of mean transition, coincidental with shear layer roll-up seen in Figs. 4.11 and 4.12. At a fixed x/c location in the vicinity of $\overline{x_t}$, three peaks are seen in the u'_{RMS} fields for both airfoil and wing configurations, which is in agreement with previous experimental studies [56, 128] and eigenmodes obtained in linear stability calculations [9, 35]. The most significant fluctuations in the streamwise velocity component (Fig. 4.11) closely follow the boundary layer displacement thickness (marked by the dashed line), outlining the trajectory of convectively amplified perturbations in the separated shear layer. The elevated streamwise velocity fluctuations along the displacement thickness in

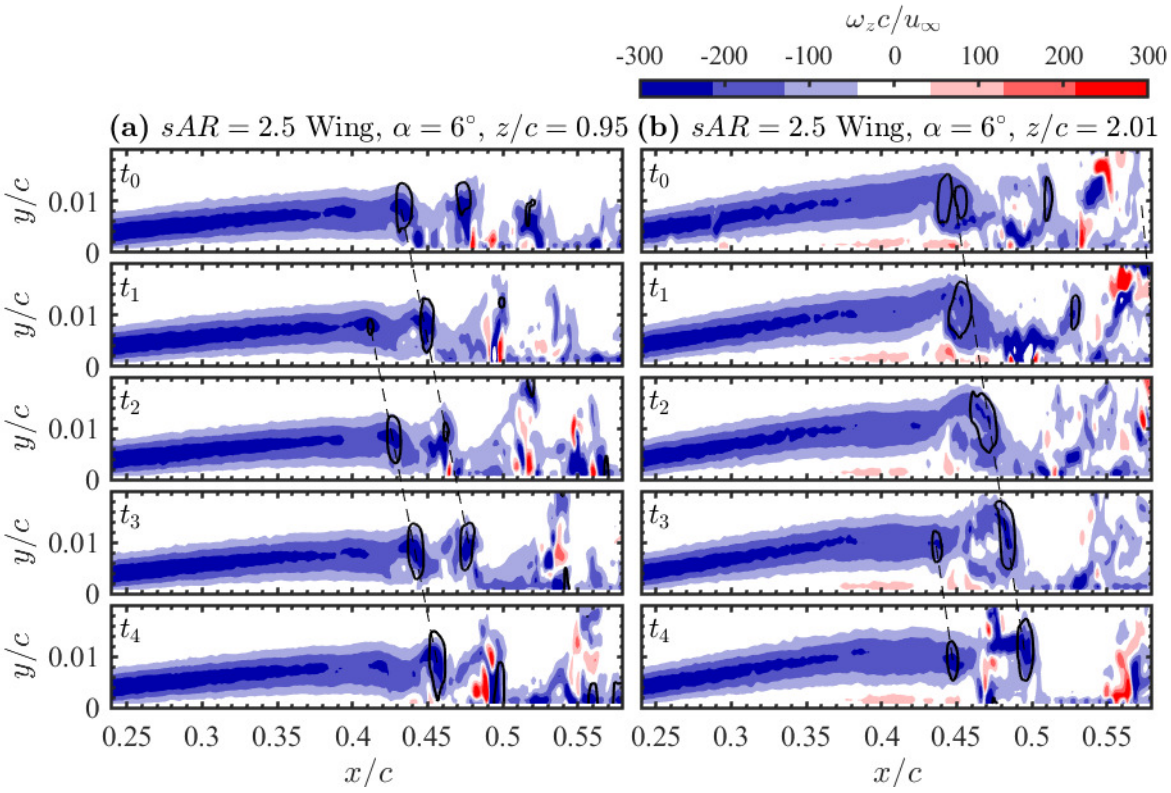

Figure 4.10: Contours of instantaneous spanwise vorticity on the wing. Solid lines are contours of λ_2 criterion [127]. Frame separation is 0.13 ms. Dashed lines track individual vortices.

the upstream portion of the bubble are associated with low frequency oscillations of the shear layer, known as bubble flapping [124, 129]. For the wall-normal velocity fluctuations (Fig. 4.12), the maximum is reached at approximately the mean reattachment location, where vortices are shed into the redeveloping turbulent boundary layer. For the airfoil, the location of the onset of significant velocity fluctuations moves downstream with decreasing angle of attack, following the downstream movement of the mean transition and the mean reattachment locations. For the wing, consistent with the location of mean transition remaining relatively constant across the span, the RMS velocity contours indicate that the location of rapid growth of turbulent fluctuations remains largely unchanged as the effective angle of attack changes from 4.9° to 3.8°. Although the RMS velocity contours on the wing closely resemble those obtained on the airfoil at $\alpha = 5.0°$, the vertical extent of the region associated with the highest contours of u'_{RMS} and v'_{RMS} is larger on the wing, and increases towards the wingtip. This correlates with the increase in the displacement thickness (Fig. 4.7b), which is expected to result in a more unstable shear layer (i.e., higher amplifications factors [8, 125]).

Spectral analysis of velocity fluctuations measured in the separated shear layer is performed to explore potential differences in the frequency content and amplitude of the amplified disturbances between the airfoil and wing configurations. Figure 4.13 presents

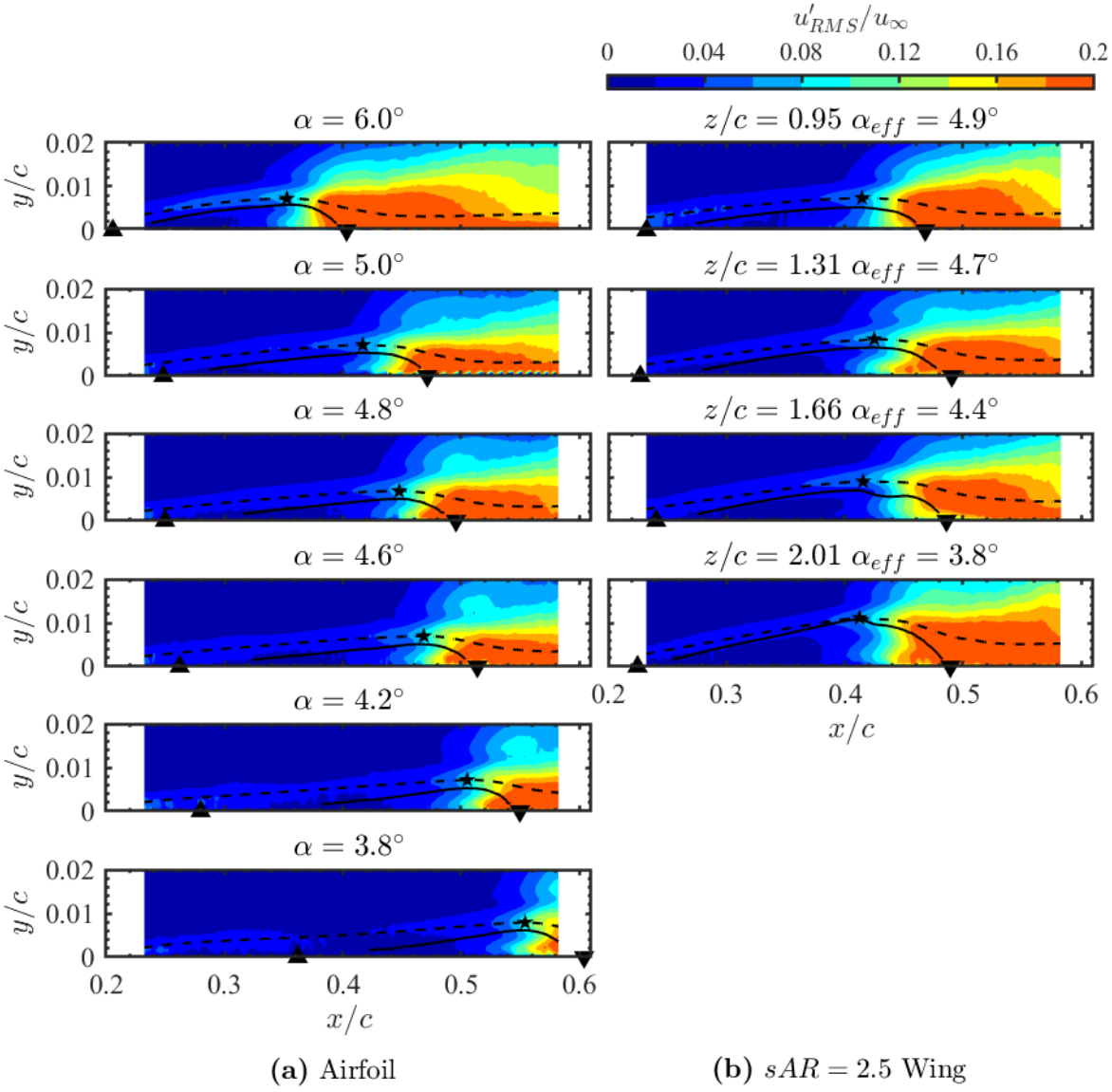

(a) Airfoil **(b)** $sAR = 2.5$ Wing

Figure 4.11: Contours of RMS streamwise velocity fluctuations. Solid lines: mean dividing streamline, dashed lines: displacement thickness. $\overline{x_t}$: ⋆, $\overline{x_s}$: ▲, $\overline{x_r}$: ▼.

spectra of wall-normal velocity fluctuations at $y = \delta^*$ for the airfoil at three angles of attack, with frequency presented in terms of the Strouhal number. The results show the amplification of disturbances within a band of frequencies, with the central instability frequency of the band marked by a dashed line. As the angle of attack of the airfoil decreases from $\alpha = 5.0°$ to $\alpha = 3.8°$, the onset of disturbance amplification occurs farther downstream (c.f. spectra at $x/c = 0.41$ for Figs. 4.13a-4.13c), and the central instability frequency decreases from $St_0 = 15.9$, to $St_0 = 13.4$, in agreement with the trends reported in previous studies [11, 14]. In contrast, the spectra of wall-normal velocity fluctuations

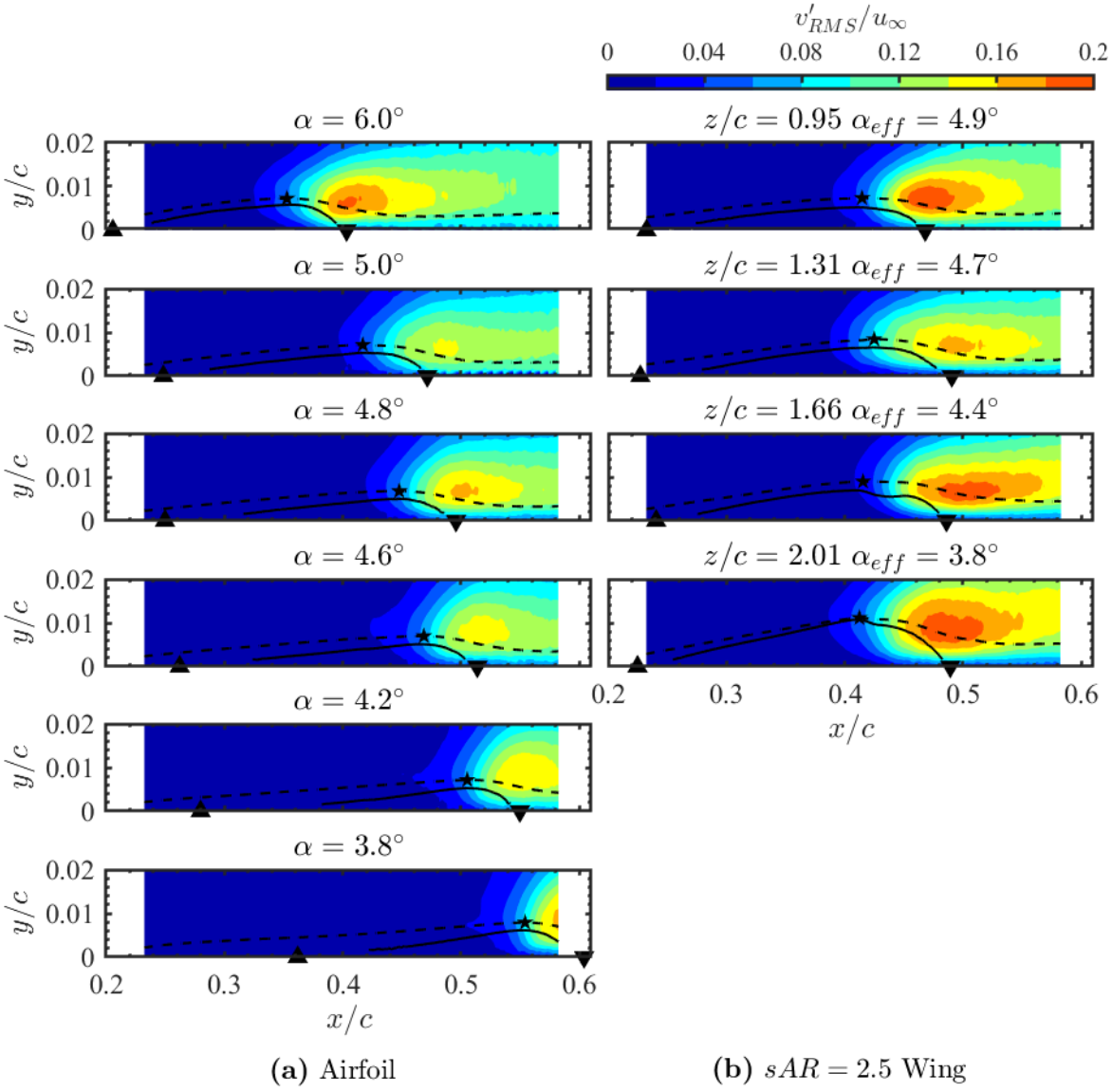

(a) Airfoil **(b)** $sAR = 2.5$ Wing

Figure 4.12: Contours of RMS wall-normal velocity fluctuations. Solid lines: mean dividing streamline, dashed lines: displacement thickness. $\overline{x_t}$: $\star$, $\overline{x_s}$: ▲, $\overline{x_r}$: ▼.

in the separated shear layer of the wing (Fig. 4.14) do not show a marked change in the central instability frequency with decreasing effective angle of attack, nor the accompanying delay in the amplification of the perturbations.

Figure 4.15 facilitates a more detailed comparison of wall-normal velocity fluctuation spectra obtained at the same streamwise positions in the separated shear layer at different spanwise locations on the wing at $\alpha = 6°$ and on the airfoil at $\alpha = 5.0°$. All spectra presented in Fig. 4.15 were taken at $\overline{x_t}$ and $y = \delta^*$. The bands of amplified frequencies at spanwise locations of $z/c \leq 1.30$ from the wing are similar to that seen for the two-dimensional

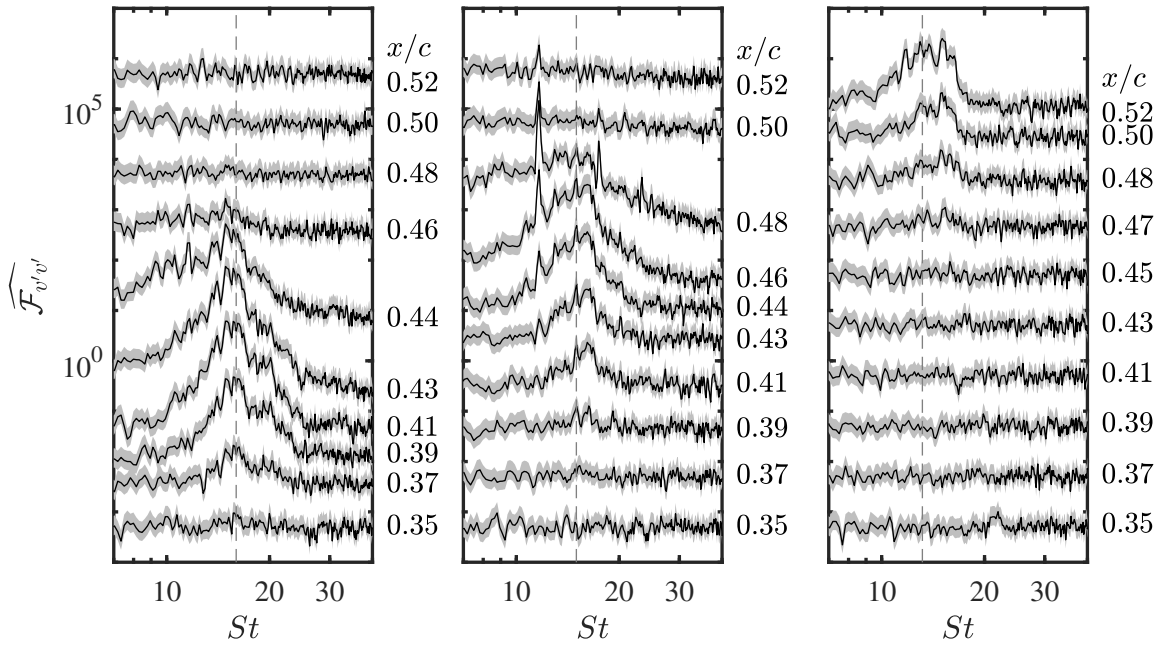

(a) $\alpha = 5.0°$ **(b)** $\alpha = 4.6°$ **(c)** $\alpha = 3.8°$

Figure 4.13: Spectra of wall-normal velocity fluctuations at $y = \delta^*$ on the airfoil. Each spectrum has been normalized by its total energy content and each x/c location has been stepped by an order of magnitude for clarity. Dashed lines indicate St_0. Shaded regions indicate the uncertainty in power spectral density magnitude.

airfoil at $\alpha = 5.0°$, which is expected from the relatively small change in the effective angles of attack from 4.9° to 4.7°. Near the wingtip ($z/c = 2.01$), despite the decrease in effective angle of attack to $\alpha_{eff} = 3.8°$, the most amplified frequency does not shift to lower frequencies. However, a slightly wider band of amplified frequencies is observed. This is attributed to the increased height of the separation bubble at this location, which is expected to lead to a broadening of the unstable frequency range as the inflection point of the separated shear layer moves away from the wall [52].

Figure 4.16 shows the central instability frequency plotted for the airfoil and wing, as a function of angle of attack and effective angle of attack, respectively. The results for the airfoil show a nearly linear increase in St_0 with increasing angle of attack, closely following the trends seen in the results taken from previous studies of the same airfoil over a similar range of Reynolds numbers [14]. For the wing at $z/c = 0.95$, where $\alpha_{eff} = 4.9°$, the central instability frequency closely matches the central instability frequency of the airfoil at $\alpha = 5.0$. As the effective angle of attack decreases towards the wingtip, the central instability frequency on the wing remains within the range $16.1 \leq St_0 \leq 17.8$ over the spanwise extent of side view 2C measurements. This variation of the central instability frequency along the span of the wing is largely captured by the experimental uncertainty and was verified to be comparable to the spanwise variation on the airfoil at the same geometric angle of attack.

The top view PIV measurements provide further insight into the spanwise structure of the shear layer roll-up process, with representative instantaneous measurements conducted at an angle of attack of $\alpha = 6.0°$ for both models presented in Fig. 4.17. Note that the sampling rate of the top view measurements is orders of magnitude lower than the relevant time-scales of the vortex shedding process, producing measurements of uncorrelated velocity fields. Because the light sheet for the top view measurements was positioned to intersect the top halves of the shear layer roll-up vortices, the dominant spanwise rollers appear as bands of high streamwise velocity. In agreement with the side view 2C measurements, the roll-up vortices on the wing (Fig. 4.17b) form further downstream in comparison to the airfoil (Fig. 4.17a), which is attributed to the lower effective angle of attack. For comparison, the mean locations of separation (solid lines), transition (dashed lines), and reattachment (dotted lines) obtained from side-view measurements are shown in Fig. 4.17. The results reveal a strongly two-dimensional initial vortex formation process on the airfoil, in agreement with previous studies on LSBs at low levels of free-stream turbulence [56, 57, 130]. Previous investigators have attributed this to the LSB transition being driven by a Kelvin-Helmholtz instability, leading to the preferential amplification of two-dimensional modes [8, 55, 131]. However, shortly downstream, notable spanwise undulations develop in the spanwise vortex filaments, and three-dimensional breakdown to turbulence occurs downstream of the mean reattachment location, which is evidenced by the appearance of numerous low velocity patches across the span (Fig. 4.17a). For the wing, a strikingly similar degree of spanwise uniformity is observed in the shear layer roll-up vortices (Fig. 4.17b), along with a similar three-dimensional breakdown to turbulence that occurs downstream of mean reattachment. Furthermore, the roll-up vortices on the wing in the range $0.95 \leq z/c \leq 2.01$ are not appreciably deformed, indicating that the reduction in local effective angle of attack has little effect on the vortex topology in this region. Incorporating the results of spectral analysis, it can be concluded that spanwise variations in LSB dynamics on a finite wing are not predicated on the local changes of the effective angle of attack. Instead, salient vortex shedding characteristics do not change appreciably over the span of the wing, and are well approximated by those seen on a two-dimensional airfoil at the same angle of attack as the effective angle of the wing root. It is important to note, however, that more pronounced variations in LSB characteristics may take place in the immediate vicinity of the wingtip.

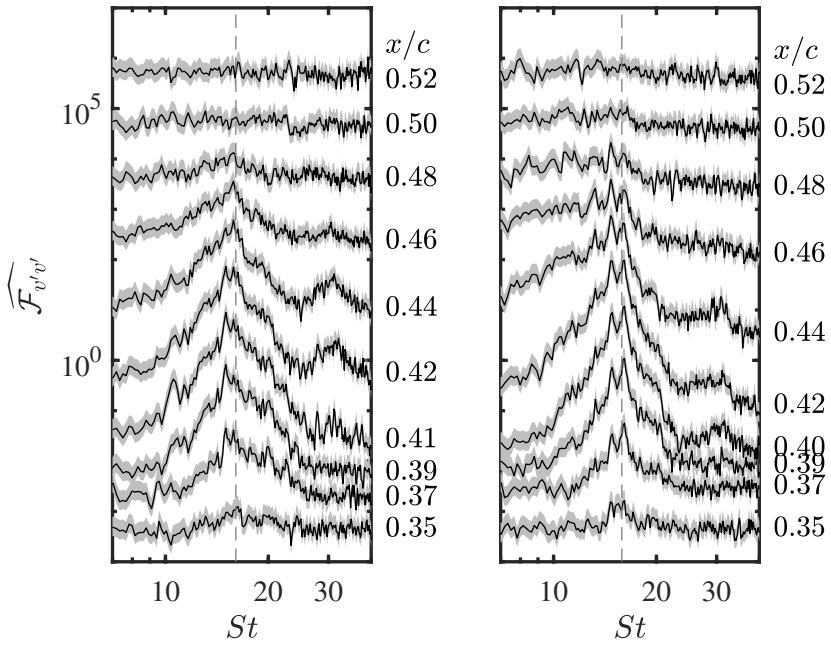

(a) $z/c = 0.95$
$\alpha_{eff} = 4.9°$

(b) $z/c = 1.30$
$\alpha_{eff} = 4.7°$

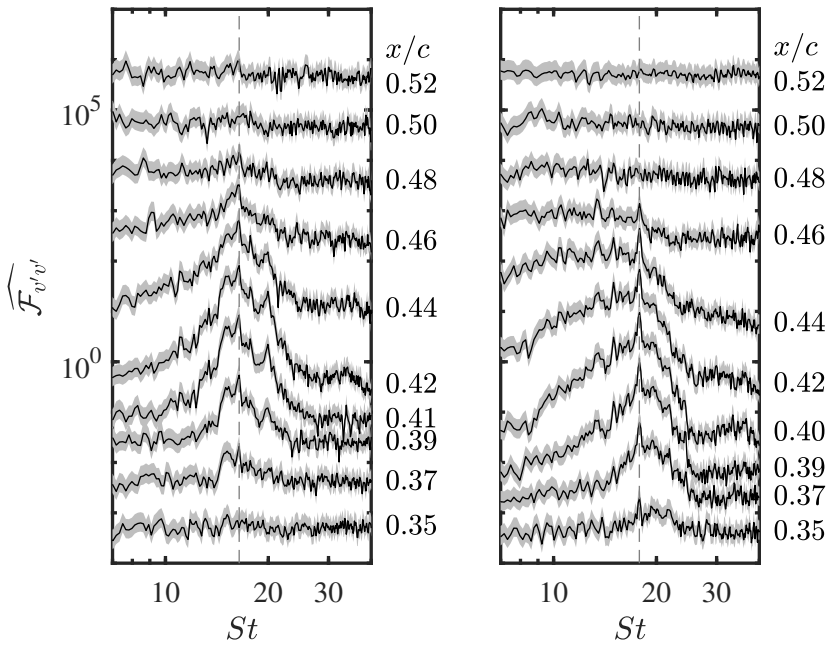

(c) $z/c = 1.66$
$\alpha_{eff} = 4.4°$

(d) $z/c = 2.01$
$\alpha_{eff} = 3.8°$

Figure 4.14: Spectra of wall-normal velocity fluctuations at $y = \delta^*$ on the wing at $\alpha = 6°$. Each spectrum has been normalized by its total energy content and each x/c location has been stepped by an order of magnitude for clarity. Dashed lines indicate St_0. Shaded regions indicate the uncertainty in power spectral density magnitude.

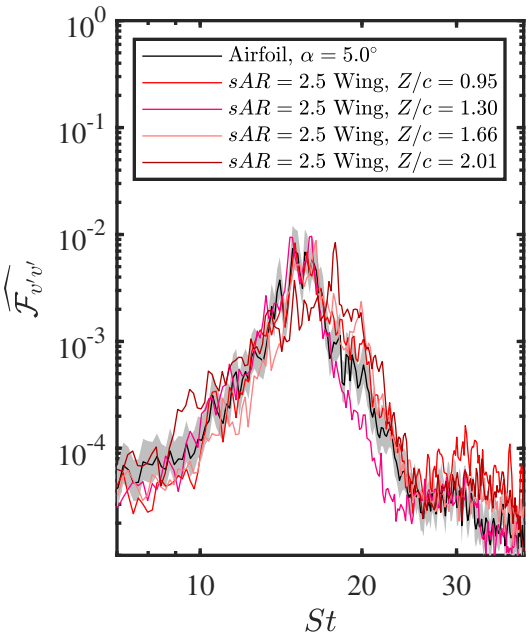

Figure 4.15: Wall-normal fluctuating velocity spectra evaluated at $y = \delta^*$ and $\overline{x_t}$ on the wing at $\alpha = 6°$ (red) and airfoil at $\alpha = 5°$ (black). Each spectrum has been normalized by its total energy content. Shaded region indicates the uncertainty in power spectral density magnitude for the airfoil at $\alpha = 5°$.

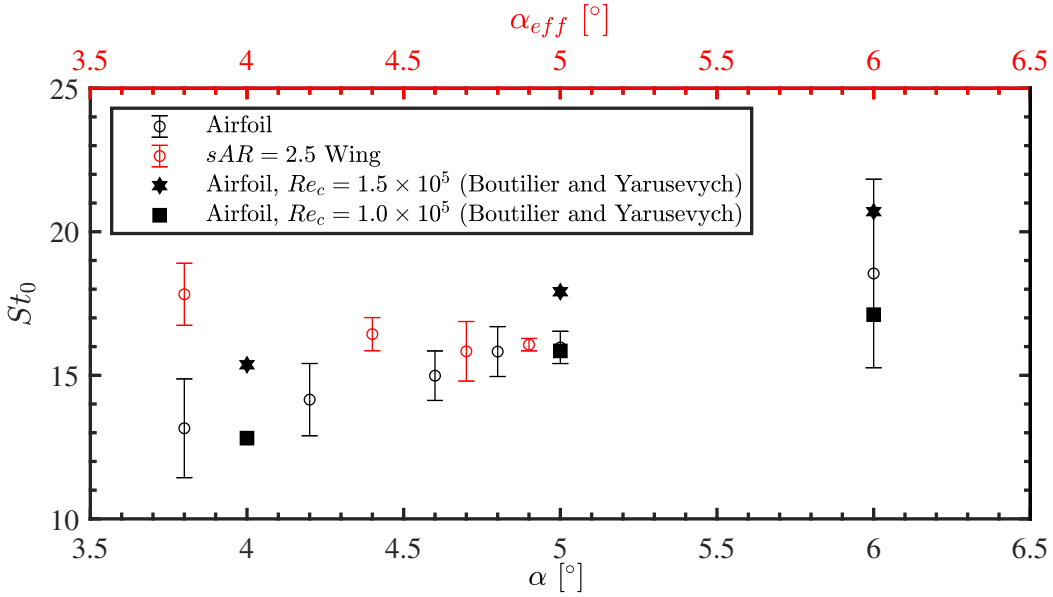

Figure 4.16: Central frequency of amplified disturbances for the airfoil and wing at $3.8° \leq \alpha \leq 6.0°$ and $\alpha = 6.0°$ respectively. Data at $Re_c = 1.0 \times 10^5$ and 1.5×10^5 from Boutilier & Yarusevych [14].

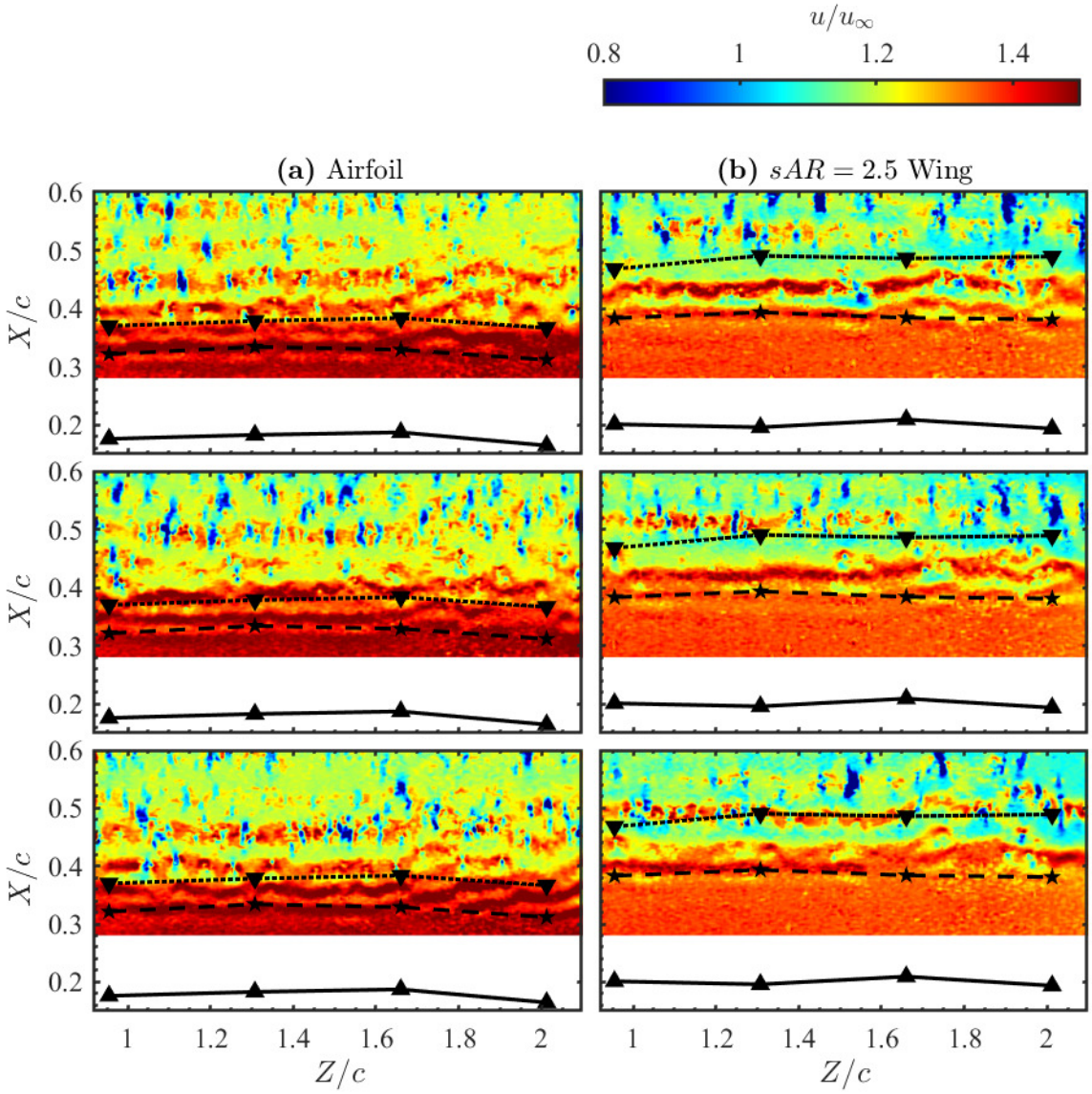

Figure 4.17: Instantaneous streamwise velocity contours from top view PIV. $\alpha = 6°$. Solid, dashed, and dotted lines are linear fits to $\overline{x_s}$, $\overline{x_t}$, and $\overline{x_r}$, respectively.

Chapter 5

Structure and Dynamics of a Three-Dimensional Laminar Separation Bubble

The results of Chapter 4 establish that LSBs on finite wings are influenced by the three-dimensional flow produced at the wingtip. Although the investigation was limited to the portion of the wing where measured spanwise velocities were low and vortex shedding proceeded in a spanwise-uniform fashion, spanwise variations were still observed in the LSB on the wing. Notably, the LSB on the wing became substantially thicker with increasing z/c. However, the reason for this change was not apparent from the 2C PIV measurements. To investigate the structure and dynamics of the interaction between the LSB and the spanwise pressure gradient on the wing, 3C PIV measurements were performed to obtain a detailed three-dimensional account of the outboard portion of the LSB, from $z/c = 1.25$ to $z/c = 2.45$. The objective of these measurements was to provide an explanation for the spanwise variations seen in the LSB in Chapter 4, and to determine how the classical LSB topology (Fig. 2.1) changes near the wingtip. The results of this chapter pertain to the LSB forming on the suction surface of a rectangular NACA 0018 semispan wing at an angle of attack of 6° and a chord Reynolds number of $Re_c = 1.25 \times 10^5$. In this configuration, 3C PIV is used to inform a three-dimensional description of the time mean structure and transition dynamics of the tip region of the LSB. The evolution of the LSB in the spanwise direction is presented from the region of nominally two-dimensional flow at the midspan, to the wingtip where the LSB terminates under the influence of the wingtip vortex.

5.1 Time Average Flow

Figure 5.1 highlights the spanwise changes in the mean velocity field towards the wingtip based on a representative subset of side view 3C measurement planes. From $z/c = 1.25$ to $z/c = 2.05$, the streamwise velocity contours in Fig. 5.1a show no substantial changes in the streamwise extent of the reverse flow region. Within this spanwise region, the LSB position and length are in close agreement with those on the two-dimensional airfoil at the effective angle of attack, as detailed in Chapter 4. At $z/c = 2.15$, the LSB moves downstream, and the reverse flow region can be seen to extend beyond the maximum downstream extent of the field of view. Closer to the wingtip, at $z/c = 2.25$, the full streamwise extent of the reverse flow region is again captured within the field of view, and its length and height diminish notably. Eventually, at and beyond $z/c = 2.35$, no reverse flow is detected. This is accompanied by a notable decrease in boundary layer thickness, which is due to a significant downwash induced by the wingtip vortex evidenced by the negative wall-normal component of mean velocity in Fig. 5.1b at $z/c = 2.45$.

The spanwise velocity contours in Fig. 5.1c reveal the presence of substantial spanwise flow in the LSB, reflecting the increased three-dimensionality of the flowfield near the wingtip. As expected for a finite wing, the spanwise flow over the suction surface occurs in the negative z direction towards the wing root. Notably, the recirculation region of the LSB near the wingtip contains substantially higher spanwise velocities than the surrounding flow, indicating that the recirculation region is influenced by the spanwise pressure gradient. At $z/c = 1.25$, where the LSB on the wing is similar to that on the two-dimensional airfoil at the same effective angle of attack, the magnitude of spanwise flow does not exceed $0.1u_\infty$. However, over the range $1.95 < z/c < 2.15$ the magnitude of spanwise velocities in the reverse flow region exceed $0.3u_\infty$. The increased strength of the spanwise flow on this part of the span coincides with major spanwise changes in the length and height of the reverse flow region visible in Fig. 5.1a. At $z/c = 2.45$, substantial spanwise flow in the negative z direction occurs across the entire field of view because of the proximity of the wingtip vortex core.

Figures 5.2a and 5.2b present limiting streamlines on the two-dimensional airfoil and wing, respectively. Limiting streamlines were calculated from the velocity gradient at the boundary using a third order polynomial fit to the ten velocity vectors nearest to the surface at each (x, z) location. Note that due to the higher effective angle of attack of the two-dimensional airfoil, the LSB is located farther upstream in comparison to the finite wing at the same geometric angle of attack. Although the separation line is located just outside of the field of view for the two-dimensional configuration, the results show a strongly uniform mean reattachment and nearly two-dimensional limiting streamlines (Fig. 5.2a). This is in agreement with spanwise surface pressure measurements, which show spanwise variations below 6% of the spanwise average in the reverse flow region ($X/c = 0.3$, Fig. 4.1b).

On the wing (Fig. 5.2b), the separation and reattachment lines have been heuristically identified as the attractor and repellor of nearby limiting streamlines in the separation and reattachment regions, respectively. Because the separation line of the LSB on the wing does

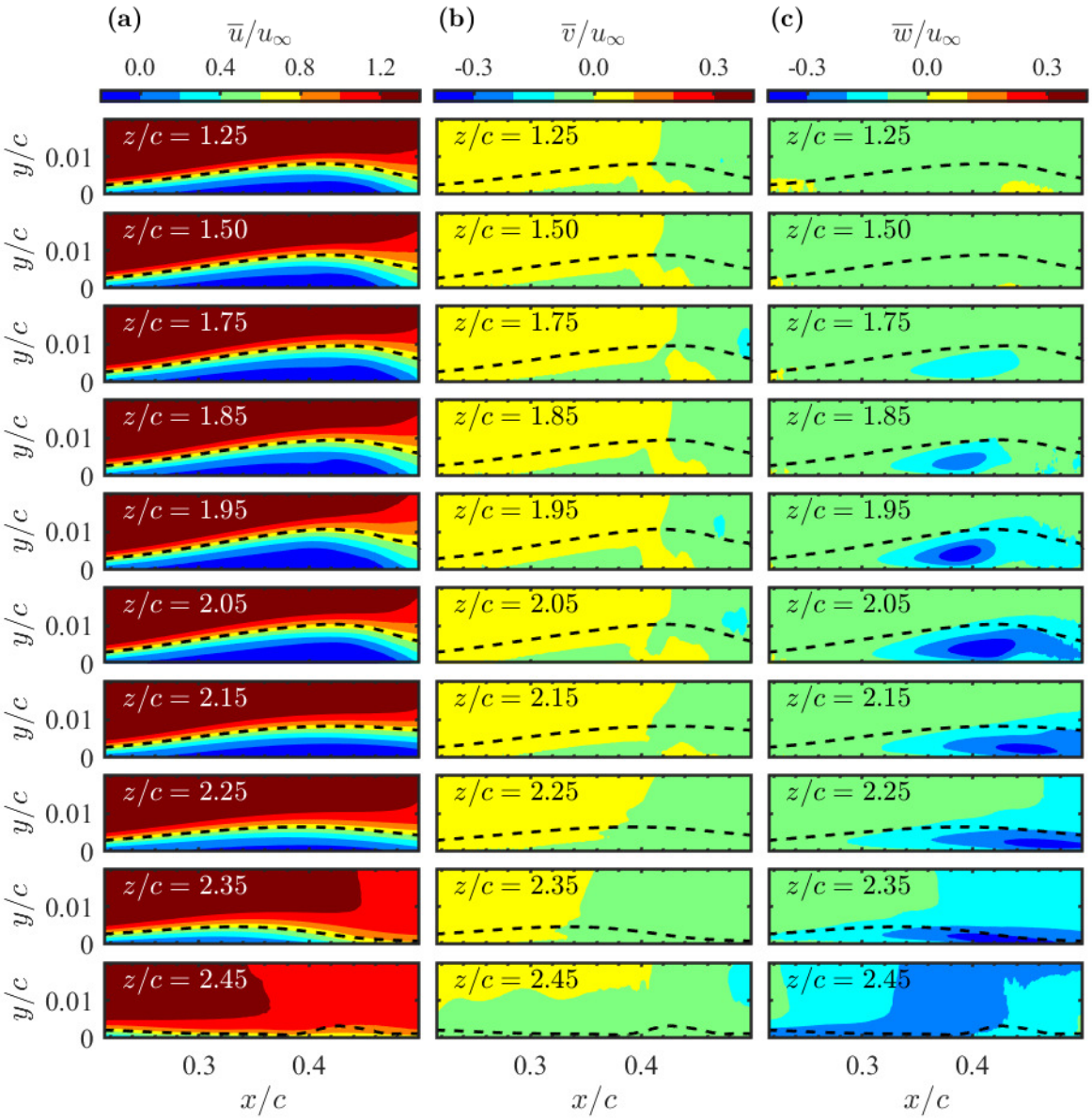

Figure 5.1: Mean velocity contours of the suction surface LSB from selected side view 3C measurement planes on the wing. Dashed line: streamwise displacement thickness.

not emanate from a saddle point, it is classified as a crossflow separation [66, 70]. Similar to the results of numerical simulations of crossflow separation on an ogive cylinder by Yates & Chapman [72], a well-defined onset of separation cannot be identified at the outboard end of the LSB ($2.10 \leq z/c \leq 2.35$, Fig. 5.2b), where the streamlines gradually approach a common envelope.

The limiting streamlines on the wing in Fig. 5.2b reveal that the near-surface flow is largely spanwise uniform in the inboard region ($1.25 \leq z/c \leq 1.85$), despite a notable spanwise flow component within the LSB. As the wingtip is approached, the separation

line remains at a nearly consistent x/c location before curving upstream at $z/c \approx 2.30$, whereas the reattachment line moves downstream and exits the field of view. The limiting streamlines within the LSB display a progressively increasing spanwise orientation with increasing z/c, consistent with the spanwise flow observed in Fig. 5.1c, suggesting that fluid enters into the LSB at its outboard end. For $z/c > 2.25$, the limiting streamlines reorient into the positive streamwise direction due to the influence of the wingtip vortex, which suppresses boundary layer separation, e.g., [29, 132].

The overall limiting streamline field displays a strong similarity to the qualitative flow visualisations by Huang & Lin [91],Yen & Huang [133], and Ananda *et al.* [134] of LSBs on finite wings. A downstream shift in LSB reattachment lines near the tips of finite wings was also reported from the flow visualisations of Marchman & Abtahi [89], Bastedo & Mueller [23], and Genç *et al.* [93]. It is important to note that this behaviour, expected from the reduction in the effective angle of attack [23], is constrained to the relative vicinity of the wingtip ($z/c > 2.15$, Fig. 5.2b). For comparison, within $1.25 \leq z/c \leq 2.15$ where the effective angle of attack changes from about 5° to 3° (Fig. 4.4), an LSB on a two-dimensional wing would move downstream by about $0.15c$ [14], i.e., about 75% of the present bubble length. Thus, the spanwise variations seen in the LSB extent and position over the majority of the span are significantly lower than those expected from the changes in the effective angle of attack, and the bubble appears to settle on a configuration driven by the effective angle at the wing root, except in the proximity of the wingtip.

Figure 5.2b also reveals a distinct change in direction of the limiting streamlines at approximately $x/c = 0.40$, which roughly demarcates the fore and aft portions of the LSB (i.e., the dead air region and mean reverse flow vortex, respectively, Fig. 2.1). The limiting streamlines in the forward part of the bubble are directed more strongly in the spanwise direction, similar to the numerical simulations of Chen *et al.* [92]. Because the skin friction within the LSB has a negative z component, the streamwise gradient in the spanwise flow magnitude implies that the recirculating flow within the LSB follows a helical path which is similar to LSBs on nominally infinite swept wings [7].

Although the limiting streamline field is in qualitative agreement with previous surface flow visualisations on finite wings at low Reynolds number, resolving the attendant three-dimensional flowfield is essential to reconstruct the bubble topology and understand the mechanisms by which the observed surface patterns form. Figure 5.3 presents isosurfaces of zero streamwise velocity ($\overline{u} = 0$) and vorticity magnitude ($\overline{|\omega|}c/u_\infty = 175$) constructed from the side view 3C measurements that illustrate the three-dimensional structure of the LSB on the wing. The results show that the streamwise bounds of the reverse flow region closely follow the separation and reattachment lines determined from the limiting streamline topology. At the outboard end of the LSB, the reverse flow region thickness reduces, and no reverse flow is eventually detected for $z/c > 2.30$. The isosurface of vorticity magnitude in Fig. 5.3b reveals the three-dimensional structure of the separated shear layer. The vorticity level of $\overline{|\omega|}c/u_\infty = 175$ was chosen to capture the shear layer core trajectory. Away from the wingtip, the vorticity isosurface shows strong spanwise uniformity, following the expected gradual departure of the shear layer from the wall in the fore portion of the bubble. A notable discontinuity occurs at $z/c \approx 2.30$ (Fig. 5.3b), where reverse flow is no longer

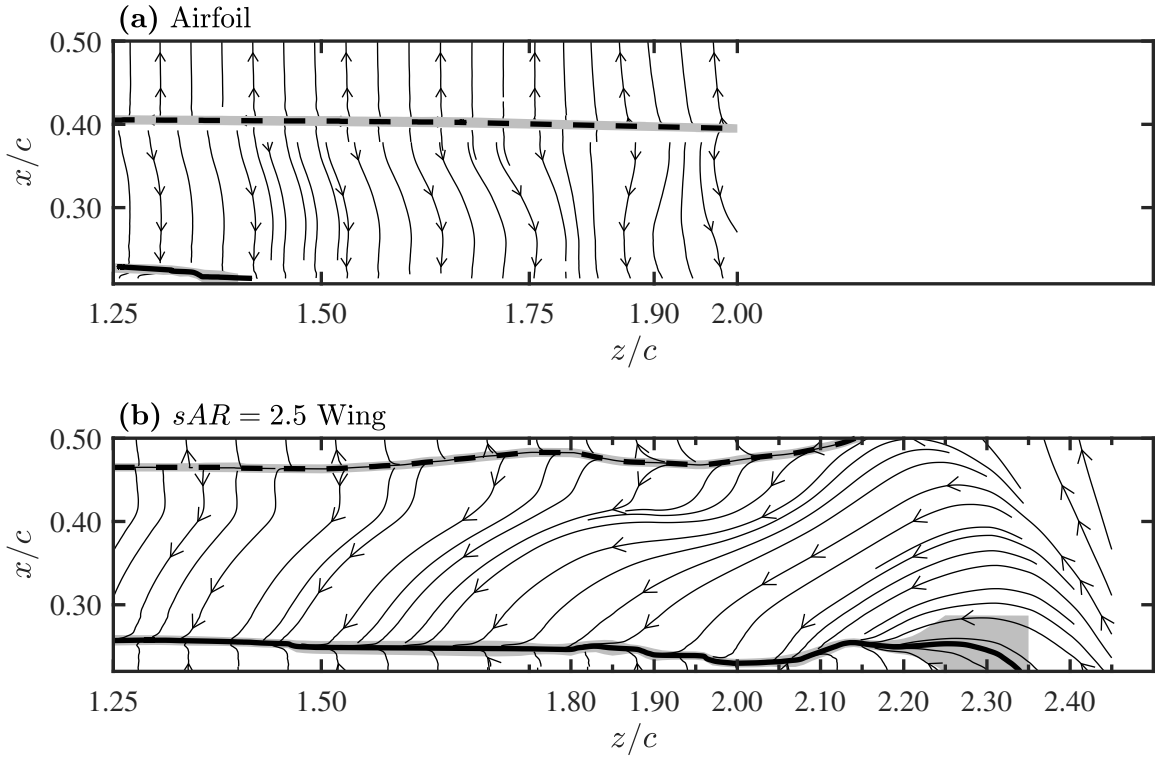

Figure 5.2: Limiting streamlines. Thick solid and dashed lines: mean separation and reattachment lines, respectively. Vertical tick marks indicate spanwise locations of side view 3C measurement planes. Shaded regions indicate uncertainty in separation and reattachment line estimates.

observed (Fig. 5.3a). Beyond this spanwise location, downwash from the wingtip vortex causes the boundary layer and its bound vorticity to remain attached to the wing surface.

A more quantitative analysis of the changes in the wall-normal and streamwise extent of the LSB along the span is facilitated by Fig. 5.4a and Fig. 5.4b, respectively. The spanwise variation of maximum thickness of the $\overline{u} = 0$ isosurface is presented in Fig. 5.4a, along with the maximum streamwise displacement thickness. The latter was confirmed to closely follow the maximum height of the inflection point in the core of the shear layer for $z/c \leq 2.35$. Both parameters vary gradually in the inboard region ($1.25 \leq z/c \leq 1.85$). However, a notable increase in the bubble height is observed towards $z/c \approx 2.00$, where an increase in both the maximum height of the reverse flow region and streamwise displacement thickness takes place, which agrees with the trend seen in the side view 2C results (Fig. 4.7). For $z/c > 2.00$, a gradual decrease in LSB thickness occurs, until reverse flow is no longer observed in the tip region for $z/c > 2.30$. The accompanying reduction in displacement thickness is consistent with the findings of Awasthi *et al.* [22], who observed a substantial reduction in boundary layer thickness towards the tip of an $sAR = 0.5$ wing. Figure 5.4b shows the spanwise variation of the separation and reattachment lines and the projection of markers from Fig. 5.4a, which serve to locate the maximum height of the bubble. It can be seen that the location of maximum height of the $\overline{u} = 0$ isosurface and the streamwise displacement

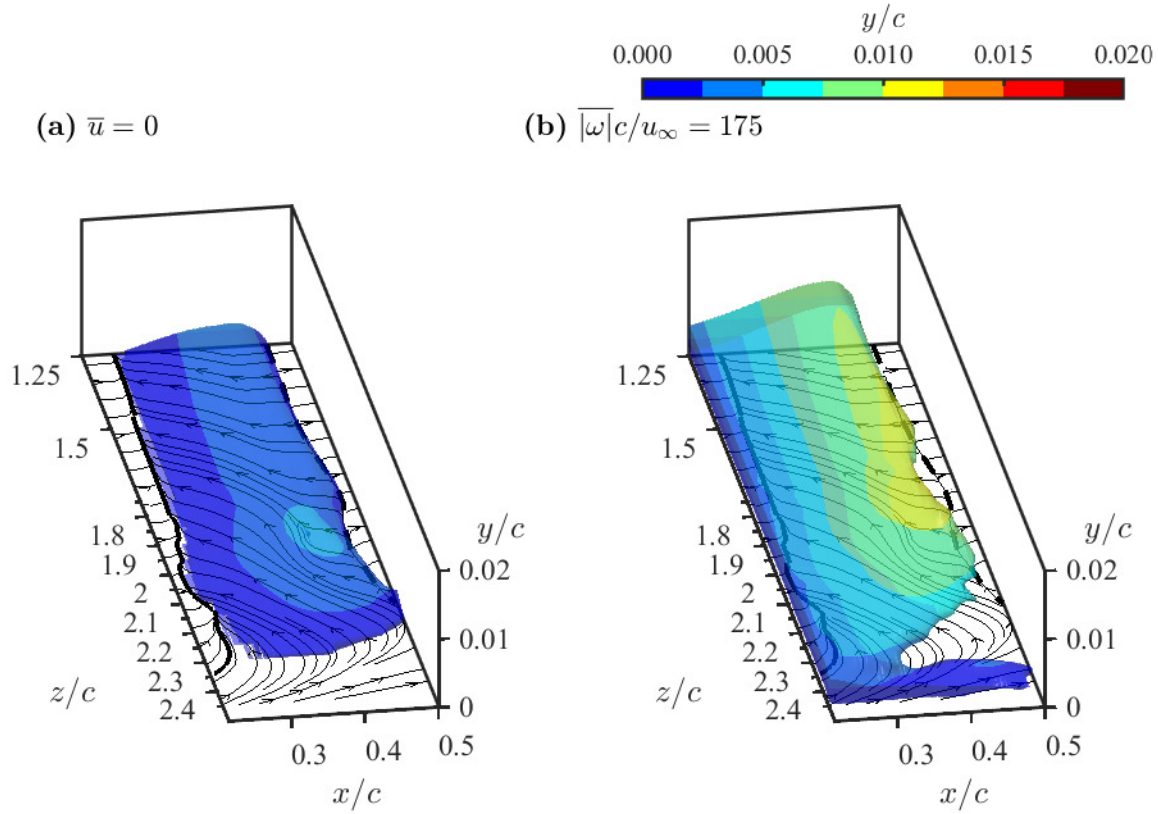

Figure 5.3: Isosurfaces of zero mean streamwise velocity and vorticity magnitude illustrating the spanwise shape of mean LSB structure. Contour colours indicate normal distance from wing surface. Thin lines: limiting streamlines; thick solid line: separation line; thick dashed line: reattachment line.

thickness closely coincide and follow the spanwise variations of the reattachment line. The separation and reattachment lines obtained from the limiting streamline topology are also compared with the contour of zero streamwise wall shear stress ($C_{fx} = 0$) in Fig. 5.4b. It can be seen that the contour of $C_{fx} = 0$ closely follows the separation and reattachment lines across the majority of the LSB. Only in the tip region, where the limiting streamlines are primarily in the spanwise direction, the zero streamwise wall shear stress contour begins to deviate from the separation line. This suggests that the two-dimensional definition of separation and reattachment based on zero streamwise skin friction can be used to identify the location and streamwise extent of an LSB on a finite wing, except for the immediate proximity of the wingtip.

Based on the observed changes in mean flow topology along the span, three characteristic regions can be identified. The inboard region is located within $1.25 \leq z/c \leq 1.85$ and characterized by nearly spanwise uniform LSB development. The tip region is confined to $z/c > 2.25$, where the flow is strongly influenced by three-dimensional tip effects, and characteristic LSB features are no longer observed. Between these regions, there

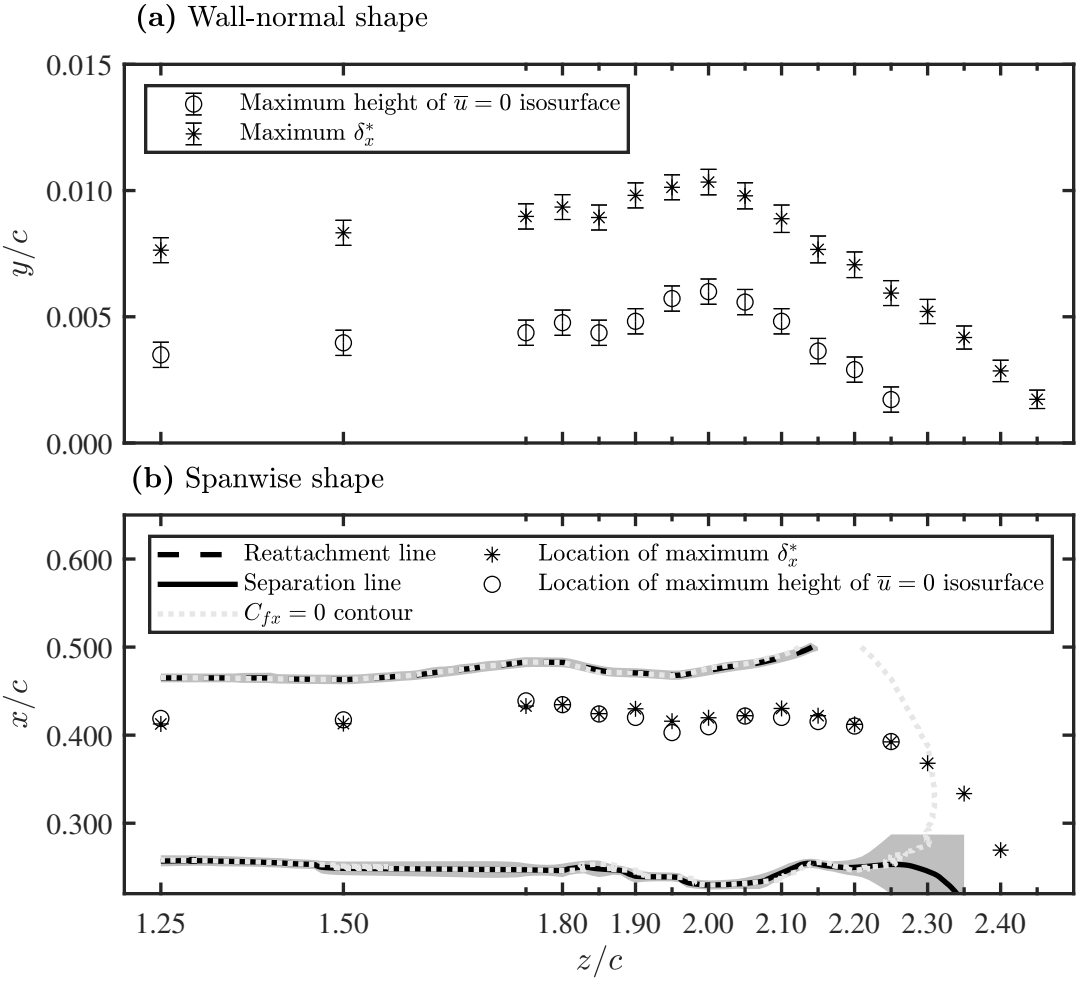

Figure 5.4: **(a)** Maximum height of $\overline{u} = 0$ isosurface and maximum δ_x^*. **(b)** Comparison of two- and three-dimensional separation and reattachment lines. Shaded region indicates uncertainty in separation and reattachment lines.

is an intermediate region ($1.85 < z/c \leq 2.25$), where the thickness of the LSB changes substantially and strong spanwise flow occurs within the reverse flow region.

To visualise the three-dimensional shape of the separation bubble, streamsurfaces of separation and reattachment were constructed from the side view 3C data and are presented in Fig. 5.5. The separation surface is formed by the set of streamlines originating from the separation line, e.g., [135]. Figure 5.5a shows that the LSB on the wing is an open bubble. Instead of forming a closed surface, the outboard portion of the separation surface is swept towards the wing root by spanwise flow, and fluid enters the LSB at its outboard open end. This is further substantiated by the trajectory of the reattachment surface in Fig. 5.5b, which is the streamsurface that emanates from the reattachment line in reverse time, e.g., [69]. Within the intermediate region, the reattachment surface passes over the separation surface and extends farther upstream ($2.10 \leq z/c \leq 2.25$), indicating that fluid is drawn into the LSB from above and outboard of the separation surface. Farther from the wingtip,

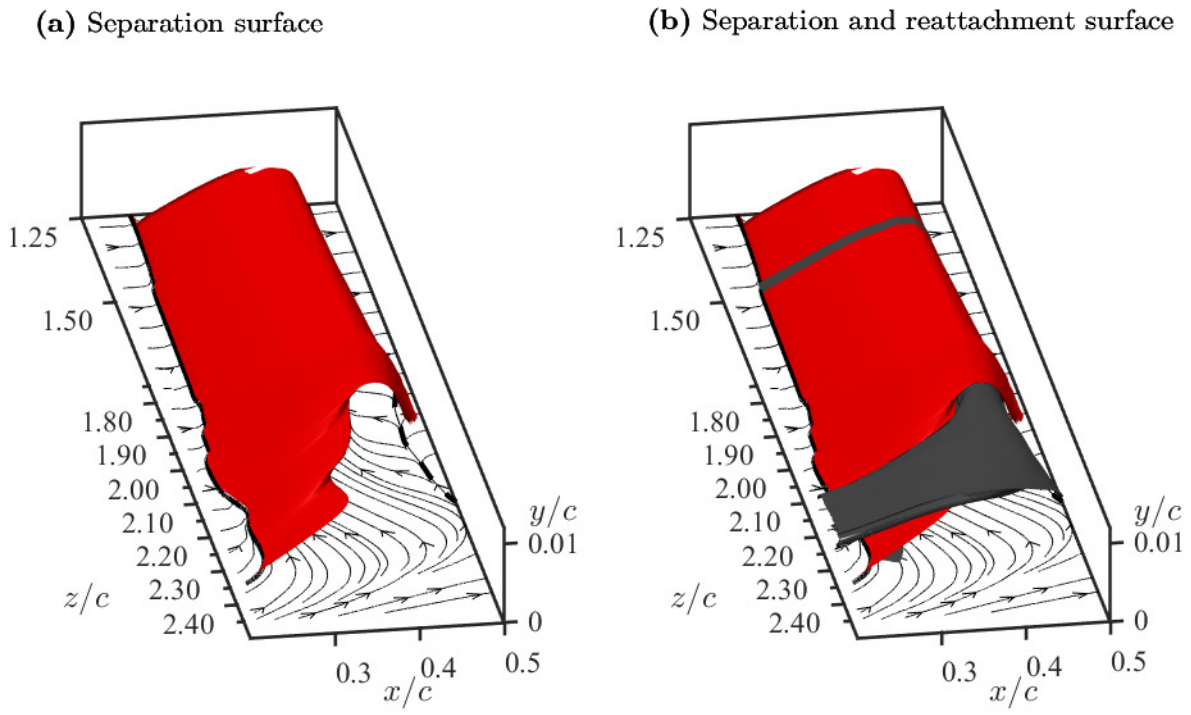

Figure 5.5: Streamsurfaces of separation and reattachment. Thin lines: limiting streamlines; thick solid line: separation line; thick dashed line: reattachment line.

the separation and reattachment surfaces approach the same shape, as indicated by the small segment of the reattachment surface near $z/c = 1.50$ that closely follows the outside of the separation surface. The convergence of the two streamsurfaces in the inboard region of the wing confirms that the bubble topology in $x - y$ planes approaches that of the closed two-dimensional separation bubble depicted in Fig. 2.1 away from the wingtip.

A more detailed insight into the open nature of an LSB on a finite wing can be gained from a planar control volume analysis applied to side view 3C velocity data from the spanwise region where an LSB is fully captured within the field of view of $x - y$ measurement planes ($1.25 \leq z/c \leq 2.10$). The definition of the planar control volume at $z/c = 1.25$ is shown in Fig. 5.6a, and the control volume boundaries at all other planes are located at the same x/c and y/c locations. The control volume boundary was placed around the aft portion of the LSB containing the reverse flow vortex (Fig. 2.1), where notable changes take place in the spanwise flow (Fig. 5.1c).

The conservation of mass for the planar control volume in an incompressible flow can

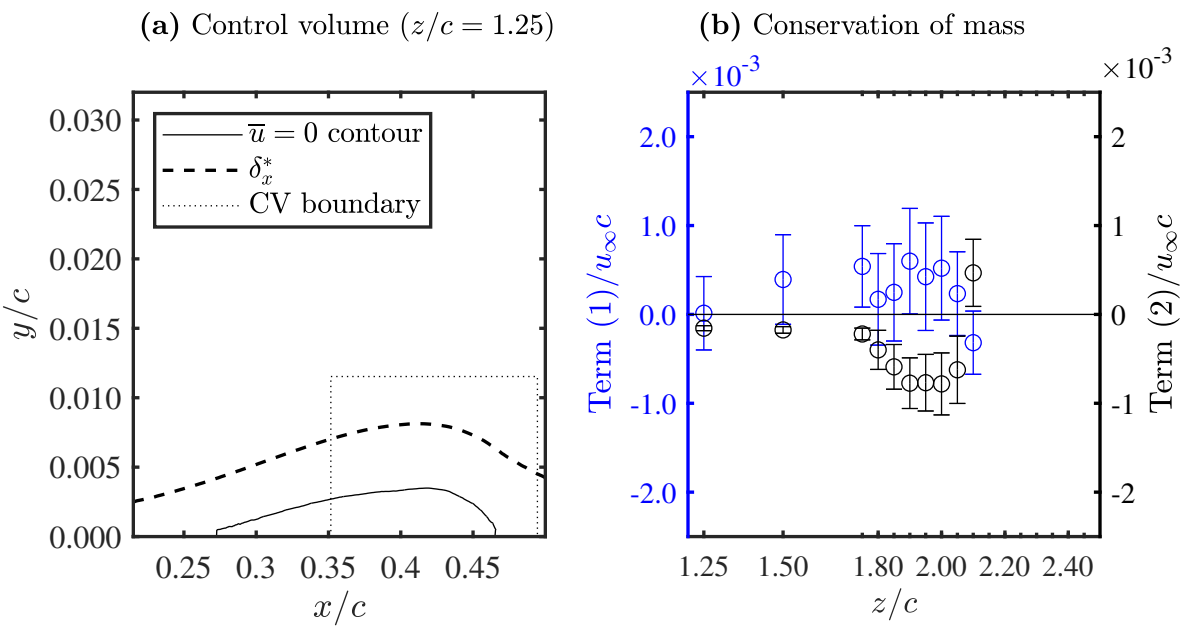

Figure 5.6: Control volume mass balance: **(a)** Control volume superimposed on the LSB outline at $z/c = 1.25$. **(b)** Terms (1) and (2) from Eq. 5.1.

be expressed as

$$0 = \oint_l \overline{\mathbf{u}} \cdot \hat{\mathbf{n}} dl + \iint_A \frac{\partial \overline{w}}{\partial z} dA = \underbrace{\oint_l \overline{\mathbf{u}} \cdot \hat{\mathbf{n}} dl}_{\substack{\text{Term (1):} \\ \text{In-plane outflow}}} + \underbrace{\frac{\partial \overline{\dot{V}}}{\partial z}}_{\substack{\text{Term (2):} \\ \text{Out-of-plane} \\ \text{outflow}}} \tag{5.1}$$

where A is the area of the planar control volume bounded by l and $\hat{\mathbf{n}}$ is the outward unit normal vector on the boundary. Term (1) represents the net in-plane outflow of fluid through the boundaries of the planar control volume due to the in-plane components (u and v) of the mean velocity ($\overline{\mathbf{u}}$) at the control volume boundaries. Term (2) represents the net out-of-plane outflow of fluid due to spanwise gradients in spanwise velocity, which is equal to the derivative of the mean bound spanwise volume flow rate ($\overline{\dot{V}}$) with respect to z.

Figure 5.6b presents the values of terms (1) and (2) for each of the planar control volumes. The observed changes in the spanwise gradient of the spanwise volume flow rate, and consequently term (2) in Eq. 5.1, necessitate changes in the net in-plane outflow (term (1), Eq. 5.1) through the control volume boundaries. It can be seen that, at a given spanwise location, the two terms add to zero to within the experimental uncertainty. Of particular interest, however, are the signs of the respective terms, distinguishing between inflow and outflow.

The last outboard plane that captures the full extent of the LSB is located at $z/c = 2.10$, where the LSB topology experiences notable changes due to the proximity of the wingtip,

including the reduction of the bubble height and downstream movement of the reattachment location (Fig. 5.4). In Fig. 5.6b, term (1) is negative at this location, reflecting the inflow into the open end of the LSB. As the gradient of the spanwise volume flow rate inside the LSB diminishes inboard, in-plane outflow (i.e., positive term (1)), is eventually attained, peaking in the intermediate region and then gradually decreasing towards the expected zero value for the nearly two-dimensional flow in the inboard region. The spanwise region of maximum in-plane outflow from the planar control volume matches that of maximum LSB thickness in Fig. 5.4a. Thus, the increase in LSB thickness in the intermediate region is attributed to changes in the mass exchange balance between the LSB and the surrounding fluid driven by the spanwise flow across the open end of the LSB. Consequently, the strong three-dimensional flow induced by the wingtip vortex not only causes open LSB formation and attached flow near the tip, but also induces notable spanwise changes to the LSB position, length, and height in the intermediate region.

5.2 Laminar to Turbulent Transition

Due to the critical role of shear layer transition in determining the overall mean LSB topology, the observed spanwise variations in the mean flow of the three-dimensional LSB on the wing are expected to be linked to changes in the transition process. The evolution of velocity perturbations in the shear layer is explored in Fig. 5.7, which presents contours of RMS velocity fluctuations. For the inboard region (e.g., at $z/c = 1.25$), the results reveal the progressive amplification of streamwise velocity fluctuations along the core of the separated shear layer, which is most prominent around the maximum height location. The attendant flow transition leads to mean flow reattachment, where saturation of velocity fluctuations is observed, agreeing with previous studies, e.g., [9, 26]. Near the x/c location of maximum bubble height, identifiable from the streamwise displacement thickness plots (dashed lines), the streamwise velocity fluctuation contours (Fig. 5.7a) exhibit three peaks, with the middle one aligned along the core of the shear layer, a structure expected from other experiments in separated shear flows, e.g., [35, 128] and linear stability predictions, e.g., [52, 136]. The wall-normal velocity fluctuations (Fig. 5.1b) for the inboard planes display a single peak along the trajectory of the separated shear layer, consistent with the formation of shear layer vortices. The observed trends persist in all measurement planes for $z/c \lesssim 2.00$ and are similar to those expected for a two-dimensional LSB, e.g., [137]. The spanwise velocity fluctuations captured in the present investigation (Fig. 5.7c) offer a novel insight into the progression of the last stages of the transition process, where onset of spanwise fluctuations is expected. It can be seen that similar levels of spanwise velocity fluctuations are achieved farther downstream compared to either streamwise or wall-normal components. As will be discussed later, these arise from spanwise deformations and subsequent breakdown of dominant shear layer vortices in the aft portion of the LSB.

Significant changes in the development of shear layer velocity fluctuations take place in intermediate region for $z/c > 2.00$ (Fig. 5.7). Most notably, a progressive downstream shift of the transition process can be seen between $z/c = 2.05$ and 2.25, and no significant velocity

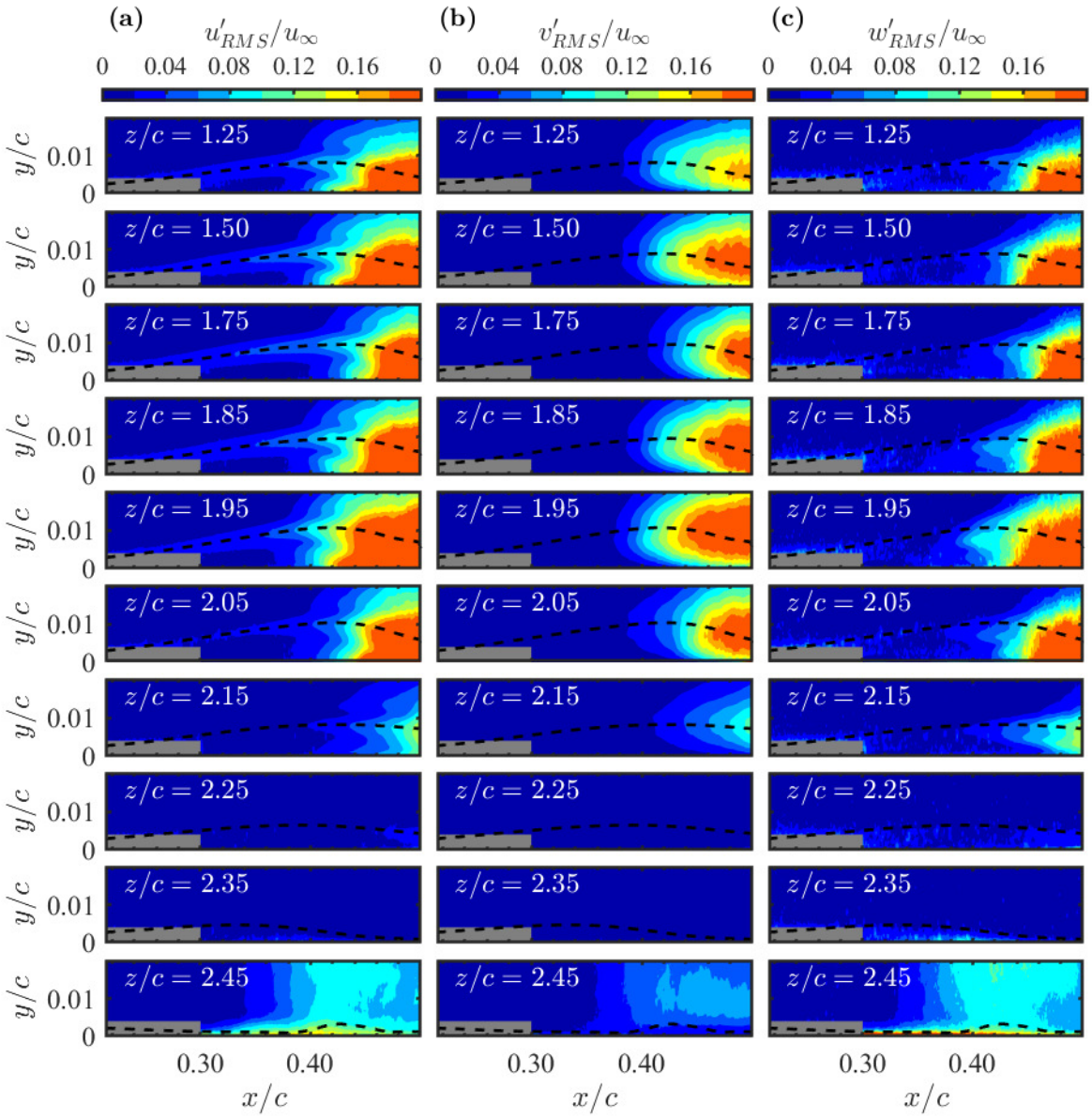

Figure 5.7: RMS velocity fluctuation contours. Dashed line: streamwise displacement thickness. Masked flow area within $0.22 < x/c < 0.30$ pertains to region of relatively high random errors near the wall.

fluctuations are observed within the field of view in the tip region at $z/c = 2.25$ and 2.35. Figure 5.8a presents a convenient comparison basis for the assessment of spanwise variations in turbulent kinetic energy (TKE) at the core of the shear layer superimposed on the mean separation and reattachment lines. Also presented is the streamwise location of maximum shape factor $H_x = \delta_x^*/\theta_x$, which has been shown to be a robust criterion for defining a mean transition location in two-dimensional LSBs, e.g., [138]. A rapid growth in turbulent kinetic energy occurs in the aft portion of the LSB for $z/c \lesssim 2.10$. Within the same spanwise region, the x/c location of maximum shape factor follows the shape of the TKE contours and the reattachment line, indicating that the spanwise variation seen in the reattachment location is related to the variation in the transition process. In contrast, for $z/c \gtrsim 2.15$, the location of maximum shape factor moves upstream, while no significant TKE levels are reached within the field of view. This signifies that estimation of the transition location using the two-dimensional definition of the shape factor is no longer valid near the wingtip, and the flow behaviour is largely governed by the three-dimensional wingtip effects. In contrast, within the inboard and intermediate regions of the span, the formation of the LSB is largely driven by the shear layer transition, similar to the two-dimensional LSB formation.

Added insight into local flow stability can be gained from the results in Fig. 5.8b, which presents the spanwise variation in maximum shape factor and minimum streamwise velocity. In the inboard region, both the shape factor and minimum streamwise velocity remain unchanged within the experimental uncertainty. However, in the intermediate region ($1.85 < z/c < 2.25$) changes in both parameters take place, and significant extrema occur around $z/c = 2.10$. Here, the minimum streamwise velocity reaches $-0.25u_\infty$, which exceeds the threshold of -0.15 to $-0.2u_\infty$ for absolute instability in LSBs reported by Alam & Sandham [54] from direct numerical simulations. Although the increase of shape factor and reverse flow velocity with increasing z/c from $z/c = 1.95$ to $z/c = 2.10$ would be expected to increase the instability of the separated shear layer [35], a downstream movement in the location of maximum shape factor and delay in TKE production occurs. Considering that these changes coincide with the region of substantial spanwise flow within the LSB (Fig. 5.1c), it implies that the transition process becomes more strongly influenced by three-dimensional effects closer to the wingtip. In the tip region ($z/c \geq 2.25$) where transition is delayed, a continued decrease in maximum shape factor and increase in minimum streamwise velocity occurs with increasing z/c. Concurrently, the thickness of the reverse flow region is reduced before separation ceases entirely near the wingtip (Fig. 5.4a), consistent with the reduction of the adverse pressure gradient (Fig. 4.1b).

To further explore the spanwise variations in the transition process, the growth of wall-normal velocity fluctuations, which are strongly associated with the formation of spanwise vortices that lead to transition, e.g., [118], is explored in Fig. 5.9. Wall-normal RMS velocity fluctuations at $y = \delta_x^*$ are compared at representative spanwise locations in the inboard ($z/c = 1.25$) and intermediate ($z/c = 1.95$, 2.15, and 2.20) regions in Fig. 5.9a. Only v'_{RMS} values exceeding the uncertainty from correlation statistics with a 95% confidence level are shown. Also plotted for reference is the growth of v'_{RMS} from the two-dimensional airfoil at the same effective angle of attack as the inboard region of the wing (5°), based on data from

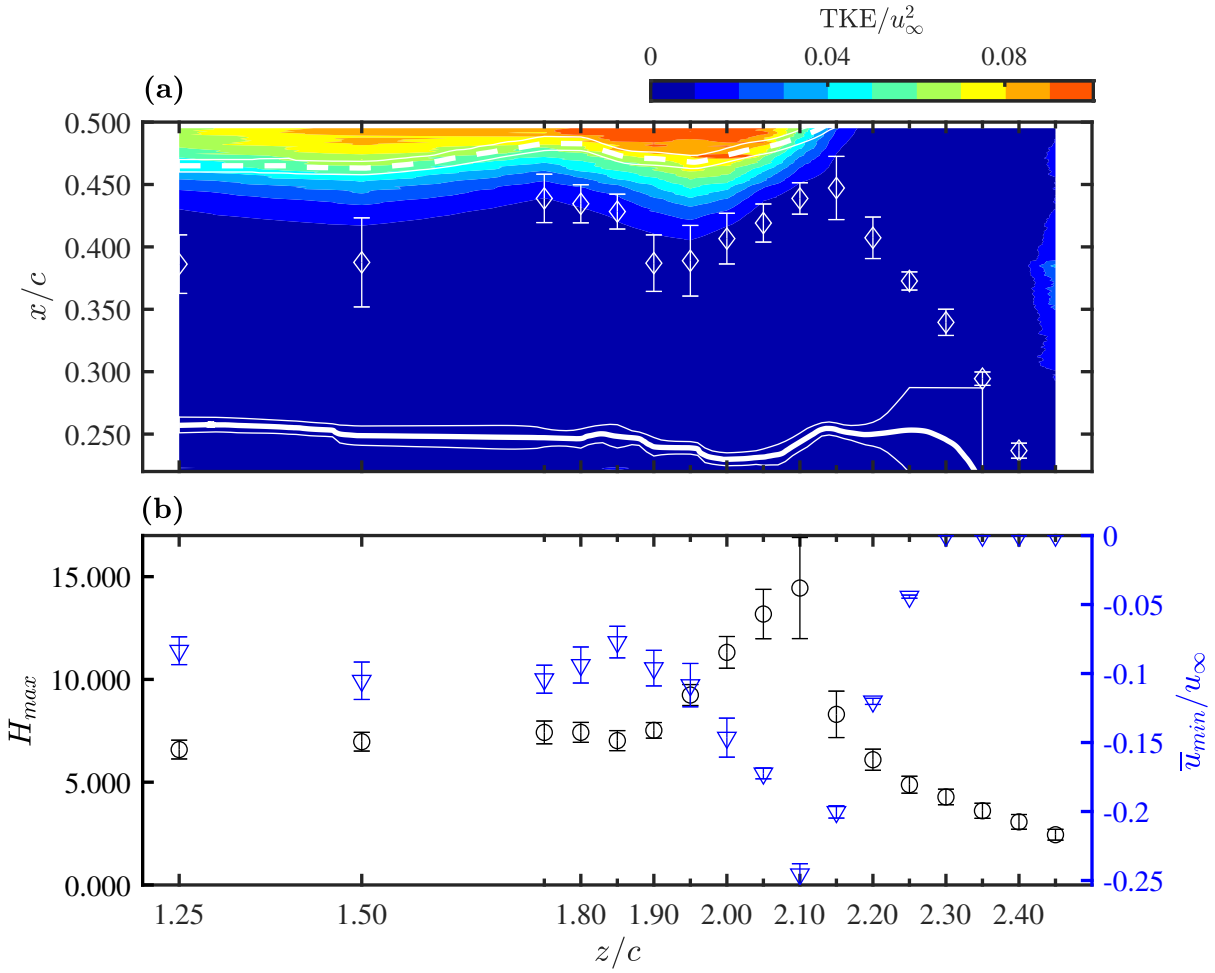

Figure 5.8: **(a)** Contours of turbulent kinetic energy at $y = \delta_x^*$. Solid line: separation line; dashed line: reattachment line; diamonds: location of maximum streamwise shape factor. Thin lines indicate uncertainty in separation and reattachment lines. **(b)** Maximum shape factor and minimum streamwise velocity.

the side view 2C configuration. Maximum streamwise growth rates of RMS wall-normal velocity fluctuations ($\sigma_{v'max} = \ln(\Delta v'_{RMS}/u_\infty)/(\Delta x/c)$, e.g., [27]) are plotted in Fig. 5.9b. The markers in Fig. 5.9a indicate the regions of approximately constant exponential growth that were used to estimate the maximum growth rates for each respective v'_{RMS} curve.

For $z/c \leq 2.10$, the initial growth rates of v'_{RMS} are similar to the two-dimensional airfoil at the effective angle of attack, and the velocity fluctuations saturate at a similar level. However, closer to the wingtip, the maximum growth rate of v'_{RMS} is reduced substantially. The notable reduction in the growth rate of v'_{RMS} at the outboard end of the intermediate region (Fig. 5.9b) is consistent with the delay in transition observed on this part of the span in Figs. 5.7 and 5.8a. This delay in transition is in agreement with the results of Smith & Ventikos [95], who observed a reduction in the growth of Tollmein-Schlichting waves near the wingtip in an attached boundary layer. The results confirm that the flow development

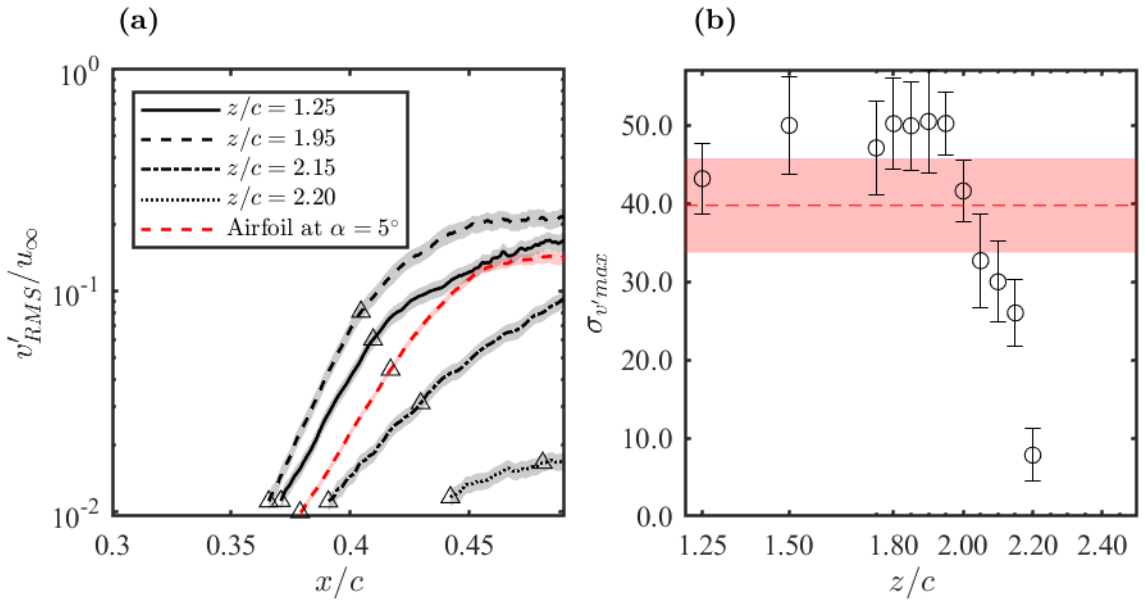

Figure 5.9: **(a)** Streamwise growth of v'_{RMS} at $y = \delta^*_x$ on the wing at $\alpha = 6°$ compared to the airfoil at the effective angle of attack of the midspan. Shaded regions indicate uncertainty. Triangle markers indicate interval used to calculate $\sigma_{v'max}$ **(b)** Maximum streamwise growth rates of v'_{RMS}. Dashed line: airfoil at effective angle of attack of midspan.

in the tip region is largely governed by the induced flow, which eliminates separation and terminates LSB, while delaying transition significantly.

5.3 Vortex Dynamics

Shear layer vortex shedding is known to play a key role in LSB dynamics, e.g., [26, 37]. The development of shear layer vortices in the investigated LSB is illustrated in Fig. 5.10, which presents an instantaneous velocity field from the top view 2C configuration and insets of instantaneous spanwise vorticity and λ_2 criterion [127] contours at selected spanwise positions from uncorrelated side view 3C measurements. In the top view 2C snapshot, the spanwise structure of the rollers can be observed. Because the light sheet was positioned to intersect the tops of the roll-up vortices, the vortices appear as spanwise bands of positive streamwise velocity fluctuations. Notable periodic velocity fluctuations can be seen just upstream of and at the mean reattachment line. They display a strong degree of spanwise coherence along the inboard portion of the wing, comparable to observations on two-dimensional geometries at similar turbulence levels, e.g., [27, 102, 130]. However, as the wingtip is approached, the vortices begin to develop progressively more pronounced spanwise undulations. Eventually, no clear signs of periodic shedding are observed in the tip region ($z/c \geq 2.25$). Across the portion of the span where shedding is seen, the spanwise

structures rapidly lose coherence and break down downstream of mean reattachment, with signs of vortex breakdown appearing earlier upstream in the intermediate region ($1.90 < z/c < 2.25$).

The presence of periodic shedding of shear layer structures across the majority of the span is confirmed by the insets from side view 3C measurements. Note that the streamwise extent of the side view 3C measurements is smaller than that of the top view 2C measurements. The insets show that the formation of vortices occurs in the aft portion of the LSB, and the roll-up location remains similar across the span for $z/c < 2.00$. With increasing z/c in the inboard region, the distance between the vortex trajectory and the surface also increases, and this trend continues in the intermediate region up to $z/c = 2.00$, following the increase in the mean height of the separation bubble (Fig. 5.4a). Closer to the wingtip, at $z/c = 2.15$, vortices can still be identified, but they form farther downstream and closer to the wing surface. The strength of the roll-up vortices rapidly diminishes in the field of view between $z/c = 2.15$ and 2.20, and no roll-up can be seen at $z/c = 2.25$. This is consistent with the less rapid growth of wall-normal velocity fluctuations at these spanwise locations in Fig. 5.9b, and is in agreement with linear stability theory, which predicts a decrease in disturbance growth rates as the inflection point of the shear layer moves closer to the wall, e.g., [52]. The absence of shear layer roll up at and beyond $z/c = 2.25$ is substantiated by the top view 2C results that cover a larger streamwise extent of the flow, indicating that shedding is suppressed and that the flow remains laminar near the wingtip. Despite the absence of shear layer roll-up in the tip region, the separated shear layer still curves towards the wing surface. However, mean reattachment is not driven by the increase in wall-normal momentum transfer caused by shear layer roll-up vortices but by the rapid decrease in the adverse pressure gradient and downwash induced by the wingtip vortex, which eventually suppress separation closer to the wingtip.

The progression of the fundamental vortex shedding cycle is illustrated by the POD-based phase averaged results (Section 3.3.1) for selected side view 3C planes and the top view 2C configuration in Figs. 5.11–5.13.

Figure 5.11 presents a sequence of contours of phase averaged spanwise vorticity ($\tilde{\omega_z}$) and λ_2 for selected z/c planes at phase angles of $\Theta = 0, \pi/2, \pi$, and $3\pi/2$. Within the inboard region ($z/c = 1.25$, Fig. 5.11a), a typical periodic vortex shedding is seen in the LSB. At $z/c = 2.00$ (Fig. 5.11b), representative of the intermediate region where a notable increase in the mean bubble height is observed due to the increased three-dimensional effects (Fig. 5.4a), vortex formation shifts upstream slightly and larger vortices are formed. A small upstream shift in the reattachment line that occurs near $z/c = 2.00$ (Fig. 5.2) is attributed to the formation of stronger vortices at this location. The increased strength of the shed structures produces stronger mean reverse flow at this spanwise location (Fig. 5.8b) and is also reflected in the increase in the production of positive vorticity near the wall. Closer to the wingtip ($z/c = 2.15$, Fig. 5.11c), the mean shear layer moves closer to the surface of the wing due to the progressively increasing wingtip vortex influence, the roll-up moves downstream, and smaller structures form in the separated shear layer, in agreement with the delayed growth of RMS velocity fluctuations seen at the corresponding location in Fig. 5.7. Farther outboard in the tip region, at $z/c = 2.25$ (Fig. 5.11d), no roll-up is seen

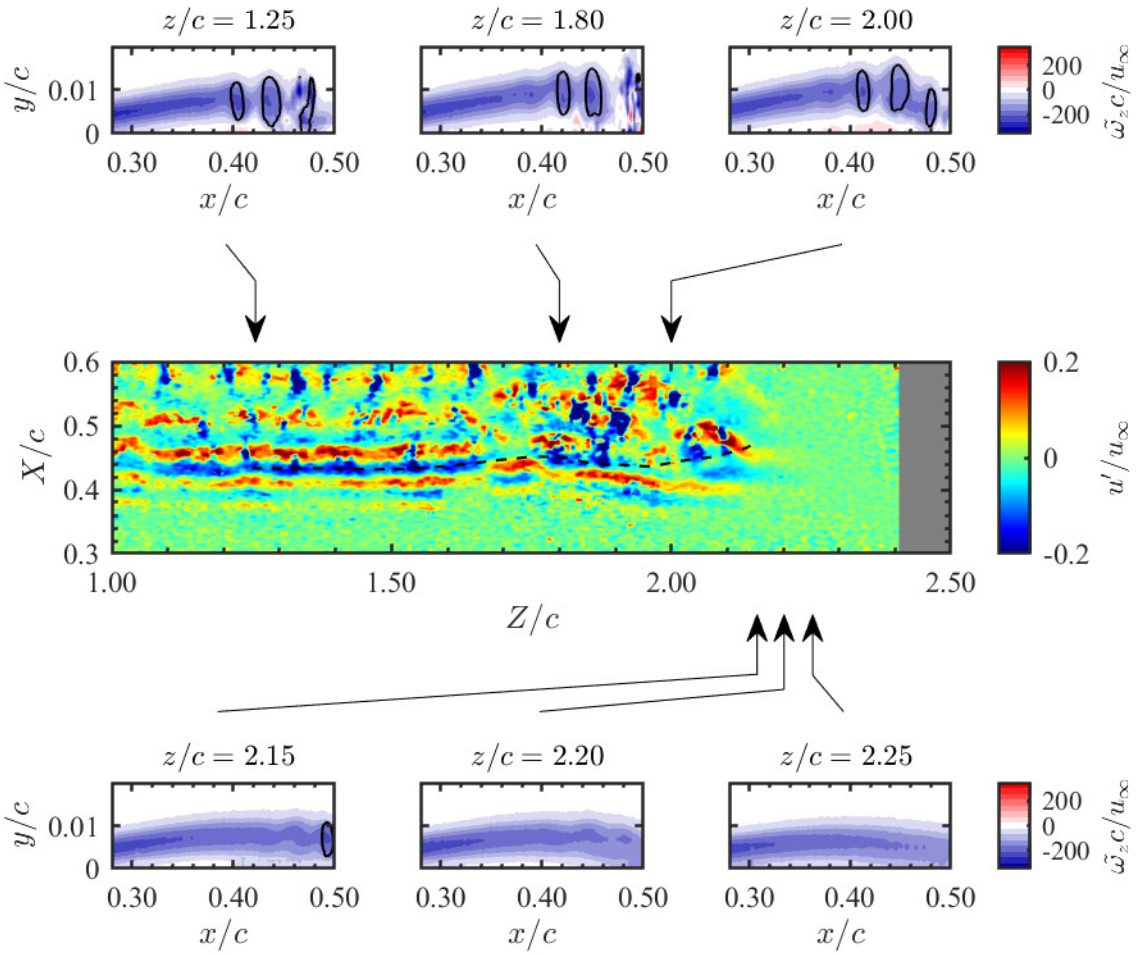

Figure 5.10: Instantaneous flowfield snapshots illustrating vortex shedding in LSB. The central image presents streamwise velocity fluctuation contours from top view 2C measurements. Insets present contours of spanwise vorticity and $\lambda_2 c/u_\infty = -1500$ from uncorrelated side view 3C measurements at selected $x - y$ planes along the span. Dashed line: reattachment line from Fig. 5.2b

and the flow remains laminar, however, minor periodic oscillations can still be observed.

To explore the interaction of spanwise flow with the shear layer rollers, Fig. 5.12 presents phase averaged spanwise velocity ($\tilde{w}$) and λ_2 for the same planes and phase angles as those in Fig. 5.11. In the inboard region ($z/c = 1.25$, Fig. 5.12a), no significant spanwise velocity fluctuations are observed. In the intermediate region, at $z/c = 2.00$ (Fig. 5.12b), shed vortices entrain high-spanwise momentum fluid concentrated within the LSB and advect it downstream. A similar interaction is seen at $z/c = 2.15$ (Fig. 5.12c). Eventually, sufficiently close to the wingtip, shedding is suppressed ($z/c = 2.25$, Fig. 5.12d), and only minor perturbations can be seen in the spanwise velocity contours. The results in Fig. 5.12 show that the interaction between shear layer vortices and spanwise flow leads to the entrainment

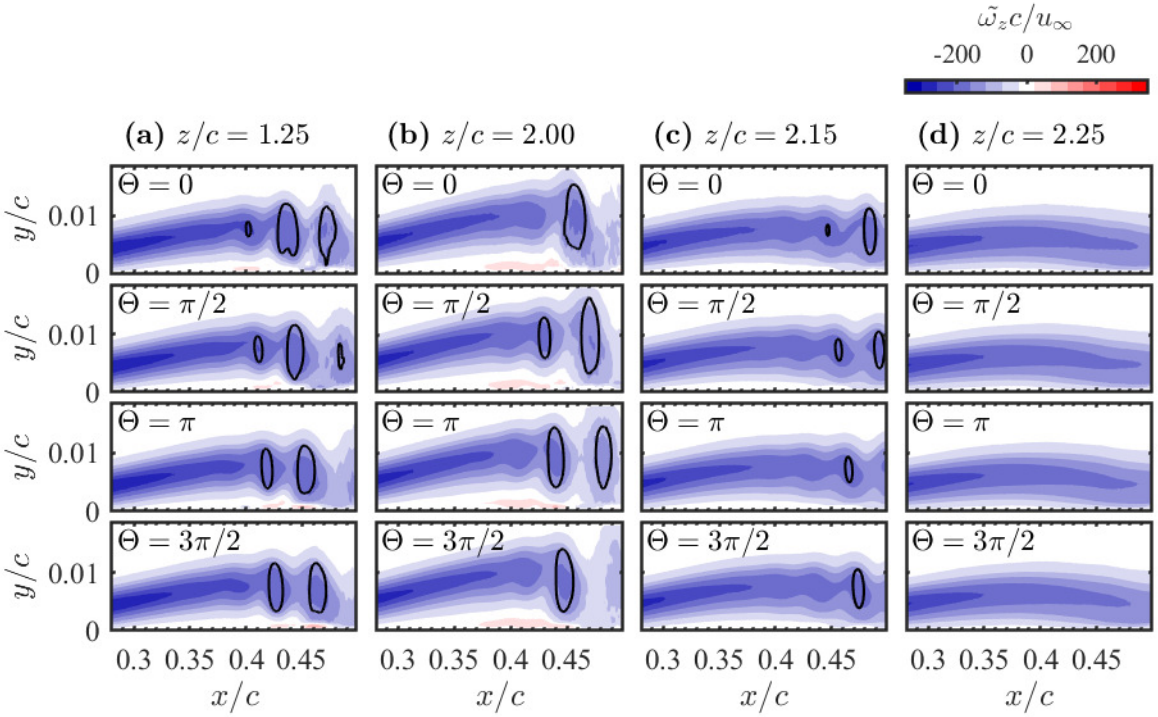

Figure 5.11: Phase averaged contours of $\tilde{\omega}_z$ at selected side view 3C measurement planes. Black lines are contours of $\tilde{\lambda}_2 c^2/u_\infty^2 = -1500$.

of spanwise momentum into the vortex cores in the intermediate region. This may be the underlying cause of the stronger spanwise undulations and earlier vortex breakdown in the intermediate region (Fig. 5.10), since axial flow is known to destabilise vortex filaments, e.g., [139].

The spanwise variation of the fundamental vortex shedding cycle is illustrated by the contours of phase averaged streamwise velocity ($\tilde{u}$) presented in Fig. 5.13. The phase averaged results confirm the strong two-dimensionality of the roll-up vortices in the inboard region ($z/c \leq 1.80$). Closer to the wingtip, greater spanwise variations in the vortex cores take place within the range $1.75 < z/c < 2.10$, and the shedding process eventually terminates around $z/c = 2.15$. In the range $1.85 < z/c < 2.10$, where earlier breakdown of coherent fluctuations is seen in Fig. 5.10, the phase averaged roll-up vortices in Fig. 5.13 do not persist as far downstream into the redeveloping turbulent boundary layer as they do in the inboard region, providing further evidence that the entrainment of spanwise momentum into the vortex cores in the intermediate region leads to earlier vortex breakdown.

To assess the relative level of cycle-to-cycle variability in the vortex shedding process at each side view 3C measurement location, vortex core identification was performed using the λ_2 criterion from instantaneous velocity fields in each side view 3C measurement plane. The vortex cores were identified within regions of λ_2 criterion below a threshold of $-1500u_\infty^2/c^2$ (e.g., Fig. 5.10 insets) with a minimum area greater than that of a circle with a diameter equal to 1/4 of the average streamwise wavelength of the structures. The $x-y$ locations of

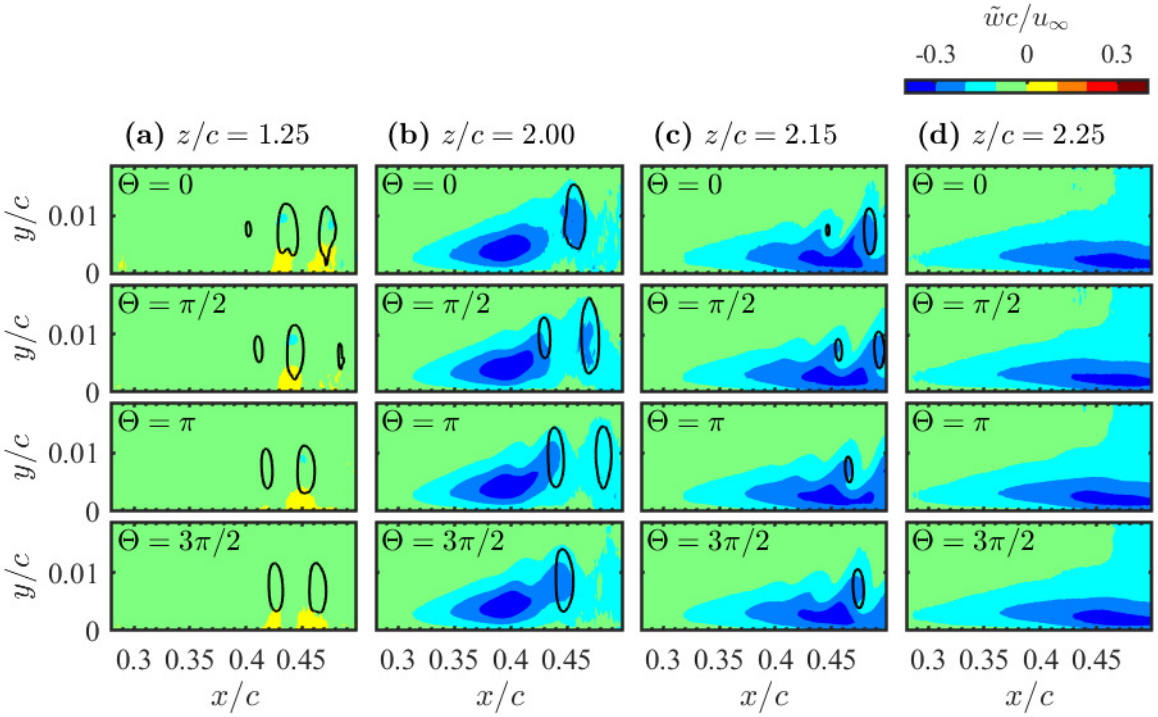

Figure 5.12: Phase averaged contours of $\tilde{w}$ at selected side view 3C measurement planes. Black lines are contours of $\tilde{\lambda}_2 c^2/u_\infty^2 = -1500$.

the identified vortex cores were computed from the centroid of the associated λ_2 threshold contours. Vortex cores were discarded if they did not correspond to a local λ_2 minimum with a prominence of at least $1500u_\infty^2/c^2$. The selected procedure was verified to consistently identify vortices in the aft portion of the LSB.

The distribution of identified vortex core locations is presented for selected representative planes in Figs. 5.14a–5.14d, where the mean of the wall-normal vortex core position calculated using a sliding window of $0.01c$ is indicated by a solid line. The results show vortices closely follow the core of the separated shear layer approximately marked by the streamwise displacement thickness. An increased variability in the vortex core location is seen in the aft portion of the bubble, which is attributed to the increased spanwise vortex deformations and onset of vortex breakdown in the vicinity and downstream of the mean reattachment. A comparison of Figs. 5.14a–5.14d indicates that the largest variations in the vortex core position within different planes along the span are observed in the intermediate region, where the average height of LSB is maximized.

Figure 5.14e presents the spanwise variation in the mean wall-normal distance to the vortex cores computed at the x/c location of maximum bubble height at each z/c plane. Also shown is the average streamwise wavelength (λ_0), estimated as the average streamwise distance between all identified vortex cores in each plane. The spanwise trend in the mean wall-normal vortex core distance is similar to the trend in the maximum bubble height (Fig. 5.4a), with a local maximum in mean wall-normal distance occurring in the

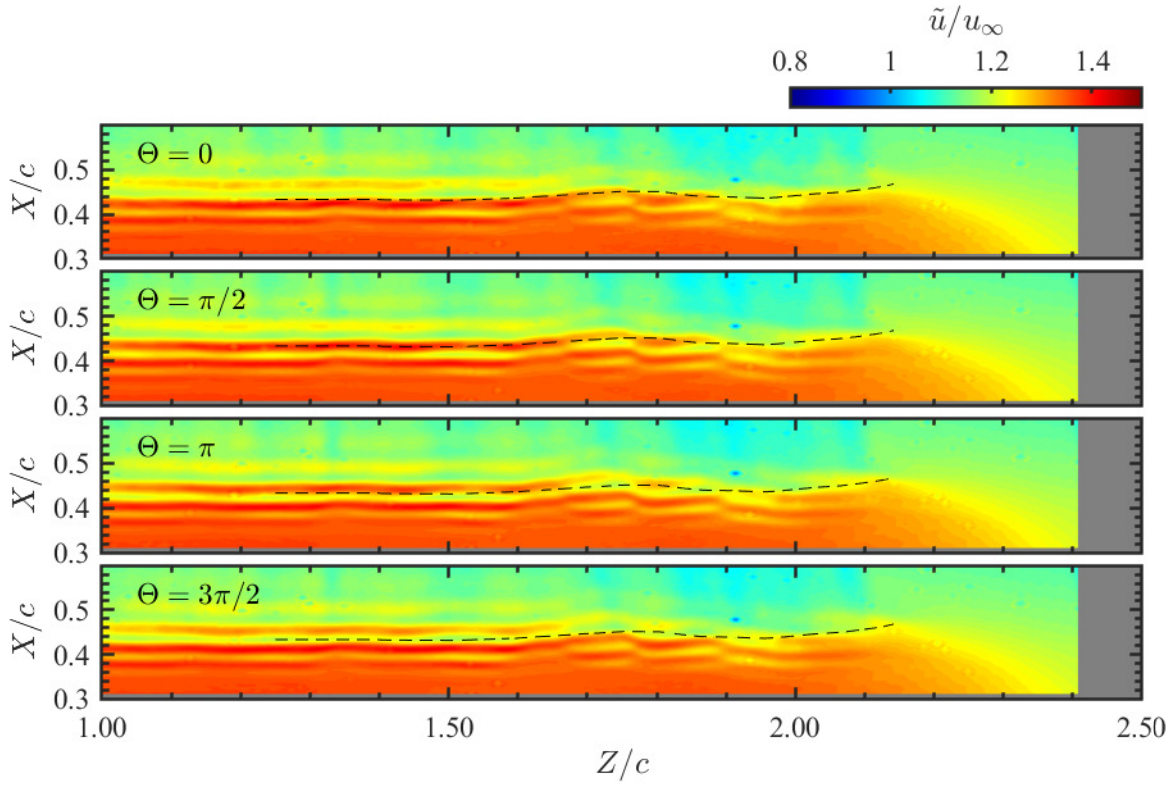

Figure 5.13: Phase averaged contours of $\tilde{u}$ from the top view 2C configuration. Dashed lines: reattachment line from Fig. 5.2b

intermediate region near $z/c = 1.95$. Consistent with the top view 2C measurements (Fig. 5.10g), the mean streamwise wavelength is largely invariant along the span, showing a minor increase closer to the wingtip. The shaded regions in Fig. 5.14e correspond to standard deviation bounds and serve to illustrate the variability in the presented quantities. It can be seen that the variability of the wall-normal vortex core distance in a given plane is greatest in the intermediate region where the vortices form farther from the surface, however the variability in streamwise wavelength is slightly reduced in this region. As the separated shear layer forms closer to the wing surface at the outboard end of the intermediate region ($2.00 \leq z/c \leq 2.15$,Fig. 5.4a) and transition becomes delayed, variability in wall-normal distance of vortex cores is reduced. In contrast, the variability in streamwise wavelegnth at $z/c = 2.15$ remains comparable to locations farther inboard.

To analyse spanwise changes in the vortex dynamics in more detail, POD was conducted on the measurements of the three-component velocity fluctuation vector $\mathbf{u}'$, and the in-plane velocity fluctuation vector (u', w'), from the side view 3C and top view 2C configurations, respectively. The relative POD modal energies of the first twenty POD modes are presented in Figs. 5.15 and 5.16, for the side view 3C and top view 2C configurations, respectively. Modes 1 and 2 of $\mathbf{u}'$ contain a notably greater fraction of the total turbulent kinetic

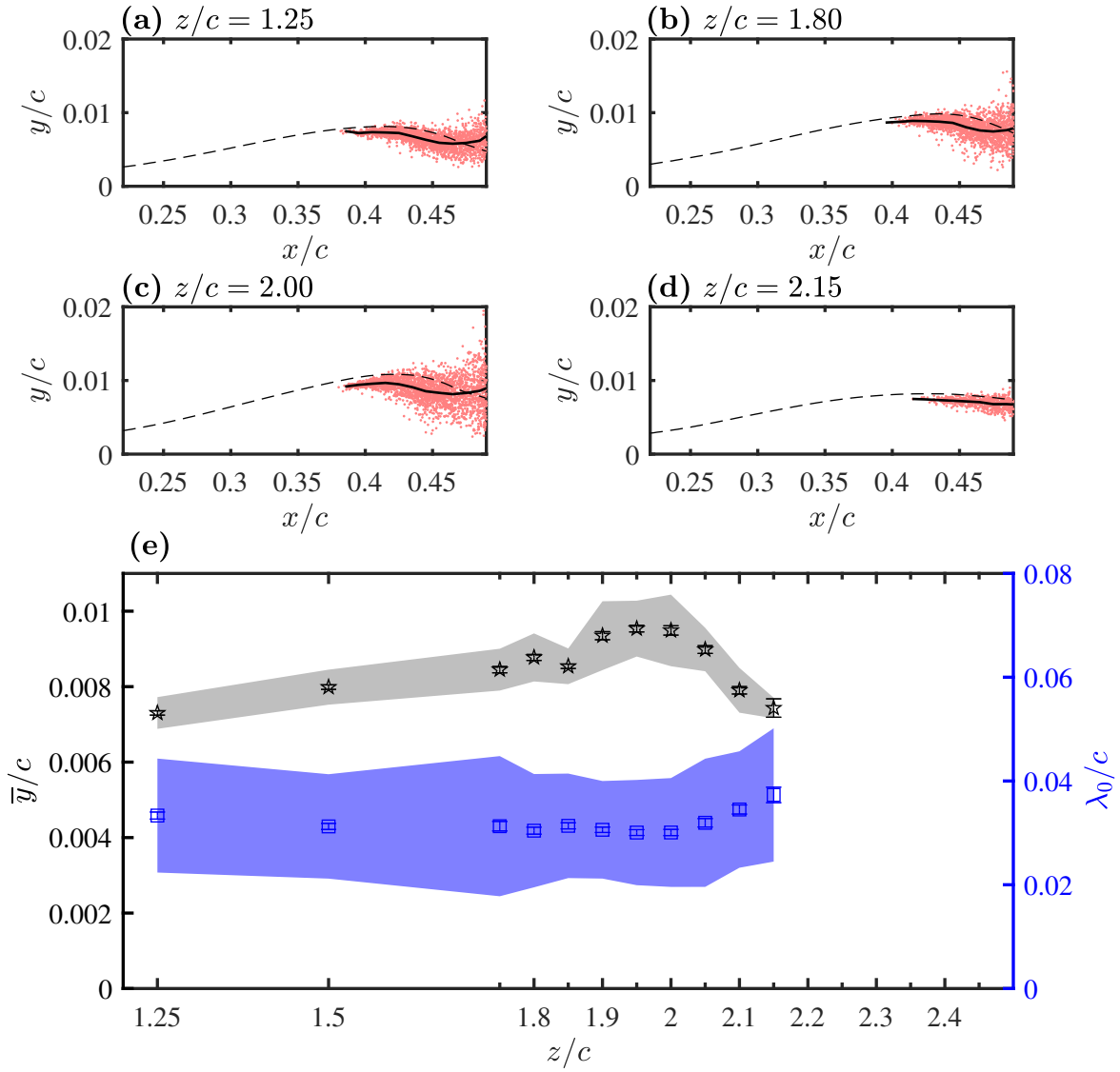

Figure 5.14: **(a-d)** Locations of vortices identified from side view 3C PIV. Dashed line: streamwise displacement thickness; solid line: mean wall-normal distance. **(e)** Mean wall-normal vortex distance at x/c location of maximum bubble thickness and mean streamwise wavelength. Error bars indicate statistical uncertainty in mean quantities, shaded regions indicate $\pm$ one standard deviation in the corresponding quantities.

energy than the higher modes and are paired for $z/c \leq 2.15$, which was confirmed by the examination of the corresponding spatial modes. Pairing also occurs between the first two POD modes of (u', w') from the top view 2C measurements. The side view 3C results are consistent with the prominent shedding of shear layer vortices in the same spanwise region seen in Fig. 5.10. At $z/c > 2.15$, the relative energy content of the first two modes of $\mathbf{u}'$ is reduced significantly, consistent with the suppression of shear layer shedding near the wingtip.

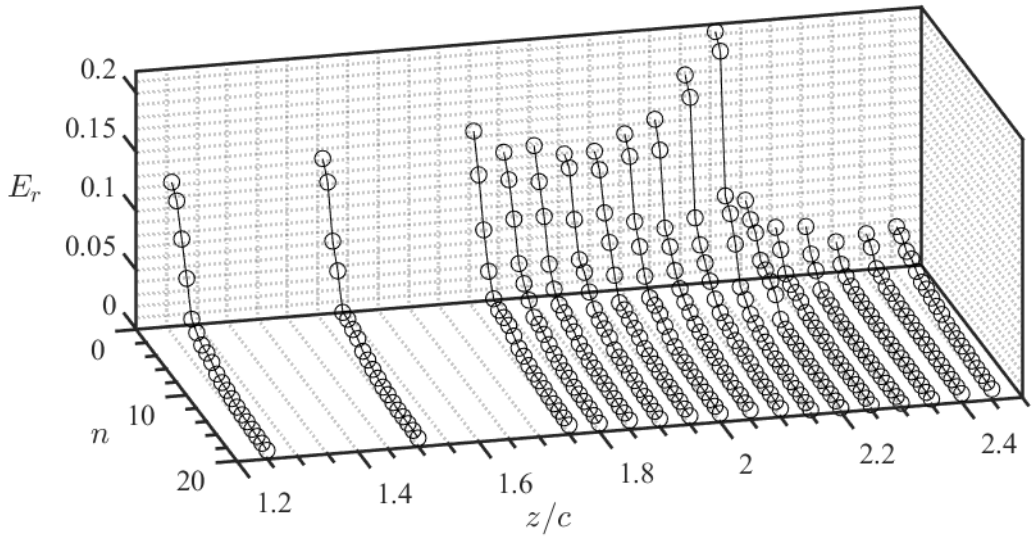

Figure 5.15: Relative modal energy of the first twenty POD modes of $\mathbf{u}'$ at each side view 3C measurement plane.

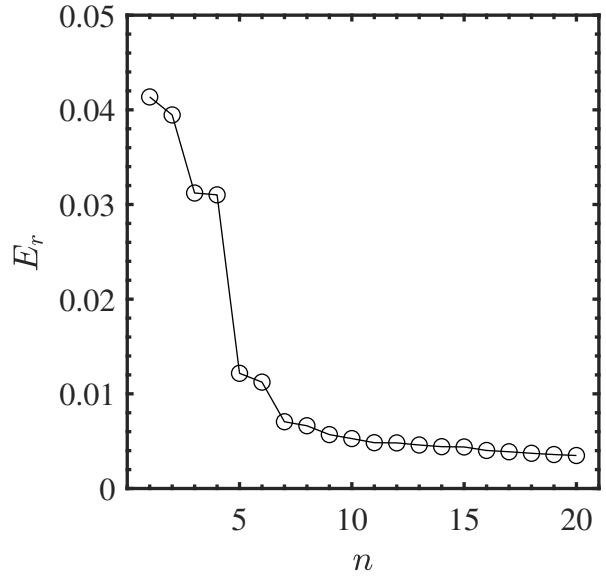

Figure 5.16: Relative modal energy of the first twenty POD modes of (u', w') from top view 2C measurements.

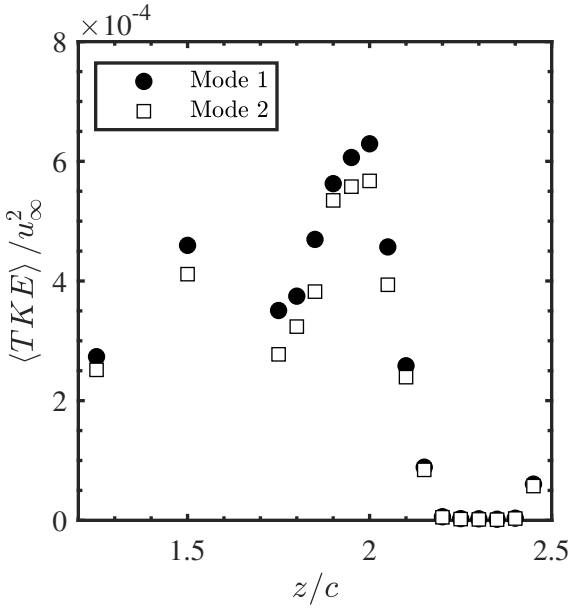

Figure 5.17: Spatially averaged turbulent kinetic energy of the first two POD modes of $\mathbf{u}'$ at each side view 3C plane.

Since the level of turbulent kinetic energy varies substantially in the spanwise direction in the aft portion of the LSB (Fig. 5.8a), it is instructive to compare the absolute energy content of the side view 3C POD modes. Figure 5.17 plots the spatially averaged turbulent kinetic energy ($\langle$TKE$\rangle$) of the first two modes for each measurement plane, which can be used to compare absolute modal energy content between different spanwise locations. A relative increase in the energy content of the first two modes is seen at $z/c = 2.00$, where formation of stronger vortices was observed due to the increase in the height of the mean LSB. However, similar to the distribution of relative modal energy, the absolute modal energy of the dominant mode pair is greatly reduced in the tip region, where shear layer vortices weaken and shedding eventually ceases. Although a peak in relative modal energy of POD modes 1 and 2 of $\mathbf{u}'$ occurs at $z/c = 2.15$ (Fig. 5.15), Fig. 5.17 shows that the absolute energy contained in these modes at $z/c = 2.15$ is substantially less than that at the neighbouring inboard planes ($z/c \leq 2.10$). This is attributed to the delayed shear layer roll-up (Figs. 5.10d and 5.11c) and the associated reduction in the energy of random turbulent fluctuations within the field of view. Thus, although weaker velocity fluctuations are produced by the vortices here, the relative energy of the associated modes increases since the structures do not break down within the field of view.

The most energetic spatial POD mode ($\mathbf{\Phi}^{(1)}$) is presented in Fig. 5.18 for representative planes, and the paired mode ($\mathbf{\Phi}^{(2)}$) is not shown for brevity. The largest magnitudes of $\mathbf{\Phi}^{(1)}$ occur in the aft portion of the LSB for $z/c \leq 2.15$, where shear layer vortices are observed in Fig. 5.10. A typical periodic spatial pattern of positive and negative wall-normal velocity seen in the aft portion of the field of view in Figs. 5.18a–5.18d confirms the association between the dominant mode pair and the shear layer vortices within this spanwise region. The results show that the spanwise mode component is notably lower than

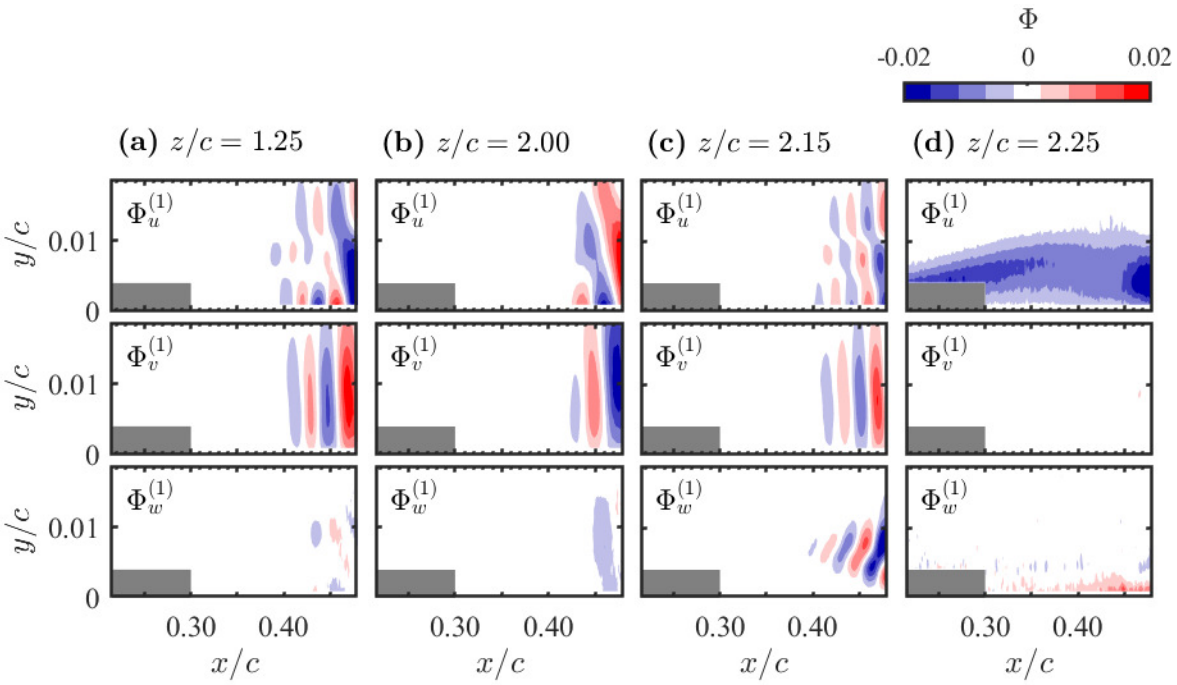

Figure 5.18: First spatial POD modes from side view 3C PIV at selected planes. Masked flow area within $0.22 < x/c < 0.30$ pertains to region of relatively high random errors near the wall.

the streamwise and wall-normal components at the onset of shear layer roll-up, supporting the earlier observation of nominally two-dimensional initial shear layer roll-up. However, a progressive increase in the spanwise component of $\mathbf{\Phi}^{(1)}$ can be seen at the same x/c locations for $z/c = 2.00$ and 2.15, correlating with the increase in spanwise deformations of the structures seen in the intermediate region (Figs. 5.10g and 5.13) and the entrainment of spanwise-momentum by the shed vortices (Fig. 5.12). Mode 1 at $z/c = 2.25$ does not display a spatially periodic pattern associated with vortex formation, and modes 1 and 2 are no longer paired at this spanwise location, consistent with the absence of shear layer vortices in the tip region. Here, mode 1 is mostly associated with the u-component fluctuations ascribed to shear layer flapping, which involves low frequency oscillations of the separated shear layer, e.g., [137].

The first four POD modes of the in-plane velocity vector $((u', v'))$ from the top view 2C measurements form two mode pairs that contain substantially higher modal energy content than higher modes (Fig. 5.16). The chordwise component of the first ($\mathbf{\Phi}^{(1)}$) and third ($\mathbf{\Phi}^{(3)}$) spatial modes are presented in Fig. 5.19, with the paired modes 2 and 3 not shown for brevity. The results indicate that the first mode pair is associated with the shear layer vortices, with the characteristic streamwise wavelength matching that seen in the side view 3C mode projections of Fig. 5.18. In the inboard region, the spatial mode shapes of mode 1 reflect strong two-dimensionality of the roll-up vortices. This is followed by

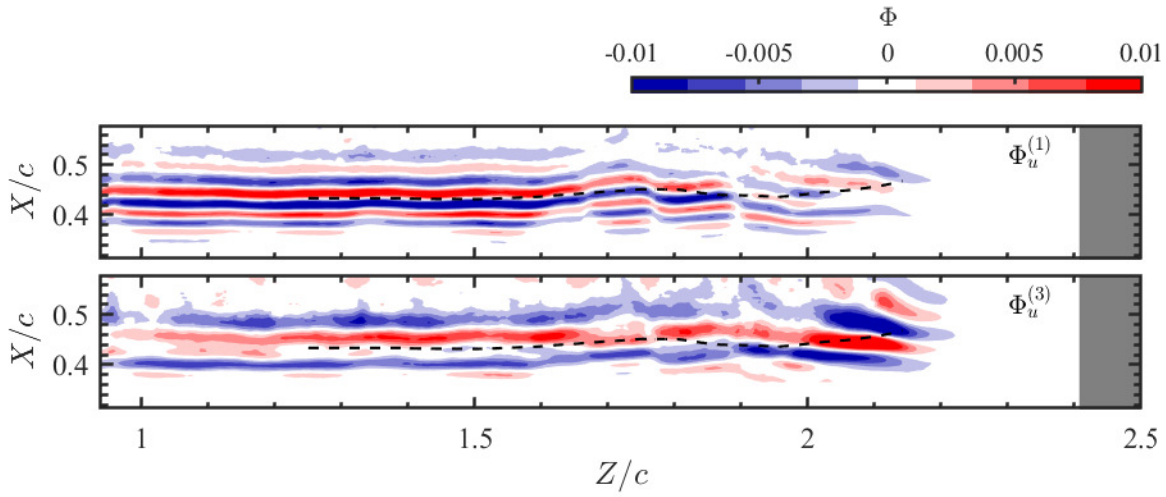

Figure 5.19: u component of spatial POD modes of (u', w') from top view 2C PIV. Dashed line: reattachment line from Fig. 5.2b.

progressive spanwise deformations for $z/c > 1.7$, with the shapes of the initial spanwise deformations following that of the mean reattachment line (dashed line). The contours of mode 3 indicate that the second mode pair is associated with velocity fluctuations at twice the fundamental wavelength, i.e., at the subharmonic of the shedding frequency. The relative magnitude of the modal energy increases notably for $z/c > 2.00$, suggesting that the increased growth of the subharmonic mode is a result of wingtip effects. This is supported by a gradual increase in the mean streamwise wavelength in the same spanwise region seen in Fig. 5.14e. The amplification of disturbances at the subharmonic of the fundamental shear layer frequency has been associated with vortex merging in experiments on LSBs on two-dimensional airfoils, e.g., [11, 60]. The merging of vortices in LSBs is often a localised phenomenon along the span, and has been speculated to be linked to cycle-to-cycle variations in the vortex strength or spacing in nominally two-dimensional LSBs [60]. This is consistent with the increased vortex deformations seen near the wingtip, which can promote localised vortex merging.

For a more detailed statistical comparison of the wavelengths of shear layer disturbances in the LSB, the spatial power spectral density of the wall-normal component of velocity fluctuations ($\mathcal{F}_{v'v'}$) was calculated for each instantaneous velocity field from the side view 3C configuration. The data were sampled along $y = \delta_x^*$, over the streamwise extent of the field of view. The resulting spectra of streamwise wavelength (λ) were then averaged over all instantaneous velocity fields at each measurement plane, and the results are presented in Fig. 5.20. In Fig. 5.20a, all spectra have been normalised by total energy and stepped by an order of magnitude to facilitate the identification of the dominant spectral peaks, while the comparison of the spectral energy content is facilitated by Fig. 5.20b. In the inboard and intermediate regions $1.25 \leq z/c < 2.25$, the results reveal clear spectral peaks within $0.037 \leq \lambda/c \leq 0.043$, which correspond to the streamwise vortex wavelength estimates based on the vortex core detection in Fig. 5.14e. The associated spectral energy contours

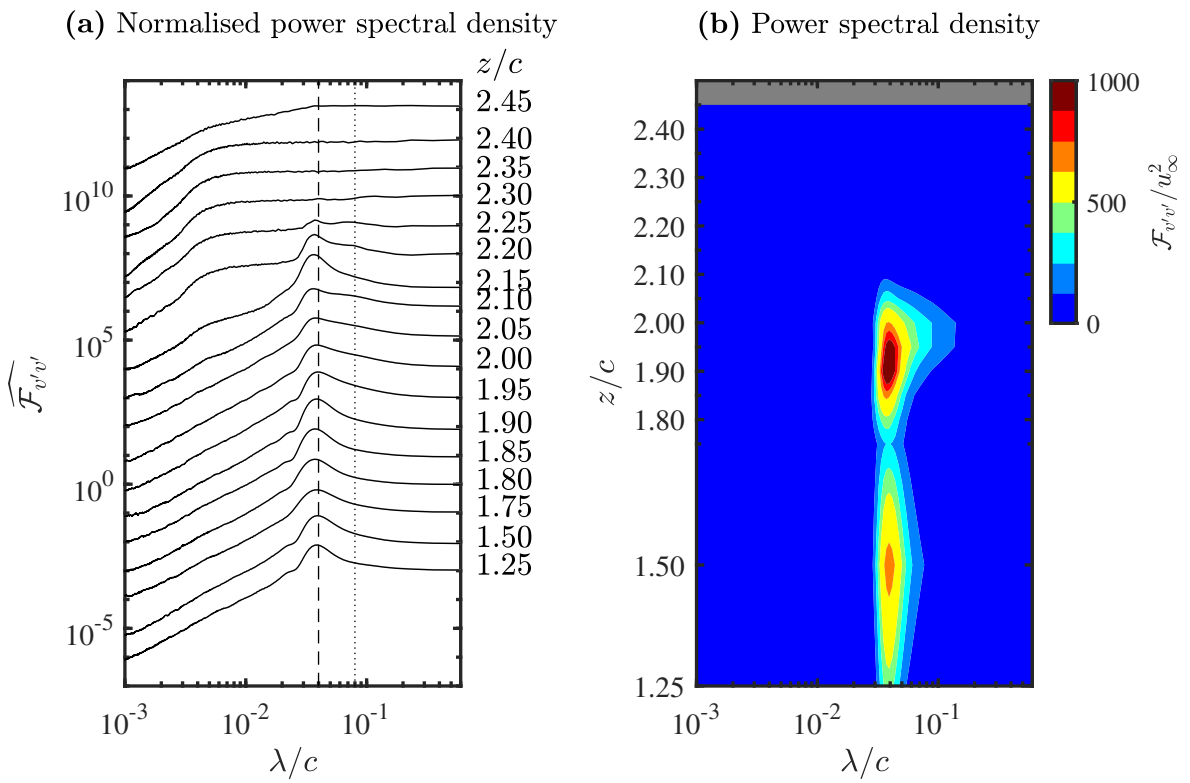

Figure 5.20: Streamwise wavelength spectra from side view 3C PIV at $y = \delta_x^*$. Dashed line: $\lambda/c = 0.04$; dotted line: $\lambda/c = 0.08$. Each spectrum in **(a)** is shifted by an order of magnitude at consecutive z/c locations for clarity.

in Fig. 5.20b show maximum energy content reached inside the inboard and intermediate regions, while a notable decrease in the peak energy is seen at the boundaries of the intermediate region. The results also show a relative increase in the spectral energy of the subharmonic mode for $2.05 \leq z/c \leq 2.25$, agreeing with the increase in the energy content of the subharmonic POD mode (Fig. 5.19), at the outboard end of the intermediate region. However, the energy content associated with these fluctuations is relatively low, as can be seen in Fig. 5.17, and thus the overall impact on the LSB topology is not expected to be significant. As discussed earlier, the delayed and eventually suppressed separation and the associated reduction in the growth rates of disturbances delay transition near the wingtip, producing insignificant spectral content in the tip region in Fig. 5.20.

The spanwise variation of the fundamental wavelength (λ_0) from the spectral analysis is presented in Fig. 5.21a, along with the mean streamwise velocity at the location of maximum shape factor ($x = x_H$, $y = \delta_x^*$) which approximates the average convection velocity of shear layer vortices [9] at a given z plane. The estimates are then used to obtain the shedding Strouhal number ($St_0 = f_0 c/u_\infty$, where $f_0 \approx \overline{u}/\lambda_0$) which is presented in Fig. 5.21b. The results confirm that the dominant streamwise wavelength of the vortices does not change appreciably across the span of the wing, despite notable changes to the mean bubble topology and vortex dynamics in the proximity of the wingtip. The associated

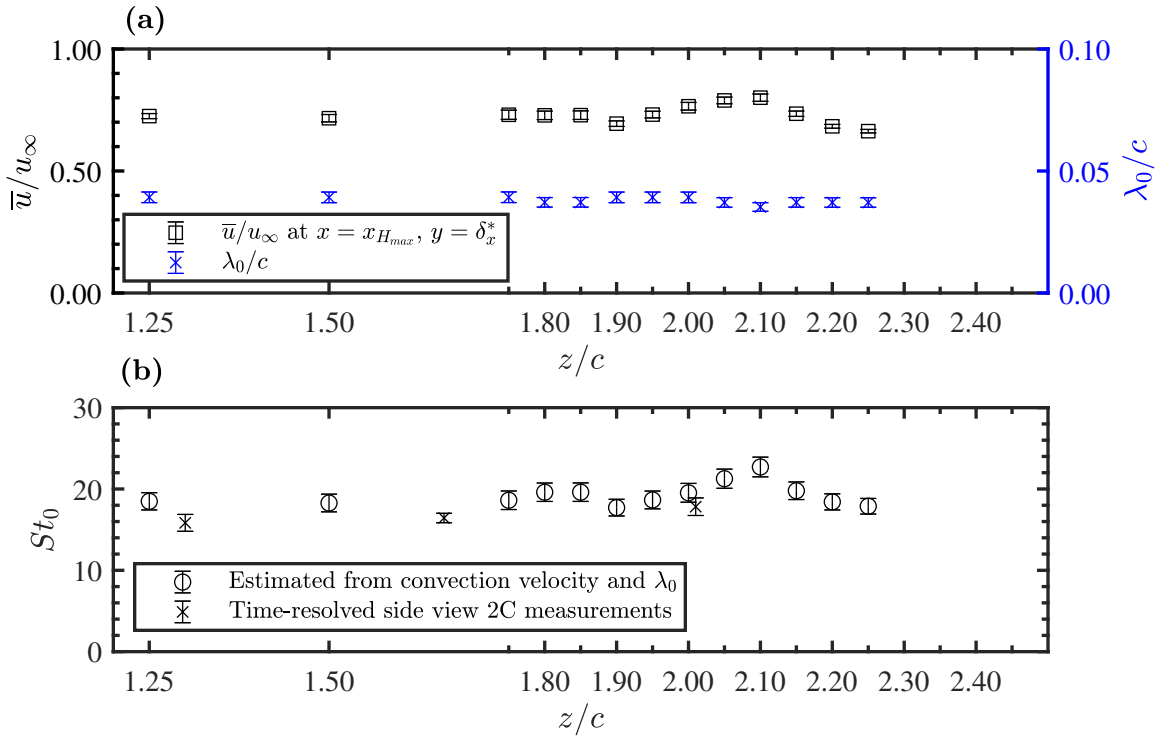

Figure 5.21: **(a)** Convection velocity and fundamental wavelength. **(b)** Estimated fundamental vortex shedding frequency.

shedding frequency shows minor variations across the span driven largely by the variations in the convection velocity estimates. The shedding frequency estimates agree to within the experimental uncertainty with the direct estimates from time-resolved measurements from the side view 2C configuration presented in Section 4.4.

It is important to note that, based on measurements of two-dimensional LSBs on the same airfoil profile, a change in the effective angle of attack from about 5° at $z/c = 1.25$ to 3° at $z/c = 2.15$ would result in a decrease in St_0 of about 20% in a two-dimensional LSB [14]. In contrast, the variation of St_0 seen in Fig. 5.21 is non-monotonic and is confined primarily to within about 10% of the inboard value largely due to experimental uncertainty. Thus, it can be concluded that shear layer transition within an LSB formed on a finite wing locks onto a common unstable mode across the span, with relatively small variations in vortex dynamics compared to those expected due to the change in the effective angle of attack across the span. This also explains the relative spanwise uniformity in the bubble topology, with the exception of progressive changes seen within the intermediate region and in the proximity of the tip, where open separation takes place due to the effects of the wingtip vortex.

5.4 Discussion

The results of this investigation demonstrate that significant changes to the LSB topology and dynamics take place in the relative proximity of the wingtip, eventually leading to open separation and effective termination of LSB. Although no comparable LSB flowfield measurements are available on finite wings, it is of interest to explore the generality of the observed trends across a wider parameter space, including other profiles, aspect ratios, Reynolds numbers, and angles of attack. This is facilitated by Table 5.1, which presents a summary of previous studies where LSB development on finite wings has been considered using surface flow visualization and/or surface pressure measurements. The results of these studies suggest that the most predominant changes in the bubble footprint along the span are confined to a region of approximately one chord length from the wingtip across a range of different experimental conditions and geometries.

A more detailed comparison of the results from previous studies is facilitated in Figs. 5.22a and 5.22b, which include data from investigations where mean separation and reattachment lines could be extracted without significant ambiguities. Figure 5.22 provides a comparison of separation and reattachment lines (Fig. 5.22a) and separation bubble length (Fig. 5.22b) at similar angles of attack. Because of the different aspect ratios employed, data are presented in terms of distance from the wingtip ($z_{tip} - z$). It is important to note that the behaviour of separation and reattachment lines is extracted from surface visualisations and hence should be interpreted with caution near the wingtip. Specifically, the region of highly three-dimensional flow near the wingtip produces complex surface flow patterns that do not necessarily yield well-defined separation lines (e.g., Fig. 5.2b), making interpretation of oil flow visualisations difficult. Additionally, the wingtip vortex creates its own separation and reattachment lines, e.g., [140], which may be difficult to distinguish from those attributable to the LSB. Nonetheless, similar to the present study, a consistent downstream shift in reattachment near the wingtip is observed in Fig. 5.22a, and substantial changes in flow topology and separation bubble length are confined within approximately one chord length of the wingtip, in agreement with the general observations made in Table 5.1. All identified separation lines extend closer to the wingtip than the corresponding reattachment lines, which is expected given the strengthening of the wingtip vortex with increasing x/c, e.g., [141]. Further, while different trends are seen in the separation line estimates near the tip due to the aforementioned challenges in reliable separation identification, on the average, the results suggest a delayed reattachment and enlargement of the LSB. Finally, termination of the reattachment lines prior to the wingtip points to the open nature of the LSBs in the tip region. Thus, the comparison of the results indicates that similar three-dimensional LSB structure and dynamics to those observed in the present study are expected to occur on finite wings of various geometric and flow parameters for the aspect ratios sufficiently large to ensure that the flow across the entire wing is not comprised entirely by end-effect dominated regions ($sAR \gtrsim 2$).

For a given airfoil profile, both the angle of attack and chord Reynolds number are known to influence the size and position of LSBs, with the former parameter associated with a more significant effect, e.g., [14]. Since the strength of the wingtip vortex also shows

Table 5.1: Comparison of selected previous studies involving LSBs on finite wings. Specified parameter ranges apply to pre-stall conditions where LSBs were explicitly detected in the corresponding studies.

Study	Airfoil Geometry	sAR	α	Re_c	Distance from wingtip within which notable LSB changes occur
Present investigation	NACA 0018	2.5	6°	1.25×10^5	$0.5c$
Huang & Lin [91]	NACA 0012	5	5° —12.5°	8.0×10^4	$0.5c$ —$1c$
Yen & Huang [133]	NACA 0012	5	6° —11°	4.6×10^4	$0.5c$ —$1c$
Marchman & Abtahi [89]	Wortmann FX 63-137	4	low, moderate*	7.0×10^4 — 3.0×10^5	$0.5c$ —$1c$
Bastedo & Mueller [23]	Wortmann FX 63-137	2	17°	8.0×10^4, 2.0×10^5	$0.2c$ —$0.4c$
Ananda *et al.* [134]	Wortmann FX 63-137	2	−2° —14°	9.0×10^4	$0.5c$ —$1c$

*Two unspecified pre-stall angles presented by the authors.

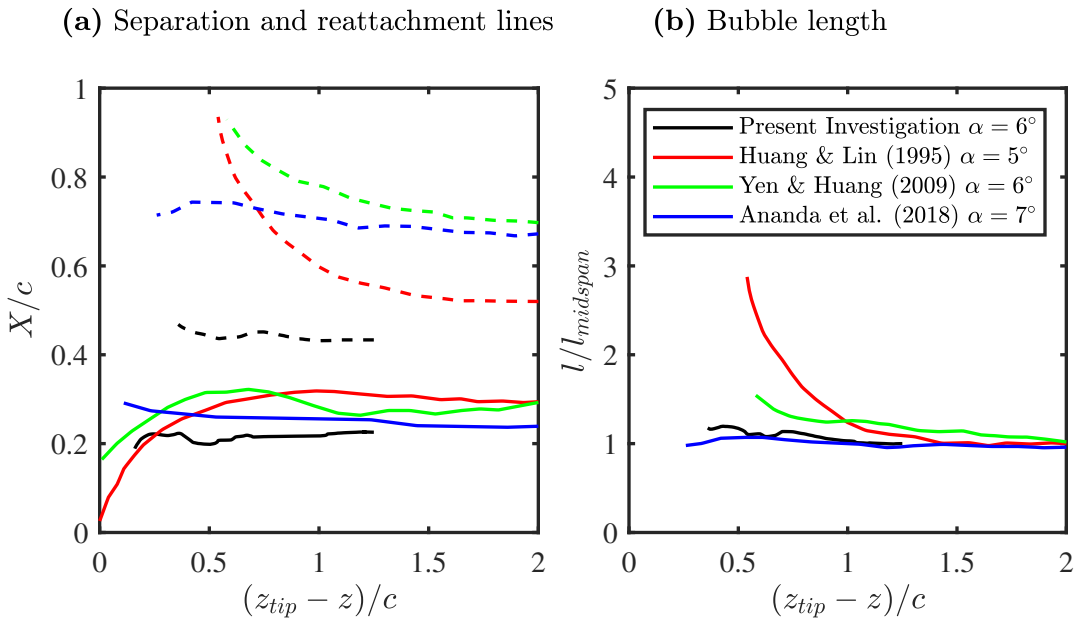

Figure 5.22: Separation line, reattachment line, and bubble length comparison with selected previous studies. Solid and dashed lines in **(a)** are separation and reattachment lines, respectively.

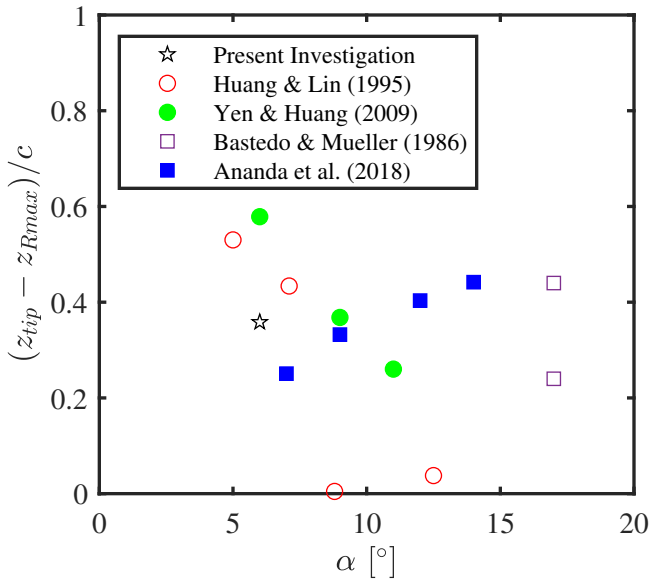

Figure 5.23: Distance between wingtip and estimated end of reattachment line. Experimental data on wings with the same airfoil profile are marked by the same symbol shapes.

a notable dependence on the angle of attack, e.g., [141], changes in this parameter may be expected to lead to substantial changes in the extent of the region where LSB development is critically altered near the wingtip. To assess the spanwise extent of this region at varying angles of attack, Fig. 5.23 presents the distance between the wingtip (z_{tip}) and the end of the LSB reattachment line (z_{Rmax}) extracted from the present and previous studies. The two studies with a NACA 0012 airfoil profile (Huang & Lin [91] and Yen & Huang [133]) suggest a decrease in the spanwise extent of the three-dimensional tip flow with increasing angle of attack. In contrast, on the average, the Wortmann profile used by Ananda *et al.* [134] and Bastedo & Mueller [23] displays an increase in the affected reattachment zone with increasing angle of attack. In addition to the aforementioned difficulties associated with the interpretation of the surface visualizations in the tip region, the observed discrepancy may be attributed to opposing effects of the angle of attack on the wingtip vortex and LSB. While an increase in the angle of attack increases the strength of the wingtip vortex and hence the spanwise extent of its effect on the suction side, it also moves the LSB upstream and reduces its length. Due to the decrease in the strength of the tip vortex towards the leading edge, the upstream movement of the LSB produces an opposing effect to the expected degree of spanwise influence. Consequently, since the LSB characteristics strongly depend on the profile shape, different and non-monotonic trends may be observed on different geometries, as seen in Fig. 5.23. However, for the variety of cases presented, the reattachment line ends no more than $0.6c$ from the wingtip, providing an approximate estimate of the maximum extent of the near-tip region where LSB suppression is expected to occur. Finally, a mild upstream movement of the reattachment point and shrinking of the LSB length with increasing chord Reynolds number, driven by the advancing transition, is expected to reduce the extent of the three-dimensional changes in LSBs on wings of a given geometry. This is reflected in the observations from Bastedo & Mueller [23], whose

two data points in Fig. 5.23 show a reduction in $z_{tip} - z_{Rmax}$ from about $0.4c$ to $0.2c$ for $Re_c = 8.0 \times 10^4$ and 2.0×10^5, respectively.

Chapter 6

Conclusions & Recommendations

6.1 Conclusions

In this thesis, a three-dimensional laminar separation bubble was studied on a rectangular NACA 0018 wing with a semi-aspect ratio of 2.5, at an angle of attack of 6°, and a Reynolds number of 1.25×10^5. Surface pressure measurements and particle image velocimetry were used to investigate the structure and dynamics of the LSB on the suction surface of the wing.

The first objective of this thesis was to determine the extent to which the presence of the wingtip causes the LSB on the finite wing to differ from an LSB on a two-dimensional airfoil. This objective was pursued through a comparison of the finite wing and two-dimensional airfoil model configurations at various geometric and effective angles of attack. Relative to the airfoil at the same geometric angle of attack, the adverse pressure gradient on the finite wing was reduced, causing the LSB on the finite wing to lengthen and form farther downstream, consistent with a reduction in effective angle of attack on the finite wing. In the midspan region of the wing, the mean locations of separation, transition, and reattachment were remarkably similar to those of the LSB on the two-dimensional airfoil at the same effective angle of attack. The frequency band of amplified disturbances of the LSB on the wing and two-dimensional airfoil at the same effective angle of attack also showed no substantial differences, indicating that the stability characteristics and transition process of the two LSBs were essentially equivalent. These results provide validation for the use of two-dimensional airfoil data to approximate the sectional characteristics of finite wings at low Reynolds numbers away from the wingtips in the region where the effective angle of attack is nearly spanwise invariant. Whereas previous studies of LSBs on finite wings reported that the larger spanwise changes in effective angle of attack near the wingtips

produce corresponding changes in LSB location, such changes were not observed. Instead, the location and fundamental frequency of the LSB on the finite wing in this study remained invariant to spanwise changes in effective angle of attack up to approximately 0.5 chord lengths from the wingtip. Although LSB location and fundamental frequency did not appreciably change in the spanwise direction, substantial changes in LSB thickness, reverse flow velocity, and spanwise flow were observed at the outboard end of the LSB on the wing.

The second objective of this thesis was to determine the topological structure of a three-dimensional LSB on a finite wing. In the midspan region of the wing, the LSB largely conforms to the canonical two-dimensional mean LSB topology. However, near the wingtip, the two-dimensional description can no longer be applied because the three-dimensional separation bubble evolves into an open bubble that exchanges fluid with the surrounding flow. Also incompatible with the canonical two-dimensional LSB topology is the reattachment of the separated shear layer in the portion of the LSB where roll-up vortices do not form. Here, the separated shear layer curves back towards the wing surface not because of transition to turbulence but because of the reduction in adverse pressure gradient and downwash caused by the wingtip vortex. Under the conditions considered in this investigation, the LSB on the wing is classified as a crossflow separation, since the three-dimensional separation line does not originate at a saddle point of the limiting streamline field, but instead forms from the gradual convergence of ordinary limiting streamlines. Fluid enters the three-dimensional open recirculation region of the LSB at the wingtip, and is drawn inboard by the spanwise pressure gradient on the wing. This influx of fluid is related to a localised thickening of the LSB, characterised by an increase in height of the recirculation region and increase in displacement thickness. Fluid begins to exit from the LSB in the region where the LSB's thickness is largest. As a result of the outflow of fluid from the LSB, spanwise velocities within the LSB are reduced near the midspan, and the LSB approaches the canonical two-dimensional topology farther from the wingtip.

The third objective of this thesis was to investigate the influence of the three-dimensional wingtip flow on the transition process in the LSB. In agreement with previous studies, downwash from the wingtip vortex prevents boundary layer separation from occuring in the tip region within 0.3 chord lengths of the wingtip. In this region, boundary layer transition is not observed. Further away from the wingtip, the adverse pressure gradient on the suction surface is sufficiently strong to cause boundary layer separation and LSB formation. At the outboard end of the LSB, disturbance growth rates and amplitudes in the separated shear layer are substantially reduced, which is attributed to the weaker adverse pressure gradient relative to locations farther inboard. The increased stability of the outboard portion of the separated shear layer delays the formation and reduces the strength of shear layer vortices, causing a delay in transition. In the midspan region, the amplification of disturbances in the separated shear layer is stronger, and causes the formation of spanwise roll-up vortices similar to those found in two-dimensional LSBs at low turbulence intensities. Although the roll-up vortices away from the wingtip are essentially uniform in the spanwise direction, more pronounced vortex deformations are observed at the outboard end of the LSB, where an increase in energy content of the subharmonic mode suggests that vortex merging is promoted. While changes to LSB dynamics are most notable in the intermediate region

between the midspan region and the tip region, the transition process in the midspan region of the wing was not appreciably influenced by three-dimensional effects, and the fundamental vortex shedding frequency and wavelength are nearly constant along the entire portion of the wing where shear layer roll-up occurs.

This investigation confirms the assumption of previous studies that LSBs forming on finite wings at low chord Reynolds numbers can be described using two-dimensional LSB characteristics, but shows that the analogy between two- and three-dimensional LSB properties is limited to the region more than ≈ 1 chord length away from the wingtips. Close to the wingtips, where LSB structure and dynamics vary substantially in the spanwise direction, the two-dimensional analogy is inadequate and three-dimensional tip effects must be considered.

6.2 Recommendations

The conclusions of this thesis lead to the following recommendations:

1. In this investigation, a three-dimensional LSB was studied at a single angle of attack and Reynolds number. In Section 5.4 it is conjectured that the three-dimensional LSB topology observed in the present investigation is representative of LSBs forming on finite wings across a range of different geometries and experimental conditions. However, since topological bifurcations of the LSB structure may occur due to changes in angle of attack or Reynolds number, it is recommended that future studies be conducted to determine how the three-dimensional LSB structure varies with changes in angle of attack, wing geometry, and Reynolds number.

2. Across the portion of the span where shear layer roll-up was observed, variations in the fundamental vortex shedding frequency and wavelength remained largely constant, despite spanwise variations in the mean LSB topology that would be expected to cause local changes in the stability characteristics of the separated shear layer. This suggests that shear layer roll-up in the LSB on the finite wing is driven by an unstable global mode. Global stability analysis should be conducted to explore the spatial and temporal characteristics of unstable three-dimensional disturbance modes, and explore how these modes may be influenced by changes in experimental conditions.

3. Performance analysis of three-dimensional lifting surfaces is often based on the assumption that at any given spanwise position, the flow can be treated as two-dimensional. Lifting line theory and blade element momentum theory are two such analysis methods commonly used in the design of wings and turbine blades. These methods assume that the effective angle of attack can be used to determine local lift and drag coefficients from two-dimensional airfoil data. Prediction of overall lifting surface performance parameters such as lift and drag at low chord Reynolds numbers using these types of methods should be performed with caution, since the LSB in this study did not respond to spanwise changes in effective angle of attack.

4. LSBs on finite wings have been associated with nonlinear and often abrupt changes in lift and drag forces, e.g., [23, 92, 133]. To understand the flow phenomena responsible for these nonlinearities, and to address the shortcomings of two-dimensional performance analysis methods for three-dimensional lifting surfaces, future investigations using simultaneous velocity field and direct force measurements should be conducted to explore the physical mechanisms responsible for the lift and drag characteristics of finite wings at low chord Reynolds numbers.

5. This investigation focused only on the wingtip. Future studies should be conducted to investigate the three-dimensional interaction of the LSB and the wing root flow, which is also a fundamental part of practical finite wing flows. The control volume analysis performed in Section 5.1 should be extended across the entire wingspan, including the wing root region, to fully characterise the mass flow within the LSB.

6. The similarity of the transition process on the wing to the two-dimensional airfoil suggests that effective flow control techniques for two-dimensional LSBs may also be applicable to the flow over finite wings. Future experiments should be performed to determine how the performance losses associated with LSBs on finite wings can be mitigated using active and passive control methods.

7. The side view 3C PIV measurement planes in this study had a relatively coarse spacing in the spanwise direction, which limited the resolution of spanwise gradients in the flow. To resolve these gradients and coherent structures with greater precision, it is recommended that PIV measurements be performed with finer spanwise resolution, ideally less than the fundamental vortex shedding wavelength. This could be achieved either with finer spacing between measurement planes or through the use of tomographic PIV. Tomographic PIV has the additional advantage that velocity data can be obtained simultaneously throughout the entire measurement volume, enabling the instantaneous observation of three-dimensional coherent structures, which is not possible when obtaining volumetric measurements by traversing a single plane PIV configuration in the spanwise direction.

References

[1] Toppings, C. E., Kurelek, J. W., & Yarusevych, S. 2021 Laminar Separation Bubble Development on a Finite Wing. *AIAA Journal* (Articles in Advance), 1–13. DOI. ↩

[2] Carmichael, B. H. 1981 Low Reynolds Number Airfoil Survey. *Tech. rep.* NASA CR-165803, Low Energy Transportation Systems, Capistrano Beach, CA. ↩

[3] Gudmundsson, S. 2014 The Anatomy of the Wing. In *General Aviation Aircraft Design*, part 9, pp. 299–399. Elsevier. DOI. ↩

[4] Lissaman, P. B. S. 1983 Low-Reynolds-Number Airfoils. *Annual Review of Fluid Mechanics* **15** (1), 223–239. DOI. ↩

[5] Schlichting, H. & Gersten, K. 2017 *Boundary-Layer Theory*. 9th ed. Springer Berlin Heidelberg. DOI. ↩

[6] McMasters, J. H. & Henderson, M. L. 1980 Low-Speed Single-Element Airfoil Synthesis. *Technical Soaring* **6** (2), 1–21. ↩

[7] Horton, H. P. 1968 *Laminar Separation Bubbles in Two and Three Dimensional Incompressible Flow*. Ph.D. Thesis, University of London, London. ↩

[8] Diwan, S. S. & Ramesh, O. N. 2009 On the origin of the inflectional instability of a laminar separation bubble. *Journal of Fluid Mechanics* **629**, 263–298. DOI. ↩

[9] Boutilier, M. S. H. & Yarusevych, S. 2012 Separated shear layer transition over an airfoil at a low Reynolds number. *Physics of Fluids* **24** (8), 084105. DOI. ↩

[10] Tani, I. 1964 Low-speed flows involving bubble separations. *Progress in Aerospace Sciences* **5**, 70–103. DOI. ↩

[11] Yarusevych, S., Sullivan, P. E., & Kawall, J. G. 2009 On vortex shedding from an airfoil in low-Reynolds-number flows. *Journal of Fluid Mechanics* **632**, 245–271. DOI. ↩

[12] Gaster, M. 1967 The Structure and Behaviour of Laminar Separation Bubbles. *Tech. rep.* Aeronautical Research Council Reports and Memoranda 3595, London, pp. 1–33. ↩

[13] O'Meara, M. M. & Mueller, T. J. 1987 Laminar separation bubble characteristics on an airfoil at low Reynolds numbers. *AIAA Journal* **25** (8), 1033–1041. DOI. ↩

[14] Boutilier, M. S. H. & Yarusevych, S. 2012 Parametric study of separation and transition characteristics over an airfoil at low Reynolds numbers. *Experiments in Fluids* **52** (6), 1491–1506. DOI. ↩

[15] Mueller, T. J. 1999 Aerodynamic Measurements at Low Reynolds Numbers for Fixed Wing Micro-Air Vehicles. In *RTO AVT Special Course on Development and Operation of UAVs for Military and Civil Applications*, number 8, pp. 1–32, Rhode-Saint-Genèse, Belgium. ↩

[16] Hansen, A. C. & Butterfield, C. P. 1993 Aerodynamics of Horizontal-Axis Wind Turbines. *Annual Review of Fluid Mechanics* **25** (1), 115–149. DOI. ↩

[17] Hodson, H. P. & Howell, R. J. 2005 The Role of Transition in High-Lift Low-Pressure Turbines for Aeroengines. *Progress in Aerospace Sciences* **41** (6), 419–454. DOI. ↩

[18] Schewe, G. 1983 On the force fluctuations acting on a circular cylinder in crossflow from subcritical up to transcritical Reynolds numbers. *Journal of Fluid Mechanics* **133**, 265–285. DOI. ↩

[19] Green, S. I. 1995 Wing Tip Vortices. In *Fluid Vortices. Fluid Mechanics and Its Applications*, pp. 427–469. DOI. ↩

[20] Prandtl, L. 1922 Applications of Modern Hydrodynamics to Aeronautics. *Tech. rep.* NACA TR-116, pp. 159–215. ↩

[21] Torres, G. E. 2002 *Aerodynamics of Low Aspect Ratio Wings at Low Reynolds Numbers With Applications to Micro Air Vehicle Design*. PhD Thesis, University of Notre Dame. ↩

[22] Awasthi, M., Moreau, D., & Doolan, C. 2018 Flow structure of a low aspect ratio wall-mounted airfoil operating in a low Reynolds number flow. *Experimental Thermal and Fluid Science* **99**, 94–116. DOI. ↩

[23] Bastedo, W. G. & Mueller, T. J. 1986 Spanwise variation of laminar separation bubbles on wings at low Reynolds number. *Journal of Aircraft* **23** (9), 687–694. DOI. ↩

[24] Pauley, L. L., Moin, P., & Reynolds, W. C. 1990 The structure of two-dimensional separation. *Journal of Fluid Mechanics* **220**, 397–411. DOI. ↩

[25] Burgmann, S., Dannemann, J., & Schröder, W. 2008 Time-resolved and volumetric PIV measurements of a transitional separation bubble on an SD7003 airfoil. *Experiments in Fluids* **44** (4), 609–622. DOI. ↩

[26] Marxen, O., Lang, M., & Rist, U. 2013 Vortex formation and vortex breakup in a laminar separation bubble. *Journal of Fluid Mechanics* **728**, 58–90. DOI. ↩

[27] Istvan, M. S. & Yarusevych, S. 2018 Effects of free-stream turbulence intensity on transition in a laminar separation bubble formed over an airfoil. *Experiments in Fluids* **59** (3), 52. DOI. ↩

[28] Chen, P.-W., Bai, C.-J., & Wang, W.-C. 2016 Experimental and numerical studies of low aspect ratio wing at critical Reynolds number. *European Journal of Mechanics - B/Fluids* **59**, 161–168. DOI. ↩

[29] Torres, G. E. & Mueller, T. J. 2004 Low Aspect Ratio Aerodynamics at Low Reynolds Numbers. *AIAA Journal* **42** (5), 865–873. DOI. ↩

[30] Kremheller, A. & Fasel, H. 2010 Water Tunnel Experiments on Three Dimensional Separation Bubbles on a Flat Plate. In *40th Fluid Dynamics Conference and Exhibit*, Reston, Virigina. American Institute of Aeronautics and Astronautics. DOI. ↩

[31] Jones, B. M. 1933 An Experimental Study of the Stalling of Wings. *Tech. rep.* Aeronautical Research Comittee R&M 1588, p. 99. ↩

[32] McCullough, G. B. & Gault, D. E. 1951 Examples of Three Representative Types of Airfoil-Section Stall at Low Speed. *Tech. rep.* NACA TN-2502. DOI. ↩

[33] Mueller, T. J. 1985 The influence of laminar separation and transition on low Reynolds number airfoil hysteresis. *Journal of Aircraft* **22** (9), 763–770. DOI. ↩

[34] Marchman, J. F. 1987 Aerodynamic testing at low Reynolds numbers. *Journal of Aircraft* **24** (2), 107–114. DOI. ↩

[35] Dovgal, A., Kozlov, V., & Michalke, A. 1994 Laminar boundary layer separation: Instability and associated phenomena. *Progress in Aerospace Sciences* **30** (1), 61–94. DOI. ↩

[36] Brendel, M. & Mueller, T. J. 1988 Boundary layer measurements on an airfoil at a low Reynolds number in an oscillating freestream. *AIAA Journal* **26** (3), 257–263. DOI. ↩

[37] Watmuff, J. H. 1999 Evolution of a wave packet into vortex loops in a laminar separation bubble. *Journal of Fluid Mechanics* **397**, 119–169. DOI. ↩

[38] Millikan, C. B. & Klein, A. L. 1933 The Effect of Turbulence: An Investigation of Maximum Lift Coefficient and Turbulence in Wind Tunnels and in Flight. *Aircraft Engineering* **5** (8), 169–174. ↩

[39] Hosseinverdi, S. & Fasel, H. F. 2019 Numerical investigation of laminar–turbulent transition in laminar separation bubbles: the effect of free-stream turbulence. *Journal of Fluid Mechanics* **858**, 714–759. DOI. ↩

[40] Michelis, T., Yarusevych, S., & Kotsonis, M. 2018 On the origin of spanwise vortex deformations in laminar separation bubbles. *Journal of Fluid Mechanics* **841**, 81–108. DOI. ↩

[41] Saric, W. S., Reed, H. L., & Kerschen, E. J. 2002 Boundary Layer Receptivity to Freestream Disturbances. *Annual Review of Fluid Mechanics* **34** (1), 291–319. DOI. ↩

[42] Mack, L. 1984 Boundary-Layer Linear Stability Theory. *Tech. rep.* AGARD 709, Neuilly-sur-Seine. ↩

[43] Orr, W. M. 1907 The Stability or Instability of the Steady Motions of a Liquid. *Proceedings of the Royal Irish Academy, Section A: Mathematical and Physical Sciences* **27**, 69–138. ↩

[44] Sommerfeld, A. 1908 Ein Beitrag zur Hydrodynamischen Erklärung der Turbulenten Flüssigkeitsbewegungen. *Atti del IV Congresso Internazionale dei Matematici* ↩

[45] Tollmien, W. 1930 Über die Entstehung der Turbulenz. In Gilles, A., Hopf, L., & Von Kármán, T., editors, *Vorträge aus dem Gebiete der Aerodynamik und verwandter Gebiete*. Springer. ↩

[46] Schlichting, H. 1933 Zur Enstehung der Turbulenz bei der Plattenströmung. *Nachrichten von der Gesellschaft der Wissenschaften zu Göttingen, Mathematisch-Physikalische Klasse 1933* 181–208. ↩

[47] Schubauer, G. B. & Skramstad, H. K. 1947 Laminar Boundary-Layer Oscillations and Stability of Laminar Flow. *Journal of the Aeronautical Sciences* **14** (2), 69–78. DOI. ↩

[48] Lord Rayleigh. 1879 On the Stability, or Instability, of certain Fluid Motions. *Proceedings of the London Mathematical Society* **s1-11** (1), 57–72. DOI. ↩

[49] Fjørtoft, R. 1950 Application of Integral Theorems in Deriving Criteria of Stability for Laminar Flows and for the Baroclinic Circular Vortex. *Geophysical Publications* **17** (6), 1–52. ↩

[50] Ho, C.-M. & Huerre, P. 1984 Perturbed Free Shear Layers. *Annual Review of Fluid Mechanics* **16** (1), 365–422. DOI. ↩

[51] Boutilier, M. S. H. & Yarusevych, S. 2012 Effects of End Plates and Blockage on Low-Reynolds-Number Flows Over Airfoils. *AIAA Journal* **50** (7), 1547–1559. DOI. ↩

[52] Michalke, A. 1991 On the Instability of Wall-Boundary Layers Close to Separation. In Kozlov, V. & Dovgal, A., editors, *Separated Flows and Jets*, pp. 557–564. Springer Berlin Heidelberg. DOI. ↩

[53] Rist, U., Maucher, U., & Wagner, S. 1996 Direct Numerical Simulation of Some Fundamental Problems Related to Transition in Laminar Separation Bubbles. In *Computational Fluid Dynamics '96*, pp. 319–325. Wiley. ↩

[54] Alam, M. & Sandham, N. D. 2000 Direct numerical simulation of 'short' laminar separation bubbles with turbulent reattachment. *Journal of Fluid Mechanics* **403**, 223–250. DOI. ↩

[55] Marxen, O., Lang, M., & Rist, U. 2012 Discrete linear local eigenmodes in a separating laminar boundary layer. *Journal of Fluid Mechanics* **711**, 1–26. DOI. ↩

[56] Kurelek, J. W., Lambert, A. R., & Yarusevych, S. 2016 Coherent Structures in the Transition Process of a Laminar Separation Bubble. *AIAA Journal* **54** (8), 2295–2309. DOI. ↩

[57] Kirk, T. M. & Yarusevych, S. 2017 Vortex shedding within laminar separation bubbles forming over an airfoil. *Experiments in Fluids* **58** (5), 43. DOI. ↩

[58] Simoni, D., Lengani, D., Ubaldi, M., Zunino, P., & Dellacasagrande, M. 2017 Inspection of the dynamic properties of laminar separation bubbles: free-stream turbulence intensity effects for different Reynolds numbers. *Experiments in Fluids* **58** (6), 66. DOI. ↩

[59] Lambert, A. & Yarusevych, S. 2019 Effect of angle of attack on vortex dynamics in laminar separation bubbles. *Physics of Fluids* **31** (6), 064105. DOI. ↩

[60] Kurelek, J. W., Yarusevych, S., & Kotsonis, M. 2019 Vortex merging in a laminar separation bubble under natural and forced conditions. *Physical Review Fluids* **4** (6), 063903. DOI. ↩

[61] Marxen, O., Lang, M., Rist, U., Levin, O., & Henningson, D. S. 2009 Mechanisms for spatial steady three-dimensional disturbance growth in a non-parallel and separating boundary layer. *Journal of Fluid Mechanics* **634**, 165. DOI. ↩

[62] Floryan, J. 1991 On the görtler instability of boundary layers. *Progress in Aerospace Sciences* **28** (3), 235–271. DOI. ↩

[63] Rodríguez, D. & Theofilis, V. 2010 Structural changes of laminar separation bubbles induced by global linear instability. *Journal of Fluid Mechanics* **655**, 280–305. DOI. ↩

[64] Rodríguez, D., Gennaro, E. M., & Juniper, M. P. 2013 The Two Classes of Primary Modal Instability in Laminar Separation Bubbles. *Journal of Fluid Mechanics* **734**, 1–11. DOI. ↩

[65] Prandtl, L. 1904 Über Flüssigkeitsbewegung bei sehr kleiner Reibung. In *Verhandlungen des III. Internationalen Mathematiker-Kongresses*, Heidelberg. ↩

[66] Tobak, M. & Peake, D. J. 1982 Topology of Three-Dimensional Separated Flows. *Annual Review of Fluid Mechanics* **14** (1), 61–85. DOI. ↩

[67] Délery, J. M. 2001 Robert Legendre and Henri Werlé: Toward the Elucidation of Three-Dimensional Separation. *Annual Review of Fluid Mechanics* **33** (1), 129–154. DOI. ↩

[68] Legendre, R. 1956 Separation de L'ecoulement Laminaire Tridimensionel. *La Recherche Aéronautique* **54**, 3–8. ↩

[69] Surana, A., Grunberg, O., & Haller, G. 2006 Exact theory of three-dimensional flow separation. Part 1. Steady separation. *Journal of Fluid Mechanics* **564**, 57. DOI. ↩

[70] Wang, K. C. 1970 Three-dimensional boundary layer near the plane of symmetry of a spheroid at incidence. *Journal of Fluid Mechanics* **43** (1), 187–209. DOI. ↩

[71] Wu, J. Z., Tramel, R. W., Zhu, F. L., & Yin, X. Y. 2000 A vorticity dynamics theory of three-dimensional flow separation. *Physics of Fluids* **12** (8), 1932–1954. DOI. ↩

[72] Yates, L. A. & Chapman, G. T. 1988 Numerical investigation of crossflow separation on a three-caliber tangent ogive cylinder. *AIAA Journal* **26** (10), 1223–1230. DOI. ↩

[73] Chapman, G. T. & Yates, L. A. 1991 Topology of Flow Separation on Three-Dimensional Bodies. *Applied Mechanics Reviews* **44** (7), 329–345. DOI. ↩

[74] Wetzel, T. G., Simpson, R. L., & Chesnakas, C. J. 1998 Measurement of Three-Dimensional Crossflow Separation. *AIAA Journal* **36** (4), 557–564. DOI. ↩

[75] Yates, L. A. 1986 *Numerical Investigation of Flow Separation on a Three-Caliber Tangent Ogive*. PhD thesis, University of Florida. ↩

[76] Miozzi, M., Capone, A., Costantini, M., Fratto, L., Klein, C., & Di Felice, F. 2019 Skin friction and coherent structures within a laminar separation bubble. *Experiments in Fluids* **60** (1), 13. DOI. ↩

[77] Theofilis, V. 2011 Global Linear Instability. *Annual Review of Fluid Mechanics* **43** (1), 319–352. DOI. ↩

[78] Visbal, M., Yilmaz, T. O., & Rockwell, D. 2013 Three-dimensional vortex formation on a heaving low-aspect-ratio wing: Computations and experiments. *Journal of Fluids and Structures* **38**, 58–76. DOI. ↩

[79] Zhang, K., Hayostek, S., Amitay, M., He, W., Theofilis, V., & Taira, K. 2020 On the formation of three-dimensional separated flows over wings under tip effects. *Journal of Fluid Mechanics* **895**, A9. DOI. ↩

[80] Mueller, T. J. & DeLaurier, J. D. 2003 Aerodynamics of Small Vehicles. *Annual Review of Fluid Mechanics* **35** (1), 89–111. DOI. ↩

[81] Clifton-Smith, M. J. 2009 Wind Turbine Blade Optimisation with Tip Loss Corrections. *Wind Engineering* **33** (5), 477–496. DOI. ↩

[82] Pelletier, A. & Mueller, T. J. 2000 Low Reynolds Number Aerodynamics of Low-Aspect-Ratio, Thin/Flat/Cambered-Plate Wings. *Journal of Aircraft* **37** (5), 825–832. DOI. ↩

[83] Kaushik, M. 2019 Finite Wing Theory. In *Theoretical and Experimental Aerodynamics*, pp. 145–168. Springer Singapore. DOI. ↩

[84] Lanchester, F. W. 1907 *Aerodynamics, constituting the first volume of a complete work on aerial flight*. Bradbury, Agnew, & Co. LD. ↩

[85] Helmholtz, H. 1867 On Integrals of the hydrodynamical equations, which express vortex-motion. *The London, Edinburgh, and Dublin Philosophical Magazine and Journal of Science* **33** (226), 485–512. DOI. ↩

[86] Von Kármán, T. 1957 Two-Dimensional Wing Theory (Wing of Infinite Span). In *Aerodynamics - Selected Topics in the Light of Their Historical Development*. Dover Publications. ISBN. ↩

[87] Bastedo, W. G. & Mueller, T. J. 1985 Performance of Finite Wings at Low Reynolds Numbers. In Mueller, T. J., editor, *Proceedings of the Conference on Low Reynolds Number Airfoil Aerodynamics UNDAS-CP-77B123*, pp. 195–205, Notre Dame. University of Notre Dame. ↩

[88] Ananda, G., Sukumar, P., & Selig, M. 2015 Measured aerodynamic characteristics of wings at low Reynolds numbers. *Aerospace Science and Technology* **42**, 392–406. DOI. ↩

[89] Marchman, J. F. & Abtahi, A. 1985 Aerodynamics of an aspect ratio 8 wing at low Reynolds numbers. *Journal of Aircraft* **22** (7), 628–634. DOI. ↩

[90] Laitone, E. V. 1997 Wind tunnel tests of wings at Reynolds numbers below 70 000. *Experiments in Fluids* **23** (5), 405–409. DOI. ↩

[91] Huang, R. F. & Lin, C. L. 1995 Vortex shedding and shear-layer instability of wing at low-Reynolds numbers. *AIAA Journal* **33** (8), 1398–1403. DOI. ↩

[92] Chen, Z. J., Qin, N., & Nowakowski, A. F. 2013 Three-Dimensional Laminar-Separation Bubble on a Cambered Thin Wing at Low Reynolds Numbers. *Journal of Aircraft* **50** (1), 152–163. DOI. ↩

[93] Genç, M. S., Özkan, G., Özden, M., Kiriş, M. S., & Yildiz, R. 2018 Interaction of tip vortex and laminar separation bubble over wings with different aspect ratios under low Reynolds numbers. *Proceedings of the Institution of Mechanical Engineers, Part C: Journal of Mechanical Engineering Science* **232** (22), 4019–4037. DOI. ↩

[94] Selig, M., Deters, R., & Wiliamson, G. 2011 Wind Tunnel Testing Airfoils at Low Reynolds Numbers. In *49th AIAA Aerospace Sciences Meeting including the New Horizons Forum and Aerospace Exposition*, number January, Reston, Virigina. American Institute of Aeronautics and Astronautics. DOI. ↩

[95] Smith, T. A. & Ventikos, Y. 2021 Wing-tip vortex dynamics at moderate Reynolds numbers. *Physics of Fluids* **33** (3), 035111. DOI. ↩

[96] Perry, A. E., Hornung, H., Perry, A. E., & Hornung, H. 1984 Some aspects of three-dimensional separation. II - Vortex skeletons. *Zeitschrift für Flugwissenschaften und Weltraumforschung* **8**, 155–160. ↩

[97] Liu, Y.-C. & Hsiao, F.-B. 2014 Experimental Investigation on Critical Reynolds Numbers Aerodynamic Properties of Low Aspect Ratios Wings. *Procedia Engineering* **79**, 76–85. DOI. ↩

[98] Gresham, N. T., Wang, Z., & Gursul, I. 2010 Low Reynolds number aerodynamics of free-to-roll low aspect ratio wings. *Experiments in Fluids* **49** (1), 11–25. DOI. ↩

[99] Gerakopulos, R. J. 2011 *Investigating flow over an airfoil at low Reynolds numbers using novel time-resolved surface pressure measurements*. Master Thesis, University of Waterloo. ↩

[100] Boutilier, M. S. H. 2011 *Experimental Investigation of Transition over a NACA 0018 Airfoil at a Low Reynolds Number*. Master Thesis, University of Waterloo. ↩

[101] Lambert, A. R. 2015 *Vortex Dynamics within the Laminar Separation Bubble over a NACA 0018 Airfoil at Low Reynolds Numbers*. Master Thesis, University of Waterloo. ↩

[102] Kurelek, J. W. 2016 *Transition in a Laminar Separation Bubble and the Effect of Acoustic Excitation*. Master Thesis, University of Waterloo. ↩

[103] Istvan, M. S. 2017 *Effects of free-stream turbulence intensity on transition within a laminar separation bubble*. Master Thesis, University of Waterloo. ↩

[104] Wynnychuk, D. W. 2019 *Characterization of Laminar Separation Bubbles Using Infrared Thermography*. Master Thesis, University of Waterloo. ↩

[105] Taylor, G. I. 1938 The Spectrum of Turbulence. *Proceedings of the Royal Society A: Mathematical, Physical and Engineering Sciences* **164** (919), 476–490. DOI. ↩

[106] Raffel, M., Willert, C. E., Wereley, S. T., & Kompenhans, J. 2007 *Particle Image Velocimetry*, number 1. Springer Berlin Heidelberg, p. 680. DOI. ↩

[107] Scarano, F. & Riethmuller, M. L. 2000 Advances in iterative multigrid PIV image processing. *Experiments in Fluids* **29** (7), S051–S060. DOI. ↩

[108] Westerweel, J. 1994 Efficient detection of spurious vectors in particle image velocimetry data. *Experiments in Fluids* **16-16** (3-4), 236–247. DOI. ↩

[109] Wieneke, B. 2015 PIV uncertainty quantification from correlation statistics. *Measurement Science and Technology* **26** (7), 074002. DOI. ↩

[110] Prasad, A. K. 2000 Stereoscopic particle image velocimetry. *Experiments in Fluids* **29** (2), 103–116. DOI. ↩

[111] Wieneke, B. 2005 Stereo-PIV using self-calibration on particle images. *Experiments in Fluids* **39** (2), 267–280. DOI. ↩

[112] Westerweel, J. & Scarano, F. 2005 Universal outlier detection for PIV data. *Experiments in Fluids* **39** (6), 1096–1100. DOI. ↩

[113] Taira, K., Brunton, S. L., Dawson, S. T. M., Rowley, C. W., Colonius, T., McKeon, B. J., Schmidt, O. T., Gordeyev, S., Theofilis, V., & Ukeiley, L. S. 2017 Modal Analysis of Fluid Flows: An Overview. *AIAA Journal* **55** (12), 4013–4041. DOI. ↩

[114] Sirovich, L. 1987 Turbulence and the dynamics of coherent structures. I. Coherent structures. *Quarterly of Applied Mathematics* **45** (3), 561–571. DOI. ↩

[115] Chatterjee, A. 2000 An introduction to the proper orthogonal decomposition. *Current Science* **78** (7), 808–817. ↩

[116] Legrand, M., Nogueira, J., & Lecuona, A. 2011 Flow temporal reconstruction from non-time-resolved data part I: mathematic fundamentals. *Experiments in Fluids* **51** (4), 1047–1055. DOI. ↩

[117] Van Oudheusden, B. W., Scarano, F., van Hinsberg, N. P., & Watt, D. W. 2005 Phase-resolved characterization of vortex shedding in the near wake of a square-section cylinder at incidence. *Experiments in Fluids* **39** (1), 86–98. DOI. ↩

[118] Lengani, D., Simoni, D., Ubaldi, M., & Zunino, P. 2014 POD analysis of the unsteady behavior of a laminar separation bubble. *Experimental Thermal and Fluid Science* **58**, 70–79. DOI. ↩

[119] Ben Chiekh, M., Michard, M., Grosjean, N., & Béra, J.-C. 2004 Reconstruction temporelle d'un champ aérodynamique instationnaire à partir de mesures PIV non résolues dans le temps. *9e Congrès Francophone de Vélocimétrie Laser* **81**, 14–17. ↩

[120] Legrand, M., Nogueira, J., Tachibana, S., Lecuona, A., & Nauri, S. 2011 Flow Temporal Reconstruction from Non Time-Resolved Data Part II: Practical Implementation, Methodology Validation, and Applications. *Experiments in Fluids* **51** (4), 861–870. DOI. ↩

[121] Kurelek, J. W. 2021 *The Vortex Dynamics of Laminar Separation Bubbles*. PhD thesis, University of Waterloo. ↩

[122] Applin, Z. T. 1995 Pressure Distributions from Subsonic Tests of a NACA 0012 Semispan Wing Model. *Tech. rep.* NASA TM-110148. ↩

[123] Theodoresen, T. 1931 The Theory of Wind-Tunnel Wall Interference. *Tech. rep.* NACA TR-410. ↩

[124] Hain, R., Kähler, C. J., & Radespiel, R. 2009 Dynamics of laminar separation bubbles at low-Reynolds-number aerofoils. *Journal of Fluid Mechanics* **630**, 129–153. DOI. ↩

[125] Yarusevych, S. & Kotsonis, M. 2017 Steady and transient response of a laminar separation bubble to controlled disturbances. *Journal of Fluid Mechanics* **813**, 955–990. DOI. ↩

[126] Reed, H. L. & Saric, W. S. 1989 Stability of Three-Dimensional Boundary Layers. *Annual Review of Fluid Mechanics* **21** (1), 235–284. DOI. ↩

[127] Jeong, J. & Hussain, F. 1995 On the identification of a vortex. *Journal of Fluid Mechanics* **285**, 69–94. DOI. ↩

[128] Häggmark, C. P., Bakchinov, A. A., & Alfredsson, P. H. 2000 Experiments on a two–dimensional laminar separation bubble. *Philosophical Transactions of the Royal Society of London. Series A: Mathematical, Physical and Engineering Sciences* **358** (1777), 3193–3205. Duck, P. W. & Ruban, A. I., editors. DOI. ↩

[129] Michelis, T. 2017 *Boundary Layer Separation Diagnostics and Control*. PhD thesis, Delft University of Technology. DOI. ↩

[130] Nati, A., de Kat, R., Scarano, F., & van Oudheusden, B. W. 2015 Dynamic pitching effect on a laminar separation bubble. *Experiments in Fluids* **56** (9), 172. DOI. ↩

[131] Squire, H. B. 1933 On the stability for three-dimensional disturbances of viscous fluid flow between parallel walls. *Proceedings of the Royal Society of London. Series A, Containing Papers of a Mathematical and Physical Character* **142** (847), 621–628. DOI. ↩

[132] Lamar, J. E. 1974 Extension of Leading-Edge-Suction Analogy to Wings with Separated Flow Around the Side Edges. *Tech. rep.* NASA Technical Report R-428. ↩

[133] Yen, S. C. & Huang, L. C. 2009 Flow Patterns and Aerodynamic Performance of Unswept and Swept-Back Wings. *Journal of Fluids Engineering* **131** (11), 1111011–11110110. DOI. ↩

[134] Ananda, G. K., Selig, M. S., & Deters, R. W. 2018 Experiments of Propeller-Induced Flow Effects on a Low-Reynolds-Number Wing. *AIAA Journal* **56** (8), 3279–3294. DOI. ↩

[135] Hultquist, J. 1992 Constructing stream surfaces in steady 3D vector fields. In *Proceedings Visualization '92*, pp. 171–178, Boston. IEEE Comput. Soc. Press. DOI. ↩

[136] Marxen, O., Kotapati, R. B., Mittal, R., & Zaki, T. 2015 Stability analysis of separated flows subject to control by zero-net-mass-flux jet. *Physics of Fluids* **27** (2), 024107. DOI. ↩

[137] Lengani, D., Simoni, D., Ubaldi, M., Zunino, P., & Bertini, F. 2017 Experimental Investigation on the Time–Space Evolution of a Laminar Separation Bubble by Proper Orthogonal Decomposition and Dynamic Mode Decomposition. *Journal of Turbomachinery* **139** (3). DOI. ↩

[138] Kurelek, J. W., Kotsonis, M., & Yarusevych, S. 2018 Transition in a separation bubble under tonal and broadband acoustic excitation. *Journal of Fluid Mechanics* **853**, 1–36. DOI. ↩

[139] Lucca-Negro, O. & O'Doherty, T. 2001 Vortex breakdown: a review. *Progress in Energy and Combustion Science* **27** (4), 431–481. DOI. ↩

[140] Giuni, M. & Green, R. B. 2013 Vortex formation on squared and rounded tip. *Aerospace Science and Technology* **29** (1), 191–199. DOI. ↩

[141] Francis, T. B. & Katz, J. 1988 Observations on the Development of a Tip Vortex on a Rectangular Hydrofoil. *Journal of Fluids Engineering* **110** (2), 208–215. DOI. ↩

[142] Moffat, R. J. 1988 Describing the uncertainties in experimental results. *Experimental Thermal and Fluid Science* **1** (1), 3–17. DOI. ↩

[143] Sciacchitano, A. & Wieneke, B. 2016 PIV uncertainty propagation. *Measurement Science and Technology* **27** (8), 084006. DOI. ↩

[144] Yavuzkurt, S. 1984 A Guide to Uncertainty Analysis of Hot-Wire Data. *Journal of Fluids Engineering* **106** (2), 181–186. DOI. ↩

[145] Wieneke, B. 2017 *PIV Uncertainty Quantification and Beyond*. PhD thesis, Technische Universiteit Delft, p. 289. DOI. ↩

[146] Samimy, M. & Lele, S. K. 1991 Motion of particles with inertia in a compressible free shear layer. *Physics of Fluids A: Fluid Dynamics* **3** (8), 1915–1923. DOI. ↩

[147] Lawson, N. J. & Wu, J. 1997 Three-dimensional particle image velocimetry: experimental error analysis of a digital angular stereoscopic system. *Measurement Science and Technology* **8** (12), 1455–1464. DOI. ↩

[148] Benedict, L. H. & Gould, R. D. 1996 Towards better uncertainty estimates for turbulence statistics. *Experiments in Fluids* **22** (2), 129–136. DOI. ↩

[149] Ahn, S. & Fessler, J. 2003 Standard Errors of Mean, Variance, and Standard Deviation Estimators. *Tech. rep.*, EECS Department, University of Michigan, pp. 1–2. URL. ↩

[150] Welch, P. 1967 The use of fast Fourier transform for the estimation of power spectra: A method based on time averaging over short, modified periodograms. *IEEE Transactions on Audio and Electroacoustics* **15** (2), 70–73. DOI. ↩

[151] Manolakis, D., Ingle, V., & Kagon, S. 2000 Nonparametric Power Spectrum Estimation. In *Statistical and Adaptive Signal Processing*, part 5. McGraw-Hill. ↩

[152] Cao, N., Ting, D. S.-K., & Carriveau, R. 2011 The Performance of a High-Lift Airfoil in Turbulent Wind. *Wind Engineering* **35** (2), 179–196. DOI. ↩

[153] Norberg, C. 2003 Fluctuating lift on a circular cylinder: review and new measurements. *Journal of Fluids and Structures* **17** (1), 57–96. DOI. ↩

[154] Wolf, S. W. 1995 Adaptive wall technology for improved wind tunnel testing techniques—A review. *Progress in Aerospace Sciences* **31** (2), 85–136. DOI. ↩

[155] Deperrois, A. 2019 XFLR5. URL. ↩

Appendices

Appendix A

Experimental Uncertainty

The value of any measured quantity is subject to errors that lead to uncertainty in the true value. The total uncertainty (U) in a measured quantity (F) subject to N sources of error is [142]:

$$U(F) = \sqrt{\sum_{i=1}^{N} U_i^2} \tag{A.1}$$

where U_i is the uncertainty in F due to error source i. Each U_i must represent the uncertainty at the same confidence level [142], typically 95%. Often it is desired to calculate the uncertainty of a function of several variables, where each variable has its own associated uncertainty. The uncertainty in the value of the function F calculated from N variables $(a_i, i = 1...N)$ can be determined using the equation [143]:

$$U(F) = \sqrt{\sum_{i=1}^{N}\sum_{j=1}^{N} \frac{\partial F}{\partial a_i}\frac{\partial F}{\partial a_j} R_{a_i a_j} U(a_i) U(a_j)} \tag{A.2}$$

Where $U(a_i)$ is the uncertainty in variable a_i, and $R_{a_i a_j}$ is the cross-correlation coefficient between the errors of a_i and a_j. For variables whose errors are statistically independent, $R_{a_i a_j} = 0$. In many situations, the sensitivities $\partial F/\partial a_i$ cannot be derived explicitly. In that case, $U(F)$ can be estimated using the method of sequential perturbation described by Moffat [142]. Sequential perturbation is performed as follows. To calculate the uncertainty $U(F)$, the value of F is first calculated. Then the value of a single variable a_i is perturbed by $U(a_i)$ and F is recalculated. The change in F resulting from the change in a_i by $U(a_i)$ is taken to be the uncertainty in F resulting from the uncertainty in a_i. This process is repeated for $i = 1, ..., N$. The total uncertainty in F is then calculated using Eq. A.1.

Table A.1 lists the uncertainties in all measured and derived quantities, and the following sections provide details of how the uncertainty estimates were obtained.

Table A.1: Uncertainties of measured and derived quantities. All uncertainties are given with 95% confidence. For spatially varying uncertainties, the maximum uncertainty is tabulated.

Parameter	Conditions	Uncertainty	Applies to
sAR		± 0.010	
Re_c		± 2800	
Tu		$\pm 0.0021\%$	
α		$\pm 0.2^\circ$	
$C_{\overline{p}}$		± 0.014	Figs. 4.1, 4.2a–4.2d, and 4.3
α_{eff}		$\pm 0.6^\circ$	Fig. 4.4
$\overline{u}$	Side View 2C-PIV	$\leq \pm 0.048 u_\infty$	Fig. 4.5
u'_{RMS}	Side View 2C-PIV	$\leq \pm 0.068 u_\infty$	Fig. 4.11
v'_{RMS}	Side View 2C-PIV	$\leq \pm 0.034 u_\infty$	Fig. 4.12
u	Top View 2C-PIV	$\leq \pm 0.31 u_\infty$	Fig. 4.17
$\overline{w}$	Top View 2C-PIV	$\leq \pm 0.13 u_\infty$	Fig. 4.5
$\overline{u}$	Side View 3C-PIV	$\leq \pm 0.13 u_\infty$	Fig. 5.1a
$\overline{v}$	Side View 3C-PIV	$\leq \pm 0.12 u_\infty$	Fig. 5.1b
$\overline{w}$	Side View 3C-PIV	$\leq \pm 0.26 u_\infty$	Fig. 5.1c
u'_{RMS}	Side View 3C-PIV	$\leq \pm 0.18 u_\infty$	Fig. 5.7a
v'_{RMS}	Side View 3C-PIV	$\leq \pm 0.17 u_\infty$	Fig. 5.7b
w'_{RMS}	Side View 3C-PIV	$\leq \pm 0.42 u_\infty$	Fig. 5.7c
δ^*_x	Side View 2C-PIV	$\leq \pm 0.0008c$	Figs. 4.5, 4.7, 4.11, and 4.12
δ^*_x	Side View 3C-PIV	$\leq \pm 0.0006c$	Figs. 5.1, 5.4a, 5.6a, 5.7, and 5.14
H		$\leq \pm 2.3$	Fig. 5.8
x_s		$\leq \pm 0.046c$	Figs. 4.5, 4.6, 4.11, 4.12, and 4.17
x_t	From δ^*_{xmax}	$\leq \pm 0.013c$	Figs. 4.5, 4.6, 4.11, 4.12, and 4.17
x_H		$\leq \pm 0.036c$	Fig. 5.8
x_r		$\leq \pm 0.0076c$	Figs. 4.5, 4.6, 4.11, 4.12, and 4.17
$\overline{y}$		$\leq \pm 0.00024c$	Fig. 5.14e
$\mathcal{F}_{v'v'}$	Side View 2C-PIV	$^{+0.64}_{-0.33}\ \mathcal{F}_{v'v'}$	Figs. 4.13–4.15
$\mathcal{F}_{v'v'}$	Side View 3C-PIV	$^{+0.063}_{-0.061}\ \mathcal{F}_{v'v'}$	Fig. 5.20

Continued...

Parameter	Conditions	Uncertainty	Applies to
λ_0	From $\mathcal{F}_{v'v'}$	$\leq \pm 0.0022c$	Fig. 5.21
λ_0	From vortex identification	$\leq \pm 0.0014c$	Fig. 5.14e
St_0	Side View 2C-PIV	$\leq \pm 3.3$	Figs. 4.13, 4.14, and 4.16
St_0	Side View 3C-PIV	$\leq \pm 1.5$	Fig. 5.21
$\frac{\partial \overline{V}}{\partial z}$		$\leq \pm 0.00037 u_\infty c$	Fig. 5.6b
$\oint_l \overline{\mathbf{u}} \cdot \hat{\mathbf{n}} dl$		$\leq \pm 0.00061 u_\infty c$	Fig. 5.6b
$\sigma_{v'max}$		$\leq \pm 6.6$	Fig. 5.9b

A.1 Pressure Measurements

There are three major sources of uncertainty in the pressure measurements: the finite accuracy of the pressure transducers, the discretisation of transducer signals by the data acquisition system, and the pressure transducer calibrations. The Setra model 239 pressure transducers used in this study have a rated accuracy of 0.14% full scale. Airfoil surface pressure measurements were taken using transducers with a full scale of 498 Pa, while the pressure drop across the wind tunnel contraction was taken using a transducer with a full scale of 1244 Pa. The NI-9234 data acquisition system used to read the voltage signals from the pressure transducers was capable of resolving a minimum change in pressure of 0.019 Pa. The uncertainty of the pressure transducer calibrations was determined from the root mean squared error (RMSE) of the data points used the linear calibration fits. The total uncertainty of surface pressure measurements was estimated to be no greater than 0.71 Pa or $0.014Q$. Equivalently, the uncertainty in surface pressure coefficients is 0.014. Following the same procedure, the uncertainty in the pressure drop across the wind tunnel contraction was estimated to be 1.8 Pa.

A.2 Experimental Conditions

The quantities that define the experimental conditions consist of the Reynolds number, turbulence intensity, angle of attack, and semi-aspect ratio.

The Reynolds number was calculated from the freestream velocity, airfoil chord length, and kinematic viscosity. The freestream velocity was calculated from the dynamic pressure given by the calibration of the pressure drop across the contraction of the wind tunnel. The dynamic pressure was therefore subject to calibration uncertainty and uncertainty in the measurement of the pressure drop across the contraction. The calibration uncertainty was determined from the RMSE of the linear calibration fit. Combining the calibration uncertainty with the contraction pressure drop measurement uncertainty from Appendix A.1,

the total uncertainty in q_∞ was estimated to be 1.8 Pa. The uncertainty in air density, estimated to be 0.0087 kg m^{-2} also contributes to uncertainty in the freestream velocity. The total uncertainty in freestream velocity was estimated to be 0.17 m s^{-1}. Also contributing to uncertainty in the Reynolds number is the uncertainty in the kinematic viscosity, which was estimated to be 2.0×10^{-7} m^2 s^{-1}. The uncertainty in Reynolds number due to the uncertainty in airfoil chord length was considered to be negligible. The total uncertainty in the Reynolds number was estimated to be 2800.

The turbulence intensity in the empty test section was measured using a single normal hotwire anemometer, calibrated against a Pitot tube. The dominant uncertainties in the velocity measured by the hotwire anemometer are attributed to uncertainty in the fourth order polynomial calibration fit [144], estimated to be 0.026 m s^{-1}, and the uncertainty of the freestream velocity measured by the Pitot tube during the calibration [144], estimated to be 0.17 m s^{-1}. The total uncertainty in turbulence intensity at the experimental conditions of this study was estimated to be 0.0021%.

The angle of attack of the wing model was measured using a digital protractor with a resolution of 0.1°. However, additional uncertainty in the angle of attack is introduced when attempting to determine the zero-lift angle of the wing. The zero lift angle was used to define the datum for angle of attack measurements since the wing model under consideration has a symmetric airfoil profile. The repeatability of surface pressure measurements was used to provide an overall estimate of the uncertainty in the angle of attack. It was found that after changing the angle of attack of the wing model and subsequently returning the angle of attack to the original angle, the change in the pressure distribution on the wing model was equivalent to a change in angle of attack of no more than 0.2°. Thus, the uncertainty in angle of attack was estimated to be ±0.2°

The span of the wing was measured with a tape measure with estimated uncertainty of 2 mm. The resulting uncertainty in semi-aspect ratio is 0.010.

A.3 Particle Image Velocimetry

Particle image velocimetry (PIV), is a complex measurement technique with numerous sources of uncertainty, many of which are difficult to quantify [106, 145]. Sources of error in the PIV measurement chain can be divided into two principal groups: bias errors in the calibration and alignment of the PIV system, and random errors propagated through the particle image cross-correlation algorithm [129]. Additional sources of error that also affect PIV measurements are timing errors of the laser and camera synchronisation system, and velocity lag of seeding particles with differing density from the surrounding fluid. Because the timing controller used in the present study has a rated jitter of 0.05 ns, timing errors are considered to be negligible. The velocity lag of the seeding particles can be described by the aerodynamic response time [146], which for the 1 µm diameter water-glycol particles used in this study is estimated to be on the order of 1 µs. Given that the LSB vortex shedding period is on the order of 1000 µs, the velocity lag of the seeding particles is also considered negligible.

The PIV system was calibrated by imaging a gridded calibration target and then fitting a third order polynomial function or pinhole camera model to the calibration images. The polynomial function or pinhole camera model provides a mapping between the image coordinates (pixels) and the physical coordinates (x, y, z or X, Z). A third order polynomial mapping function was used for the side view 3C and side view 2C configurations, while the top view 2C configuration used a pinhole camera model mapping function. Three major sources of uncertainty in the calibration process are the uncertainty of the location of the calibration target in physical space, the uncertainty in the distance between grid points on the target, and the uncertainty of the polynomial mapping function. The side view calibration target could be reliably located within 1 mm ($0.005c$) in the x and z directions and within 0.15 mm ($0.0008c$) and 0.1 mm ($0.0005c$) in the y direction for the side view 2C and side view 3C configurations, respectively. The top view 2C calibration target could be located within 2 mm ($0.01c$) in both the X and Z directions. The bias error in the location of the target affects the estimates of spatial locations obtained using the PIV data, such as the location of the wing surface, of separation, of transition, and of reattachment, but does not bias the magnitudes of measured velocities.

Errors in the identified locations of calibration target grid markers in calibration images and errors in the mapping functions contribute to bias errors in the measured velocities. The nominal distance between grid points in the calibration target images was 3.18 mm, 3.18 mm, and 4 mm, for the side view 2C, top view 2C, and side view 3C configurations respectively. The corresponding relative uncertainty in the distances between grid marker locations in the calibration images was 1.2% for the side view 2C and 3C configurations, and 2.0% for the top view 2C configuration.

The uncertainty in measured velocities due to the uncertainty of the mapping functions fit to the target grid points was quantified using the RMSE of the mapping functions, calculated to be 0.54%, 0.035%, and 0.028% of the distance between grid points for the side view 2C, top view 2C, and side view 3C configurations, respectively. The resulting total uncertainty in velocity magnitudes due to uncertainties in calibration, including the uncertainties of the distances between grid points and the polynomial mapping functions was calculated using Eq. A.1 to be 1.3%, 3.5%, and 1.2% for the side view 2C, top view 2C, and side view 3C configurations, respectively.

The previous discussion pertains to the in-plane velocity components of each PIV configuration. For the side view 3C configuration, the out-of-plane velocity component has an uncertainty that is proportional to the uncertainty of the in-plane velocity times $1/\tan(\gamma/2)$, where γ is the angle between the optical axes of the 3C PIV cameras [147]. The uncertainty of the in-plane and out-of-plane velocity components is equal when $\gamma = 90°$. For the 3C PIV configuration employed in this study, γ was limited to 35° because of physical limitations on camera positioning. Additionally, the relative uncertainty of the distance between levels on the stepped 3C PIV target in the out-of-plane direction is larger than the relative uncertainty in distances between grid points on the same level, because of the assumed constant machining tolerances and the small distance between levels (1 mm) in the z direction. The relative uncertainty in the separation between levels in the z direction on the stereo calibration target is 3%. The total calibration uncertainty for the out-of-plane

velocity component is estimated to be 4.6%.

Another source of calibration uncertainty in PIV measurements, which can be significant for 3C PIV, is the alignment of the light sheet with the calibration target [111]. Because the two cameras in the 3C PIV system view the light sheet from different directions, if the light sheet is not aligned with the calibration target, the locations of the same particles in the image coordinates of each camera will not map onto the same locations in physical space. If the same particles are not mapped to the same locations in physical space, then the velocities at each point in physical space will be computed from particle images at different locations in physical space, which introduces systematic errors, especially in regions with large velocity gradients. To correct potential misalignment between the 3C PIV calibration target and the light sheet, stereo self-calibration [111] was performed on a set of 100 particle images from each side view 3C measurement plane. After self-calibration, the remaining disparities in particle positions were less than 2px. Given the interrogation window size of 16px, errors due to misalignment of the light sheet were considered negligible after self-calibration.

The uncertainty in PIV measurements due to random errors was estimated using the correlation statistics method [109]. The correlation statistics method uses the calculated displacement field and the particle images to estimate uncertainty by considering the contributions of each pixel in the interrogation windows to asymmetry in the cross-correlation between particle images. The result of this method is an uncertainty estimate for each velocity vector calculated from each interrogation window in space and time. Contours of the RMS uncertainty due to random errors as estimated by the correlation statistics method are presented in Figs. A.1–A.3 for each PIV configuration.

For the side view 2C and side view 3C configurations (Figs. A.1 and A.3), only one representative z/c location from each configuration is shown. The largest uncertainty levels in both side view configurations occur in the turbulent reattaching boundary layer in the aft portion of the LSB. Higher uncertainty is expected in this region because of the substantial instantaneous spatial velocity gradients that occur in turbulent flow. The side view 3C configuration also has high uncertainty in the upstream laminar boundary layer, where large wall-normal velocity gradients are present. The uncertainty of the w component of the side view 3C configuration is greater than the in-plane velocity components because of the relatively narrow 35° angle between the optical axes of the cameras. In the top view 2C configuration (Fig. A.2), random localised regions of higher uncertainty occur where surface imperfections in the model cause light reflections from the laser.

A.4 Derived Quantities

For derived quantities that could be expressed explicitly as differentiable functions of measured quantities, the uncertainty in the derived quantity was calculated by propagating the uncertainties of measured quantities using Eq. A.2. For derived quantities calculated using more complex data processing procedures, sequential perturbation was used to estimate the resulting uncertainty of the derived quantity [142]. The remainder of this

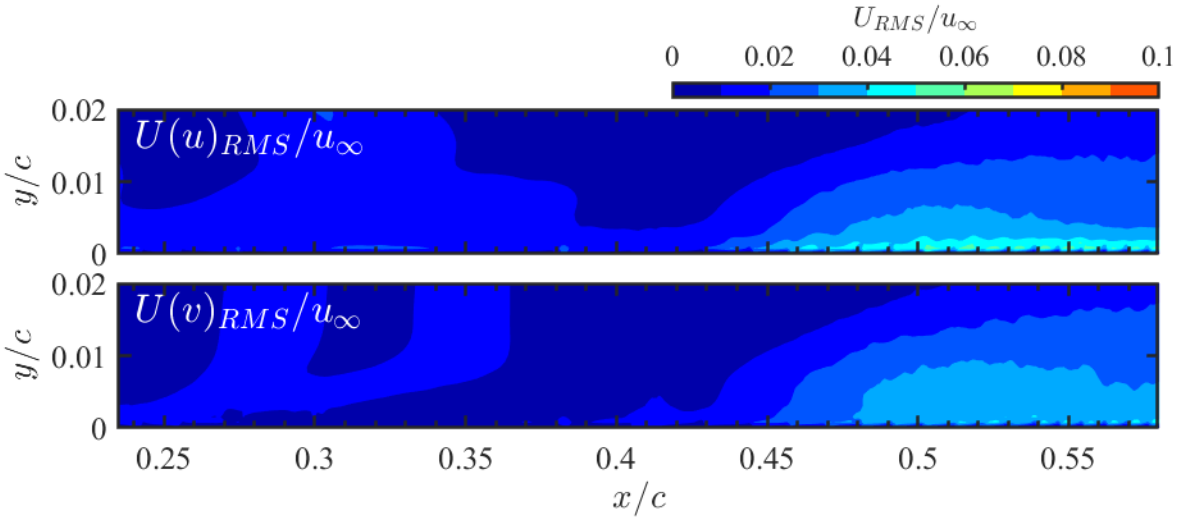

Figure A.1: RMS uncertainty of side view 2C measurements from correlation statistics [109] at $z/c = 1.30$.

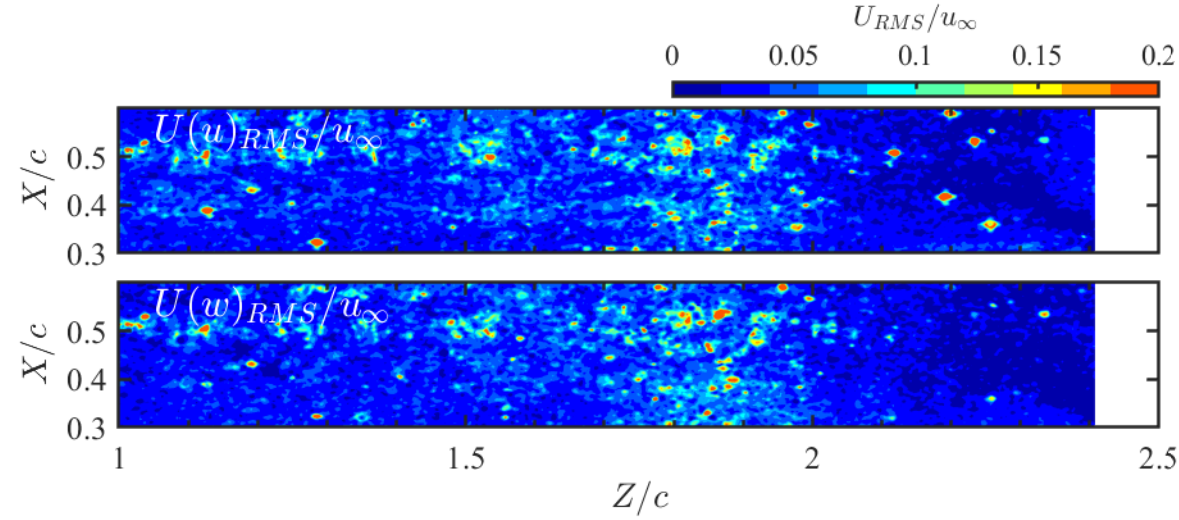

Figure A.2: RMS uncertainty of top view 2C measurements from correlation statistics [109].

section provides further details of the uncertainty estimation procedure for the principal results.

Velocity Statistics

As outlined in [143] and [148], the uncertainty of the mean velocity at a given point in space due to random noise and finite sample size is given by the following equation for a

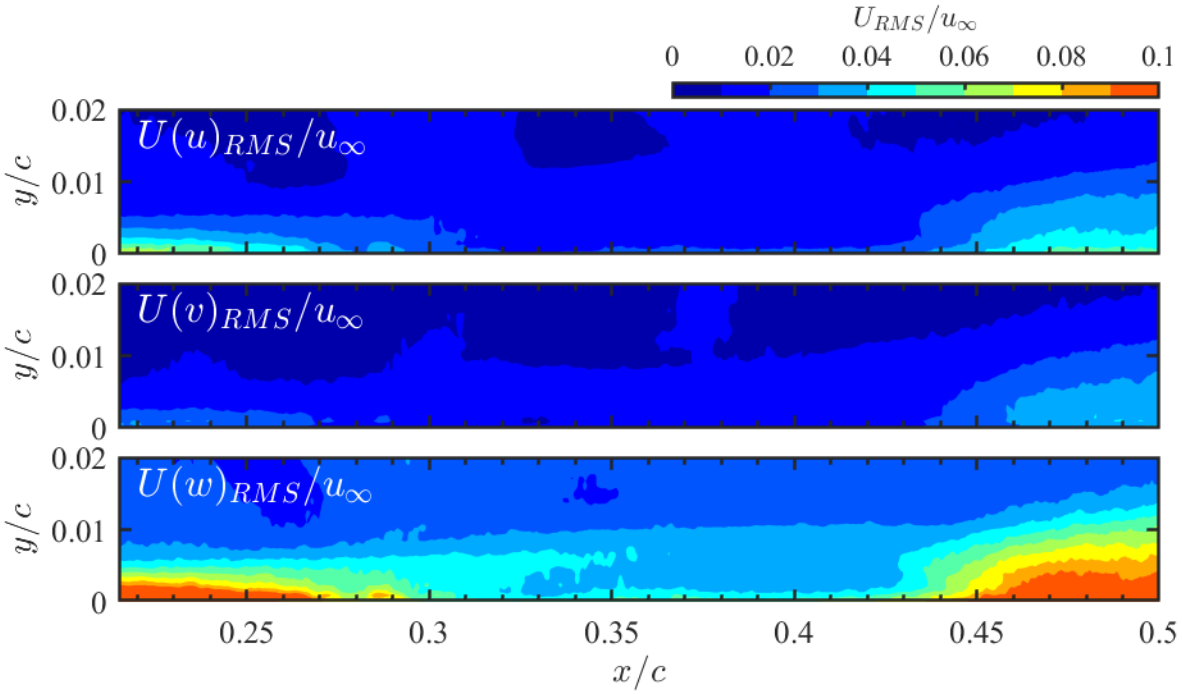

Figure A.3: RMS uncertainty of side view 3C measurements from correlation statistics [109] at $z/c = 1.25$.

95% confidence level:

$$U(\overline{u})_{random} = 1.96\frac{u'_{RMS}}{\sqrt{N_{eff}}} \tag{A.3}$$

where N_{eff} is the effective number of independent samples. Likewise, the uncertainty in RMS velocity at a given point in space due to random noise and finite sample size with 95% confidence is approximately [143, 148]:

$$U\left(u'_{RMS}\right)_{random} = 1.96u'_{RMS}\sqrt{\frac{2}{N_{eff}}} \tag{A.4}$$

The effective number of independent samples is defined as [143]:

$$N_{eff} = \frac{T}{2T_{int}} = \frac{T}{2\int_0^\infty R_{uu}(t)dt} \tag{A.5}$$

where T is the total sampling time, T_{int} is the integral time scale, and $R_{uu}(t)$ is the autocorrelation coefficient of u. Strictly, Eqs. (A.3) and (A.4) are valid only as $N_{eff} \to \infty$, however the errors are negligible for $N_{eff} > 100$ [149]. The total uncertainty in the mean and RMS fluctuating velocities can be calculated using Eq. A.2 to include both the uncertainties

due to random noise and uncertainties due to bias errors in the calibration:

$$U(\overline{u}) = \sqrt{U(\overline{u})^2_{random} + U(\overline{u})^2_{calibration}} \tag{A.6}$$

$$U\left(u'_{RMS}\right) = \sqrt{U\left(u'_{RMS}\right)^2_{random} + U\left(u'_{RMS}\right)^2_{calibration}} \tag{A.7}$$

Integral Boundary Layer Parameters

The uncertainties in integral boundary layer parameters δ^*_x, θ_x, $H = \delta^*_x/\theta_x$ and the dividing streamline height are affected by the uncertainties in mean velocity and by the uncertainty in locating the model surface in the PIV images. The uncertainties in integral boundary layer parameters were estimated by sequentially perturbing the mean velocity field by $\pm U(\overline{u})$ and the model surface position by $+U(y_{surface})$ and calculating the resulting total uncertainty using Eq. A.2. In Chapter 4 the locations of separation and reattachment were calculated by extrapolating the dividing streamline to the model surface. The same procedure was used to estimate the uncertainties in locations of separation and reattachment, with the additional uncertainty of the PIV target location of $0.005c$ incorporated using Eq. A.2.

Effective Angle of Attack

In Section 4.2, effective angle of attack estimates were made by minimising the sum of squared differences between surface pressure measurements on the wing and linear fits to surface pressure measurements on the two-dimensional airfoil at multiple reference angles of attack. The effective angle of attack estimates are therefore subject to uncertainty in the reference angles of attack of the two-dimensional airfoil, and uncertainty related to the nonzero residual differences between the surface pressure measurements on the wing and the linear fits. The uncertainty in the reference angles of attack of the two-dimensional airfoil is 0.2°, as explained in Appendix A.2. To quantify the uncertainty due to the residual differences between the surface presssure measurements on the wing and the linear fits, the change in effective angle of attack necessary to eliminate the residual difference of each pressure tap independently was calculated for the three pressure taps at each spanwise location. The uncertainty due to the residual differences was taken as the maximum of the three changes in effective angle of attack. This uncertainty was combined with the uncertainty of the reference angles of attack of the two-dimensional airfoil using Eq. A.1 to produce an overall estimate of the uncertainty in effective angle of attack at each spanwise pressure tap location.

Fluctuating Velocity Spectra

All velocity spectra were computed from the PIV measurements using Welch's method with 50% overlap between windows [150]. Welch's method estimates the power spectral density using a weighted average of the spectra from each window [150]. With 50% overlap,

the variance of the Welch's power spectral density estimate approximately follows a χ^2 distribution with the number of degrees of freedom equal to twice the number of windows [151]. The frequency resolution is equal to f_s/N, where f_s is the sampling frequency and N is the number of samples per window.

For the frequency spectra presented in Chapter 4, 20 windows of 512 samples were used. The corresponding uncertainty interval for the power spectral density is 67% to 164%. The uncertainty in frequency, equal to half of the frequency resolution, is $\pm 0.080 u_\infty/c$ or $\pm 3.8\,\mathrm{Hz}$.

For the wavelength spectra presented in Chapter 5, each spectrum was obtained by averaging the spectra from all 1000 instantaneous velocity fields. Each individual spectra was calculated from approximately 630 velocity samples with a spacing of $0.0004c$ in the x direction at each measurement plane. The corresponding uncertainty interval for the power spectral density is 94% to 107%. The uncertainty in wavenumber, equal to half of the wavenumber resolution, is $\pm 4.32/c$ or $\pm 21.6\,\mathrm{m}^{-1}$, equivalent to a wavelength uncertainty of $\pm \lambda^2/(0.25c)$.

Convection Velocity

In Section 5.3, vortex convection velocities were estimated at $x = x_H$ and $y = \delta_x^*$. The uncertainty in integral boundary layer parameters H and δ_x^* is dominated by the uncertainty in the location of the wing surface. However, the uncertainty of the location of the wing surface was not propagated into the uncertainty of convection velocities because the uncertainty in location of the wing surface is independent of the uncertainty in location of the separated shear layer where the vortices convect. Therefore, the uncertainty in convection velocities was estimated by perturbing the mean velocity field only.

Central Instability and Fundamental Vortex Shedding Frequencies

The procedure for calculating central instability frequencies from time resolved side view 2C PIV data in Section 4.4 consisted of the following steps. First, wall-normal fluctuating velocity spectra were computed at $y = \delta_x^*$ at each PIV velocity vector location from $x_t - 0.02c$ to x_t, using a single window of 5457 samples. Secondly, the velocity spectra were smoothed using locally weighted least-squares quadratic regression with a window width of 364 Hz. Lastly, the frequency of maximum power spectral density from each smoothed spectra was averaged over x to obtain an estimate of the central instability frequency. The total uncertainty of the central instability frequency was calculated using Eq. A.1 to include the uncertainty due to the variance of the peak power spectral densities over x and the uncertainty due to the finite frequency resolution of the computed spectra. The uncertainty due to finite frequency resolution was one-half of the frequency resolution of the computed spectra, equal to $0.080 u_\infty/c$ (3.8 Hz).

In Section 5.3 the fundamental shear layer vortex shedding frequencies were estimated from convection velocities and streamwise wavelengths. The uncertainty in fundamen-

tal shear layer vortex shedding frequency was propagated from the uncertainties of the convection velocities and streamwise wavelengths using Eq. A.2.

Control Volume Analysis

The uncertainties in the the in-plane outflow ($\oint_l \overline{\mathbf{u}} \cdot \hat{\mathbf{n}} dl$), and out of plane outflow ($\partial \overline{\dot{V}} / \partial z$), in the control volume analysis of Section 5.1 were calculated by propagating the uncertainty of measured velocities using Eq. A.2. Because the interrogation windows used for PIV vector calculation were overlapping, it was assumed that the errors in the u, v and w velocity components were perfectly correlated between velocity vectors calculated from overlapping interrogation windows. With 75% window overlap, velocity errors were assumed to be correlated between the neighbouring 3 velocity vectors in the positive and negative x and y directions.

Growth Rates of Velocity Fluctuations

The dominant uncertainty in the calculation of the streamwise growth rates of wall-normal velocity fluctuations ($\sigma_{v'max}$) is the uncertainty in v'_{RMS}. The growth rates were calculated using an exponential fit to the regions of exponential disturbance growth. Therefore, the greatest error in $\sigma_{v'max}$ would occur if the velocity fluctuations at the beginning of the region of exponential growth were lower than measured, while the velocity fluctuations at the end of the region of exponential growth were higher than measured, or vice versa. To estimate the consequent uncertainty in growth rates, sequential perturbation was performed by perturbing the values of v'_{RMS} at the beginning and end of the region of exponential growth by $U(v'_{RMS})$ in opposing senses.

Appendix B

Facility Characterisation

The recirculating wind tunnel at the University of Waterloo is designed to provide a low disturbance environment for low-Reynolds number research. Due to the sensitivity of LSBs to the disturbance environment, the conditions in the test section where characterised before performing wing experiments.

B.1 Freestream Velocity Calibration

To unintrusively determine the freestream velocity in the test section, an array of surface static pressure taps are connected to the 9:1 contraction of the wind tunnel. Four taps are located around the perimeter of the entrance to the contraction, and four taps are located around the perimeter of the contraction exit. The two sets of four pressure taps are mechanically averaged by virtue of their connection to the two pressure ports of a single pressure transducer. Applying the Bernoulli equation and conservation of mass to the flow between the entrance and exit of the contraction, the following relation can be obtained between the dynamic pressure in the test section (q_∞) and the pressure drop across the contraction (Δp):

$$QC = \Delta p$$

For an ideal flow with zero losses, the contraction coefficient (C) is equal to $(1 - 1/r^2)$, where r is the contraction ratio, which for this wind tunnel is 9. The actual value of C is less than its ideal value due to energy losses. By placing a Pitot-static probe in the empty test section at the location of the wing model, the dynamic pressure was measured and used to determine C. The pressure drop across the contraction and the dynamic pressure from the Pitot-static tube were both measured using a Setra model 239 pressure transducer

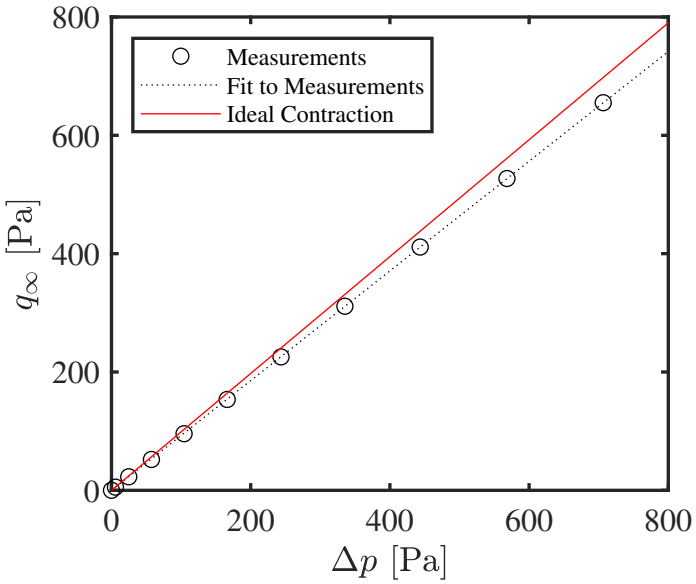

Figure B.1: Test section dynamic pressure versus contraction pressure drop.

connected to a National Instruments NI-9234 data acquisition system. Measurements were taken at motor drive frequencies between 0 Hz and 60 Hz in increments of 6 Hz. Figure B.1 presents the measured values of the contraction pressure drop and test section dynamic pressure that were used to determine the contraction coefficient.

Using the linear fit to the measured data, C was determined to be 0.9271, which is less than the ideal value of 0.9876. Once the freestream dynamic pressure has been determined using the contraction pressure drop and the calibrated contraction coefficient, the freestream velocity in the test section can be computed using the relation:

$$u_\infty = \sqrt{\frac{2q_\infty}{\rho}}$$

which enables valid freestream velocity calculations despite changes in air density due to changing meteorological conditions. All measurements were conducted at a chord Reynolds number of 1.25×10^5, which corresponds to a freestream velocity of approximately $9.5\,\mathrm{m\,s^{-1}}$.

B.2 Freestream Uniformity

The uniformity of the flow in the test section was assessed using a traversing Pitot-static probe connected to a Setra model 239 pressure transducer. Data was acquired using a National Instruments NI-9234 data acquisition system. The Pitot-static probe was an L shaped probe, approximately 0.6 m in length. The probe tip was aligned to the freestream direction while the main shaft of the probe extended out of the side of the test section. Outside the test section, the shaft of the probe was connected to a two-axis traverse. The traversing hardware remained outside the test section and a slot was opened in the side of

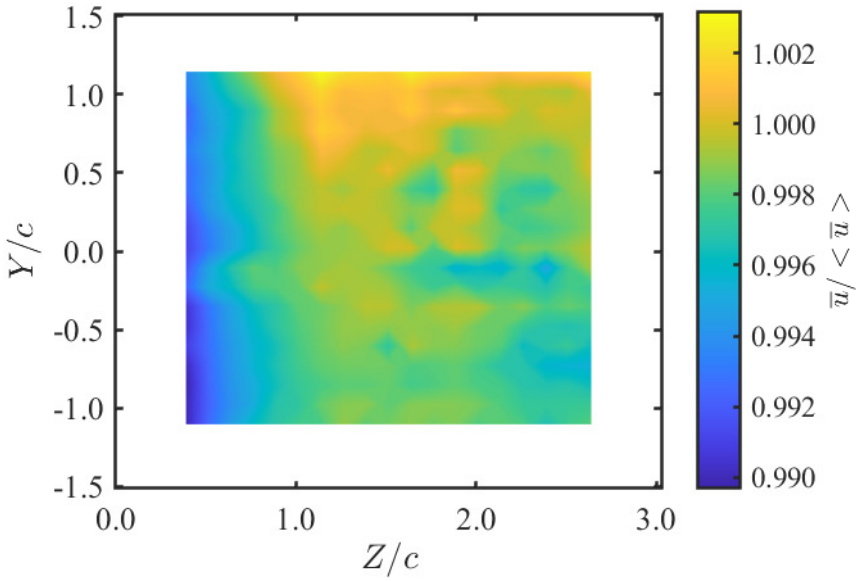

Figure B.2: Freestream velocity uniformity.

the test section to allow the shaft of the Pitot-static probe to move both horizontally and vertically. Velocity measurements were taken in a grid pattern with $0.125c$ spacing between measurement points in both the horizontal and vertical directions. The open slot affected the flow near $Z/c = 0$, causing lower freestream velocities to be measured in this region. Figure B.2 shows the time-averaged velocity in the cross sectional plane traversed by the Pitot-static probe, normalised by the spatially and time-averaged velocity ($< \overline{u} >$). Despite the non-uniformity caused by the open slot at $Z/c = 0$, the freestream velocity across the entire measurement region remained within $\pm 1.1\%$ of the mean velocity. In the spanwise region where PIV measurements were performed ($0.95 \leq Z/c \leq 2.5$), the freestream velocity was within $\pm 0.4\%$ of the mean velocity.

B.3 Disturbance Environment

Velocity fluctuations were measured using a single normal hotwire probe at the centre of the empty test section, $0.4c$ upstream of the position of the leading edge of the wing model. Sampling was conducted at 51.2 kHz for 20 s. The hotwire probe signal was measured using a Dantec Dynamics constant temperature anemometry hotwire bridge and a National Instruments NI-9234 data acquisition system. The velocity signal was filtered to reduce high frequency electrical noise using a digital Butterworth low pass filter having a passband frequency of 10 kHz, a stopband frequency of 11 kHz, and 80 dB attenuation in the stopband. Turbulence intensity was calculated by dividing the filtered RMS velocity fluctuations by the mean velocity. Turbulence intensity measurements were conducted for motor drive frequencies between 0 Hz and 60 Hz in increments of 6 Hz. Figure B.3 presents the turbulence intensity measured in the empty test section as a function of freestream velocity. The wing

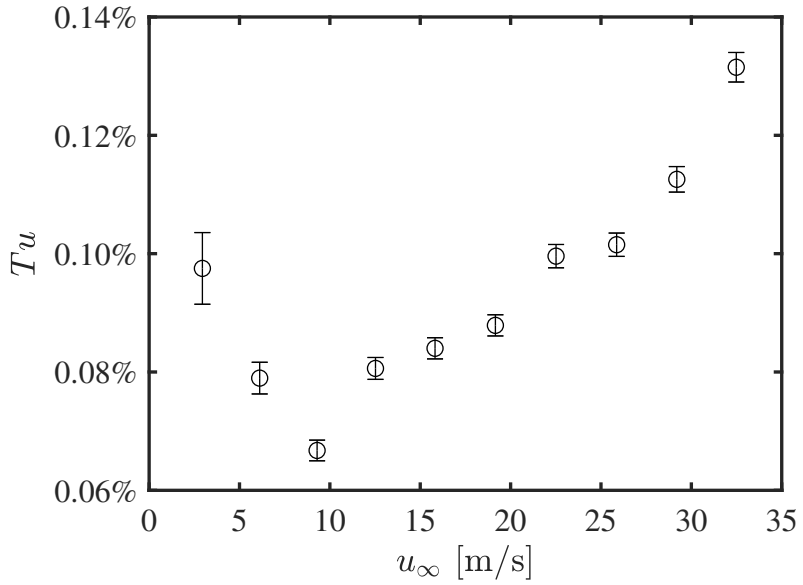

Figure B.3: Freestream turbulence intensity versus freestream velocity.

experiments in this study were performed at approximately $9.5\,\mathrm{m\,s^{-1}}$ where the turbulence intensity is less than 0.08%.

Figure B.4a presents the spectrum of velocity fluctuations measured by the hotwire probe in the empty test section at $u_\infty = 9.29\,\mathrm{m\,s^{-1}}$. At Strouhal numbers greater than 8, no velocity fluctuations are observed that are substantially greater than the background noise in the hotwire signal. The central instability frequency of the LSB on the wing of 16.54 is considerably higher than the relatively large velocity fluctuations that are observed at $St < 8$. The central instability frequencies of the LSBs forming on the airfoil over the range $3.8° \leq \alpha \leq 6.0°$ were within the range $13.16 \leq St \leq 21.89$, which also does not contain any substantial turbulent fluctuations relative to the background hotwire signal noise.

To characterise the accoustic environment in the test section, a Brüel and Kjæl type 4192 1/2 inch pressure field microphone was placed in the flow at the downstream end of the empty test section. Free-field pressure fluctuations were recorded using the microphone at 40 kHz for 105 s. The sound pressure level was measured to be 80.7 dB. Figure B.4b presents the spectrum of the free-field pressure fluctuations measured by the microphone. No significant spectral content was observed near the central instability frequencies of the LSBs studied on the wing or airfoil.

The integral time scale of the turbulent velocity fluctuations can be determined by integrating the autocorrelation function of the velocity fluctuations [152], which should trend towards zero as time approaches infinity. Since only a finite duration of velocity measurements were taken, an exponential curve fit to the autocorrelation function was used to calculate the integral time scale [103, 153]. Figure B.5 shows the autocorrelation function of the velocity fluctuations and the exponential fit at $u_\infty = 9.29\,\mathrm{m\,s^{-1}}$. The integral time scale was calculated to be $0.26c/u_\infty$. By applying Taylor's frozen turbulence hypothesis [105], the integral length scale is $0.26c$ (52.3 mm).

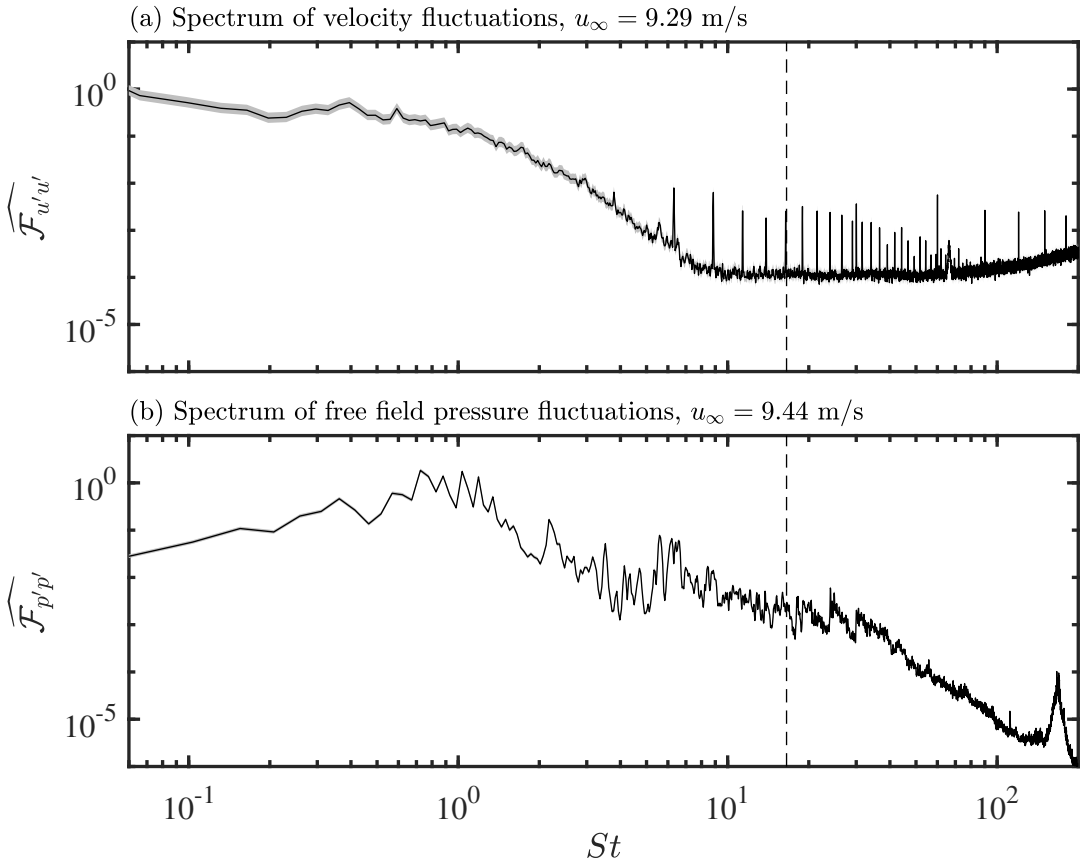

Figure B.4: Spectra of velocity and pressure fluctuations in the empty test section. Shaded area represents uncertainty. Dashed line is the central instability frequency of the LSB on the $sAR = 2.5$ wing.

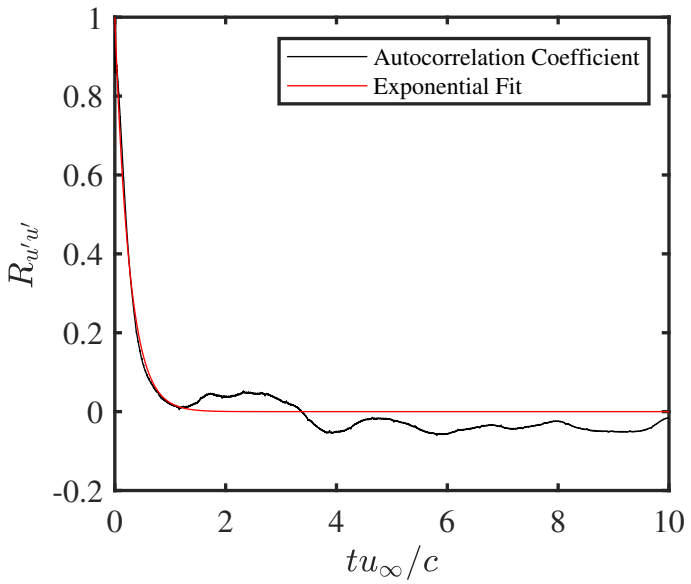

Figure B.5: Autocorrelation coefficient of velocity fluctuations in the empty test section at $u_\infty = 9.29\,\mathrm{m\,s^{-1}}$.

Appendix C

Assessment of Wind Tunnel Wall Interference

Although the purpose of a wind tunnel is to produce controllable and repeatable flow conditions representative of flows of practical importance, the exact replication of real-world flow conditions in a wind tunnel is virtually impossible. An obvious difference between free-flight conditions and wind tunnel experiments are the presence of test section walls, which lead to interference effects [123, 154]. Most relevant to the results in this thesis is the interference between the test section walls and the wingtip vortex, which changes the effective angle of attack on the wing model relative to free-flight conditions. The effect of the solid test section walls on the wingtip vortex can be modelled using the method of images, as shown in Fig. C.1a [123]. The test section is indicated by the bolded middle square with the semispan wing cantilevered from the side wall. Since the fluid velocity at the test section walls must have zero wall-normal component, each wall of the test section acts as a plane of symmetry. This can be modelled mathematically by the symmetrical placement of potential vortices about each plane of symmetry that mirror the position of the wingtip vortex. Because the test section has four sides, an infinite array of virtual vortices in a symmetrical pattern must be placed outside the test section walls to enforce the symmetry condition at each wall.

The virtual vortices induce a positive Y component of velocity on the wing, which increases the effective angle of attack of the wing relative to an true unbounded flow. The increase in effective angle of attack on the wing produced by the array of virtual vortices ($\Delta\alpha_{eff}$) at a given spanwise location can be expressed in terms of the wing lift coefficient

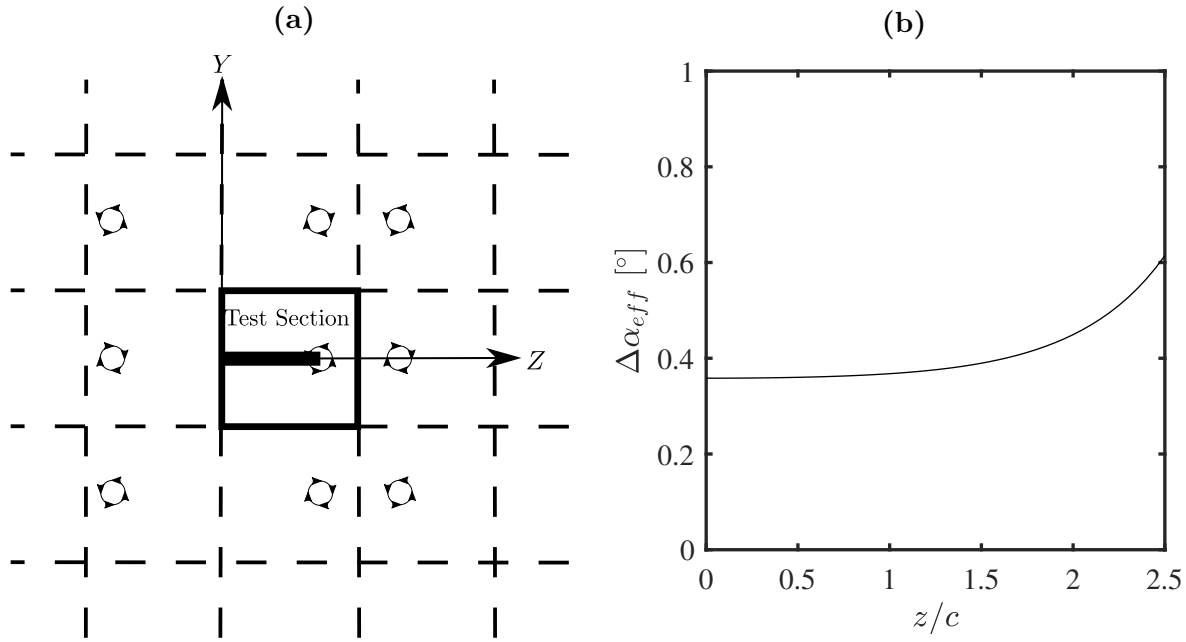

Figure C.1: **(a)** Wind tunnel wall interference on wingtip vortex modelled using method of images, after Theodoresen [123]. **(b)** Increase in effective angle of attack due to wind tunnel wall interference.

(C_L), wing chord, wingspan, and wind tunnel cross-sectional area (A_2): [123]:

$$\Delta\alpha_{eff}(Z) = \frac{C_L cb}{A_2}\zeta(Z) \tag{C.1}$$

where $\zeta(z)$ is determined from the following equation that models the induced velocity at a spanwise position Z on the wing [123]:

$$\zeta(Z) = \frac{b}{8\Delta Z}\sum_{n=0}^{\infty}\left[\frac{1}{\sinh\left(\frac{\pi\left(n\Delta Z-\left(\frac{1}{2}b+Z\right)\right)}{\Delta Y}\right)} + \frac{1}{\sinh\left(\frac{\pi\left(n\Delta Z-\left(\frac{1}{2}b-Z\right)\right)}{\Delta Y}\right)} - \frac{1}{\sinh\left(\frac{\pi\left(n\Delta Z+b-\left(\frac{1}{2}b+Z\right)\right)}{\Delta Y}\right)} - \frac{1}{\sinh\left(\frac{\pi\left(n\Delta Z+b-\left(\frac{1}{2}b-Z\right)\right)}{\Delta Y}\right)}\right] + \frac{\Delta Y}{\pi\left(\frac{1}{2}b-Z\right)} + \frac{\Delta Y}{\pi\left(\frac{1}{2}b+Z\right)} \tag{C.2}$$

where ΔZ is the width of the wind tunnel, and ΔY is the height of the wind tunnel. The increase in angle of attack due to wind tunnel wall interference is plotted in Fig. C.1b versus spanwise location on the wing model. A wing lift coefficient of 0.52 was assumed, based on calculations performed using the wing analysis software XFLR5 [155]. The infinite sum in

Eq. C.2 converges rapidly. The largest increase in effective angle of attack occurs at the wingtip, where $\Delta\alpha_{eff} = 0.61°$, whereas at the wing root, $\Delta\alpha_{eff} = 0.36°$. In Section 4.2, the geometric angle of attack of the lifting line theory fit was calculated to be 0.6° higher than the measured geometric angle of attack of the wing model. Considering the uncertainty in geometric angle of attack of 0.2°, the higher geometric angle of attack of the lifting line theory fit is in reasonable agreement with the change in effective angle of attack due to wall interference.

Appendix D

Supplementary Results

For the purpose of conciseness, not all experimental results obtained during this investigation could be included in the previous chapters. This appendix presents some supplementary results that are referenced briefly in the preceding discussions.

Spanwise Pressure Distributions

The focus of this investigation was on a wing with a semi-aspect ratio of $sAR = 2.5$. This aspect ratio was chosen after conducting pressure measurements on wings with semi-aspect ratios between $sAR = 2.00$ and $s2.75$. Pressure measurements from the spanwise pressure tap arrays at $X/c = 0.15, 0.30$, and 0.60 for the range of semi-aspect ratios tested are shown in Figs. D.1–D.3 for angles of attack of $\alpha = 0.0°$, $5.0°$, and $10.0°$, respectively. Since the goal of this study was to understand the influence of the wingtip on LSB dynamics, isolation of wing root and wingtip effects was desired. Figures D.1–D.3 show that as the angle of attack is increased, the influence of the wingtip extends over a greater proportion of the wingspan. However, at $\alpha = 5°$ (Fig. D.2), close to the angle of attack of $\alpha = 6°$ used for PIV measurements, a substantial region of nearly spanwise uniform pressure occurs for the $sAR = 2.5$ and 2.75 wings centred near $z/c = 0.75$. Although a larger semi-aspect ratio provides a better isolation of tip and root flows, a trade-off between maximising the semi-aspect ratio and minimising wind tunnel wall interference on the tip vortex must be made. Therefore, the semi-aspect ratio of $sAR = 2.5$ was chosen as the focus of this investigation, since it displayed a small region of spanwise uniform pressure at moderate angles of attack, while reducing the effects of wall interference relative to $sAR = 2.75$.

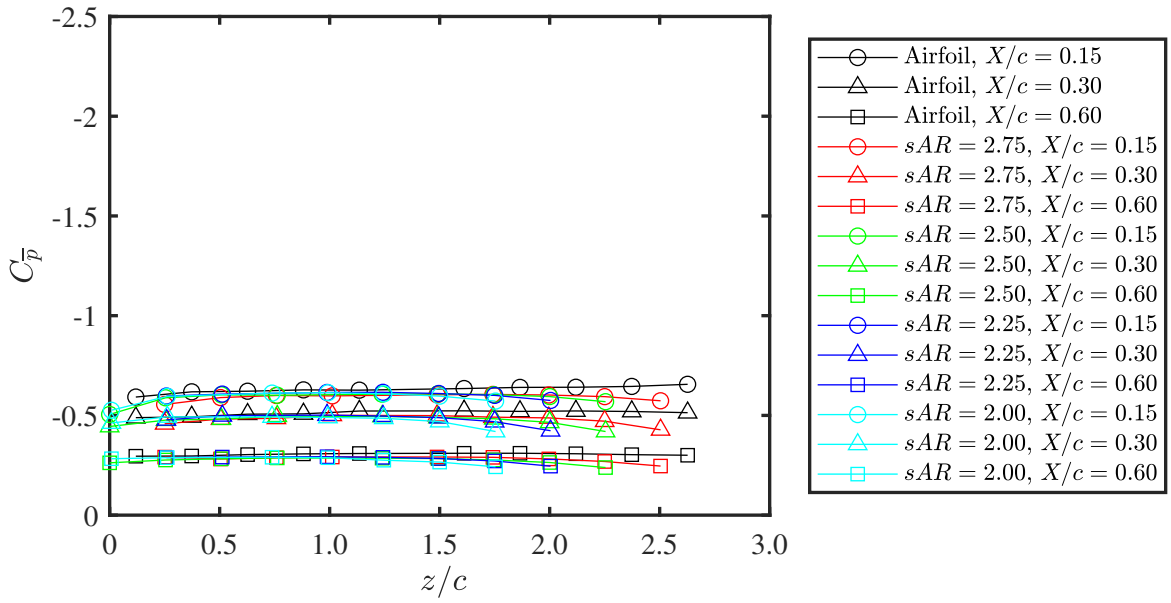

Figure D.1: Measured spanwise pressure distributions at $\alpha = 0°$.

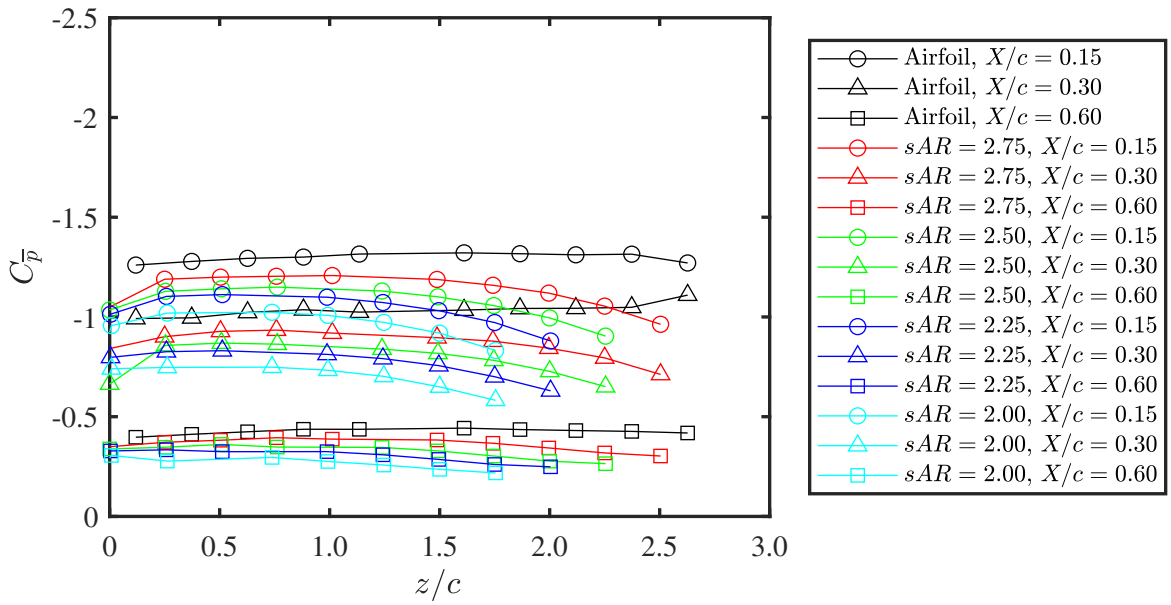

Figure D.2: Measured spanwise pressure distributions at $\alpha = 5°$.

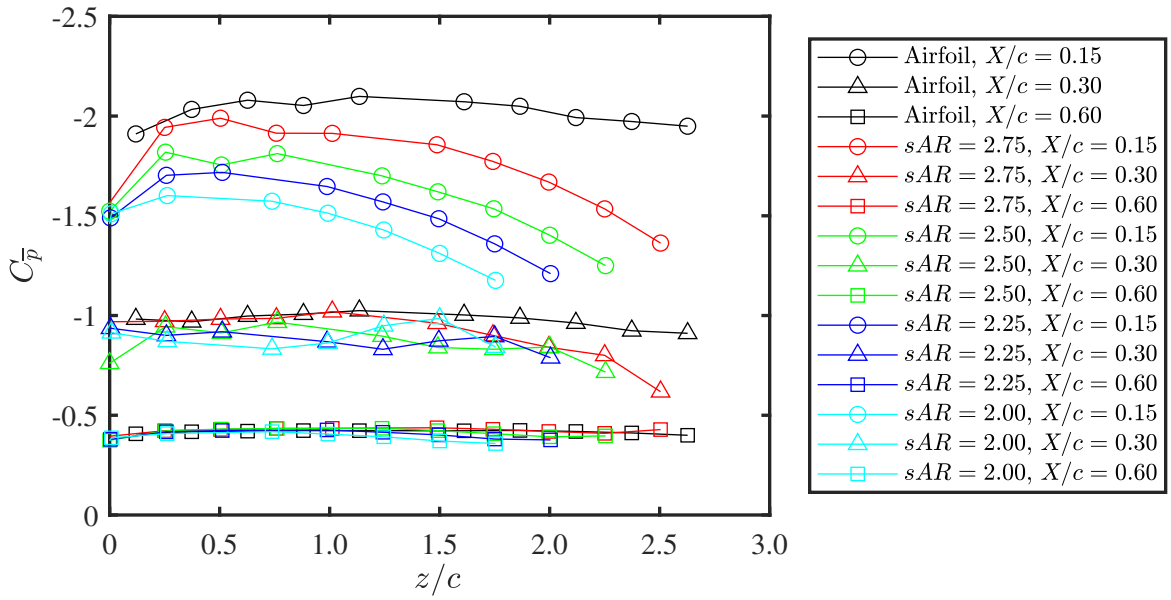

Figure D.3: Measured spanwise pressure distributions at $\alpha = 10°$.

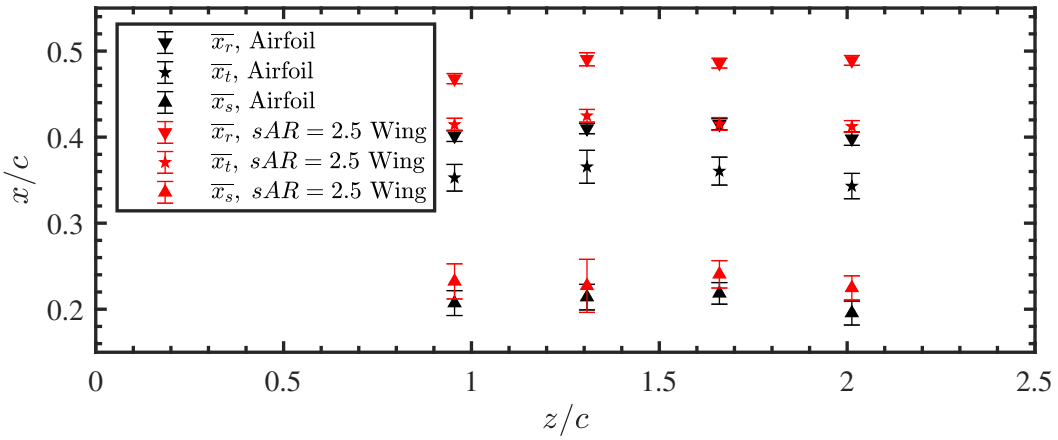

Figure D.4: Spanwise variation in separation, transition, and reattachment on wing and airfoil at $\alpha = 6°$

Spanwise Variation of LSB on Two-Dimensional Airfoil

In Section 4.3 it was claimed that the spanwise variations in the fundamental vortex shedding frequency and the locations of separation, transition, and reattachment seen on the wing were comparable to the variations seen on the airfoil at the same angle of attack of $\alpha = 6°$. Figures D.4 and D.5 show the spanwise variations in these parameters for both the wing and airfoil model configurations at $\alpha = 6°$

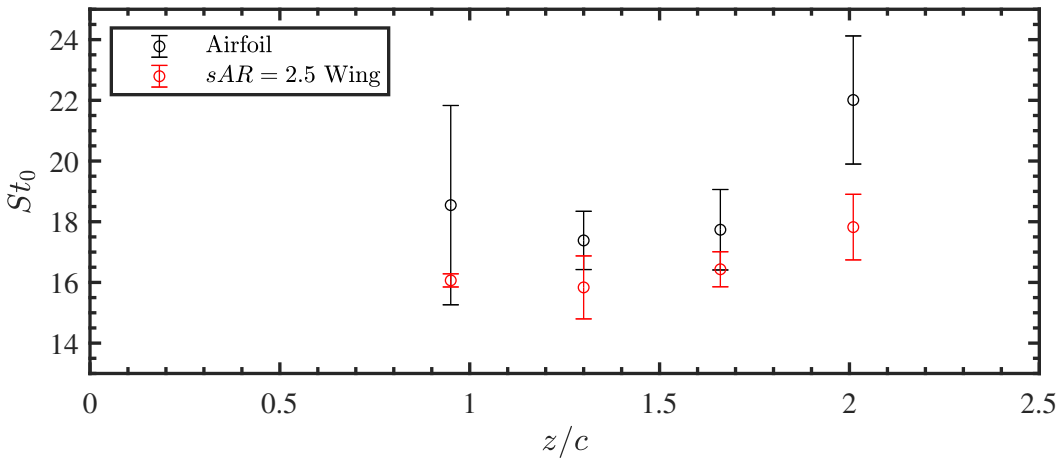

Figure D.5: Spanwise variation in fundamental vortex shedding frequency on wing and airfoil at $\alpha = 6°$